Giovanni Sgubin

XXIV ciclo di Dottorato in
Scienze ed Ingegneria del Mare

University of Naples "Federico II"

A model study of the Southern Ocean dynamics: mean flow, intrinsic variability and teleconnections

PhD Thesis

Tutor:

Prof. Stefano Pierini (University of Naples "Parthenope")

Co-tutors:

Prof. Henk A. Dijkstra (University of Utrecht)
Prof. Enrico Zambianchi (University of Naples "Parthenope")

Wish you were here...

A mio papà Gianfranco,
con immenso affetto.

Contents

Abstract

The general circulation in the Southern Ocean plays a significant role in the global climate, as it connects all the major world basins, carrying anomalies around the globe through the Antarctic Circumpolar Current (ACC). A better understanding of the physical mechanisms that take place in this region can help improve the knowledge of the global ocean circulation.

In this context, this thesis deals with the dynamics of the Southern Ocean and of the ACC by means of a numerical model approach. Results obtained from the primitive equation sigma-coordinate Princeton Ocean Model (POM) concerning both the mean circulation and the intrinsic variability in the Southern Ocean are presented and discussed.

Preliminary simulations are performed in order to set up a consistent circulation for the Sothern Ocean, i.e. with a realistic structure of the ACC fronts and with acceptable values of the volume transport across the Drake Passage. Steady wind stress and heat fluxes are imposed based on climatological data in a periodic channel with realistic coastlines and bathymetry. In order to investigate the role of the bottom form drag on the dynamical balance of the ACC, a hierarchy of model implementations for a homogeneous ocean are first developed using both a flat-bottom and an idealized topography. Baroclinicity is also considered: in particular, the meridional density gradient is found to be a significant element, as it activates the JEBAR effect and prevents a total topographic steering. A consistent model for the ACC is finally proposed using realistic bottom topography and background stratification.

An overview of the simulations in an eddy-permitting resolution shows evidence of intrinsic variability of the ACC. The latter is found to be strongly

sensitive to the bottom topography, eddy viscosity and stratification. By analyzing the results of these numerical experiments we investigate the statistical interrelationships between different regions in the Southern Ocean, and give a first estimate of teleconnections in the Southern Ocean dynamics. Both the variability and the connectivity are found to be very significant in the Argentine Basin, a crucial region where strongly contrasted water masses encounter and mix.

Recent observations in this region have evidenced a clear variability of the flow associated with the Zapiola Anticyclone, a strong counterclockwise current that encircles the Zapiola Rise (the main topographic feature located in the middle of the basin). Our simulations does show such a dynamical feature, along with the existence of two markedly different regimes of the circulation associated with the Zapiola Anticyclone on long-term time scales. In particular, the analysis of transport and sea surface height signals evidence a weakly variable regime related to a quasi-steady circulation around the Zapiola Rise, and a highly variable regime associated with fluctuations of the main flow and with a strong eddy activity. An abrupt transition from one state to the other characterizes such a behavior. Moreover, the counterclockwise topographic circulation around the Zapiola Rise occasionally collapses when, within the highly variable regime, the northern branch of the ACC frontal system (the Sub Antarctic Front) is able to shed this structure away. Interesting agreement is also found when comparing model results with altimeter data.

Chapter 1

Introduction and motivations

1.1 The Southern Ocean

Antarctica is an extreme and isolated continent centred at the South Pole and its environment is unique in many aspects. It is entirely surrounded by the so-called *Southern Ocean*, which separates the continent from the rest of the world. The minimum distance between Antarctica and the mainland is represented by the *Drake Passage*, a relatively narrow inlet between *Cape Horn* and the Antarctic Peninsula.

As a result of the unique geography of the Southern Ocean, the region has a large influence on the global ocean circulation and hence on the Earth's climate: the absence of continental barriers in the latitude band of Drake Passage creates a periodic zonal pathway that allows a circumpolar current to exist. As such, the *Antarctic Circumpolar Current* (ACC), the strongest among oceanic flows, is the only current in the world that connects all the major ocean basins, playing an important role in the transport of heat, salt and other quantities around the globe. The redistribution of water operated by the ACC system is a central process in the global oceanic *conveyer belt*, which connects the ocean surface currents and thermohaline circulation, transporting mass waters on a planetary scale (Figure 1.1). It is therefore possible to

assert that the Southern Ocean is the location of the greatest oceanic teleconnection.

Furthermore, the Southern Ocean represents a significant sink for heat and carbon dioxide, is the world's most biologically productive ocean and one of the sites for the production of the coldest and densest water masses, which are dominant driving forces for the global overturning circulation. This points to the importance of improving our knowledge of the main dynamical mechanisms ruling the Southern Ocean dynamics, especially as far as climate dynamics is concerned: in fact, the ACC flowing around the globe permits anomalies formed in one basin to propagate elsewhere with a consequent influence on the global scale.

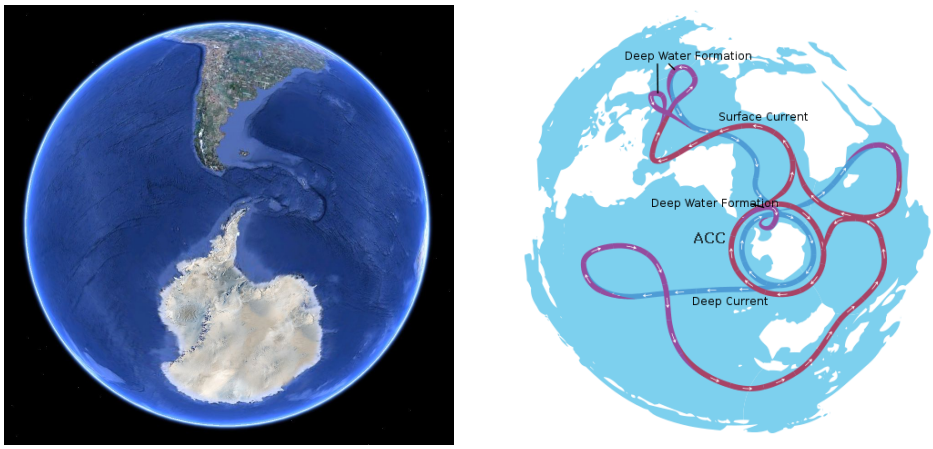

Figure 1.1: *Peculiar geography of the Southern Ocean: the region has no eastwest boundary near the latitude of Drake Passage and directly connects three major oceans. The ACC is the crossroads of the global ocean water masses, connecting the Atlantic, Pacific, and Indian Oceans as well as connecting the deep ocean to the surface, being significant in the global oceanic conveyer belt. The latter consists of a poleward surface flow of warm water in the North Atlantic (the Gulf Stream System), the formation of colder and denser North Atlantic Deep Water (NADW) within the subpolar North Atlantic, a deep southward flow of NADW, upwelling of water in the Pacific Ocean, in the Indian Ocean, and in the Southern Ocean (AABW), and the closure of the circulation by surface return flows into the Atlantic.*

1.1.1 The bathymetry and the wind regime

The bottom topography of the Southern Ocean, as we can see more in detail in the next sections, has a much larger influence on the dynamics

and on the hydrology than in any other oceans. We can anticipate that the ACC is a strong current that is present at all depths, therefore we can expect a mainly topographically driven current system. Furthermore, we can also prefigure that the bathymetry plays an important role in the dynamical balance of the ACC itself, being the central feature in the mechanisms of bottom form drag. It is possible to divide the whole periodic basin into three sectors: the Atlantic sector between South America and South Africa, the Indian sector between South Africa and Australia and the Pacific sector between New Zealand and the western side of South America.

The Atlantic sector is certainly the most variable in terms of topography. As already mentioned, the Drake Passage is a very narrow constriction that separates the Antarctic Peninsula from South America. This tight passage is surrounded by a series of submarine mounts and islands that make the passage even more narrow (780 km at 500 m depth level). Here, the current accelerates in this narrow gap. The strong flow of the ACC across this natural transit is partially blocked by another seamount, i.e. the *Scotia Ridge*, located 2000 km east of the Drake Passage; this topographic anomaly obstructs the increased current, which, as a consequence, becomes highly turbulent and shifts sharply northward. Part of this water follows the continental shelf of South America, forming the Malvinas Current, a western boundary current that collides with the Brazil Current from the north forming one of the most energetic areas in the world, i.e. the *Confluence Zone*. This region is close to the *Argentine Basin*, which is characterized by a depth of more than 6000m and is bounded by a very steep continental slope. In the middle of the basin a sedimentary deposit is located, the so-called *Zapiola Rise* (ZR), whose top is about 1000 m higher than the abyssal plain. This particular topography creates a very intense counterclockwise barotropic flow, i.e. the *Zapiola Anticyclone* (Saunders and King, 1995) which is likely to be an important mechanism in the exchanges of heat between the Southern Ocean and lower latitudes (de Miranda *et al.*, 1999).

The *Atlantic-Indian Basin* forms part of the the Atlantic and Indian Ocean sectors and is connected with the *Weddell Sea* to the west and the *Kerguelen Plateau* to the east, the latter constituting an obstruction for the path of the ACC. The existing data suggest the possible generation of eddies in this region, which is an important mechanism for the meridional exchange of heat.

In general, such a process takes place where major topographic features are located.

In the Pacific sector it is worth mentioning the *Pacific-Antarctic Basin*, that extends eastward from the *Ross Sea*, and two submarine mountain chains, i.e. the *Pacific-Antarctic Ridge* and the *East-Pacific Rise*, which influence the path of the ACC. Figure 1.2 summarizes the most prominent topographic features in the Southern Ocean.

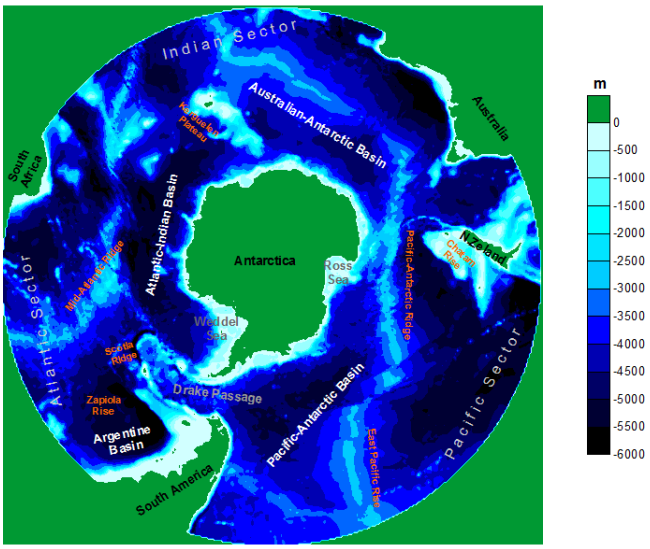

Figure 1.2: *Bottom topography of the Southern Ocean.*

The main forcing for the ACC system is the wind stress. It is predominantly zonal, westerly between $65°S$ and $30°S$ and dominated by frequent storms, and easterly elsewhere (Figure 1.3). The meridional Ekman transport is therefore northward between $65°S$ and $30°S$ and southward south of $65°S$ and north of $30°S$. As a consequence, it is possible to locate a zone of convergence, the *Antarctic Convergence* near the line of vanishing wind stress curl in the westerly winds band (at around $55 - 60°S$), and a zone of divergence, the *Antarctic Divergence* at around $55 - 60°S$. The region of the Antarctic Convergence, as it will be shown below, is where the ACC flows. Rather than a single geostrophic zonal current, the ACC is actually a system of nearly zonal geostrophic fronts that flow eastward. The most

important among them are, from north to south, the *Subtropical Front* (STF), the *Subantarctic Front* (SAF) and the *Polar Front* (PF) (Figure 1.4). Close to the Antarctic continent the winds show a reversal from westerlies to easterlies, the Polar Easterlies, which drive the *East Wind Drift*, a narrow coastal current which flows westward against the dominant eastward-flowing ACC. In the presence of partial land constrains close to Antarctica, i.e. in the Weddell Sea and in the Ross Sea, the combination of East Wind Drift, ACC and coastlines produces two gyres, the *Weddell Sea Gyre* and the *Ross Sea Gyre*.

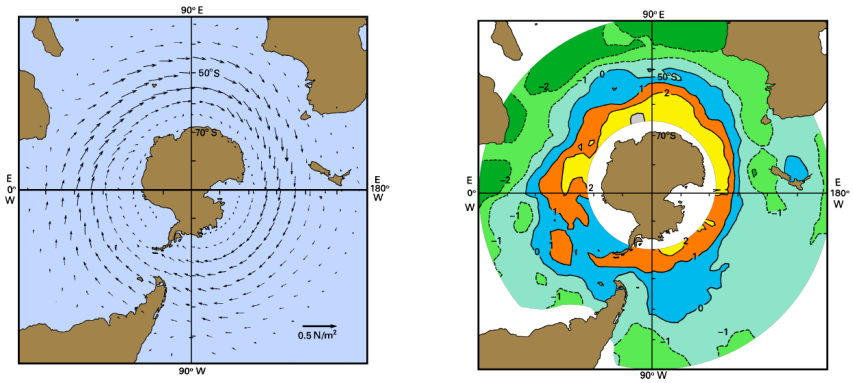

Figure 1.3: *The wind stress pattern (left panel) and the wind stress curl (right panel) in the Southern Ocean. From Tomczak and Godfrey (2003).*

1.1.2 Hydrology

Another important feature related to the Southern Ocean is a general weak stratification of the water. The higher the latitude the shallower the permanent thermocline, which even vanishes in polar regions. This reaches the surface approximately at the *Subtropical Convergence* area, which corresponds to the region of negative curl (τ/f) (Figure 1.5). Therefore, the temperature difference between the sea surface and the deep ocean in the polar region does not exceed 5 °C, that is just 20% of the difference found in the tropics. The weak stratification enhances the interaction between the flow and the bottom topography, making the barotropic mode very important in the Southern Ocean. Moreover, the Southern Ocean is the formation region of several water masses that are spread around the world ocean. During the polar winters, such a vertical distribution of temperature promotes an

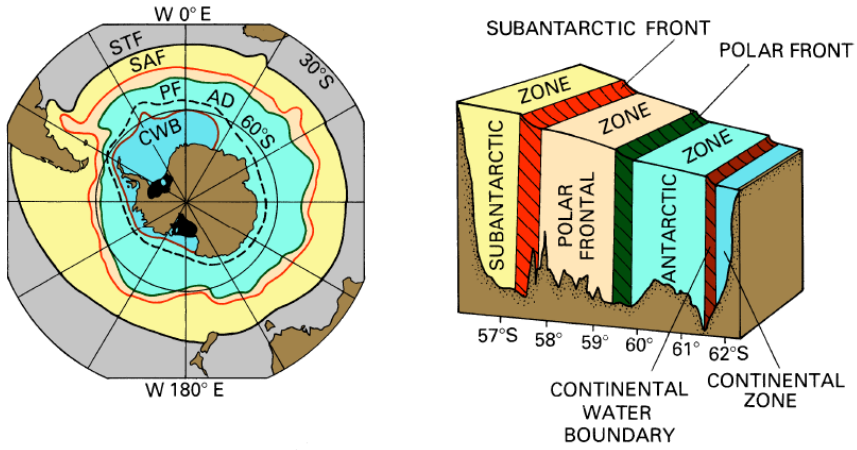

Figure 1.4: *The pattern of the main fronts of the AAC (left panel) and the associated zones of convergence and divergence (right panel). From Tomczak and Godfrey (2003).*

overturning, with colder water overlying warmer water, while the salinity distribution typically promotes stratification, with fresher water overlying saltier water. This instability yields the formation of denser and colder water in particular areas of the Southern Ocean that ventilate the abyssal and intermediate depths of the world ocean.

The intense mixing processes, together with the combined action of the westerly winds and the bottom topography create areas of convergence and divergence: the ACC is hence a system of fronts which marks off different types of water masses (see Table 1.1).

Table 1.1: *Definition of the main water masses in the Southern Ocean obtained from WOCE Repeat Section SR03. The samplings were conducted six times and every 30 nautical miles across a section between Antarctica and Tasmania for the period 1991/1996. Data from Tomczak and Liefrink (2005).*

Water Mass	Potential Temperature ($^\circ C$)	Salinity	Oxygen ($\mu mol/kg$)
SAMW	8.75	34.58	250
AAIW	4.40	33.75	310
UCDW	2.15	34.40	165
LCDW	2.06	34.77	195
AABW	-1.4	34.60	275

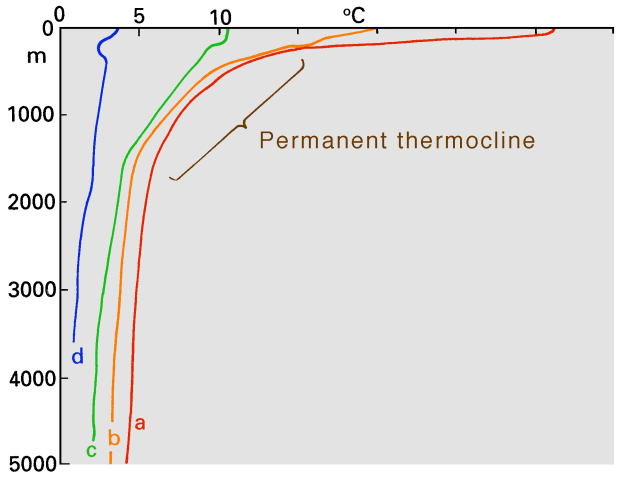

Figure 1.5: *Temperature profiles for different climatic regions near 150 °W (Pacific Ocean): (a) tropical (5 °S), (b) subtropical (35 °S), (c) subpolar (50 °S), (d) subpolar (60 °S). The temperature scale is correct for the polar profiles whereas the other profiles are shifted successively by 1 °C. Note the thinning of the warm surface layer with the latitude and the substantial absence of a permanent thermocline in the polar region. Picture from Tomczak and Godfrey (2003).*

The Subtropical Convergence is a subduction region and it is of some 1000 km extent. Within this area, there exists a narrow band all around the Antarctic continent where surface salinity and temperature changes rapidly, i.e. the *Subtropical Front* (STF) that runs roughly parallel to the contour of zero wind stress curl just some degrees north of it. The STF can be also defined as the northern limit of the Southern Ocean. South of it, the ACC consists essentially of a number of circumpolar fronts, which correspond to different water mass limits (Orsi *et al.*, 1995). The two main fronts of the ACC, as already mentioned, are the *Subantarctic Front* (SAF) and the *Polar Front* (PF). We can roughly assume that the SAF separates the *Subantarctic Mode Water* (SAMW) from the *Antarctic Intermediate Water* (AAIW), and the PF separates the AAIW from the *Circumpolar Deep Water* (CDW).

The SAMW is formed by deep convection in late winter on the northern flank of the ACC near the SAF. The surface density of SAMW ranges between about 1026.0 and 1027.0 $\mathrm{kg\,m^{-3}}$ and the core of this water mass is often identified as a region of particularly low stratification. The SAMW is important for the carbon sinking, and for absorbing atmospheric carbon

dioxide, and in general acts as an oxygenator for mid oceanic depths in the Southern Ocean (McCartney, 1977). The Antarctic Intermediate Water (AAIW) is identified by a prominent salinity minimum. Various processes contribute to its formation along the PF (Sorensen *et al.*, 2001).

The *North Atlantic Deep Water* (NADW), the water mass that is formed in the North Atlantic Ocean by the sinking of highly saline, dense overflow water from the Greenland Sea, is able to reach the latitudes of the Antarctic Divergence, where it upwells. At the surface, part of this water moves northward where persistent precipitations decrease the salinity of the original NADW. It is customary to identify this new water mass as the Antarctic Surface Water (AASW). Moving northward in the Antarctic Convergence, the AASW encounters the warmer SAMW and it begins to sink because it is denser than the Subantarctic water to its north, but less dense than the Antarctic water to its south. The sinking AAIW becomes sandwiched between the SAMW (in the upper part), which is much warmer (but more saline), and the Upper Circumpolar Deep Water UCDW (in the lower part), which is colder and quite salty. The rest of the upwelled NADW turns toward Antarctica, where it gets colder and sinks back down forming the *Antarctic Bottom Water* (AABW). Most of the AABW is formed in the polynyas of the Weddell and Ross Seas, where the high production of ice, in combination with the action of katabatic winds (which sweep the ice away), enriches the concentration of salt in the surface water. Observed data show an overflow of dense water originated on the continental shelf, in very localized areas, e.g. in the Ross Sea shelf break (Bergamasco *et al.*, 2002). As a consequence, the denser water masses flow down the Antarctic continental margin, and the bottom further north.

The Circumpolar Deep Water (CDW) is a major water mass in the Southern Ocean, as it is involved in the formation of all others (Whitworth III *et al.*, 1998). It is the product of North Atlantic Deep Water (NADW) being modified through mixing with deep waters from the Indian and Pacific Oceans while being carried eastward by the ACC. The contributions from different sources can be traced to some extent, and several investigators distinguish Upper Circumpolar Deep Water (UCDW, which is characterized by an oxygen minimum and nutrient maxima), and Lower Circumpolar Deep Water LCDW, which is characterized by its high NADW salinity (Whitworth III

et al., 1998). Figure 1.6 shows a schematic view of the general hydrology and of the overturning circulation in the Southern Ocean.

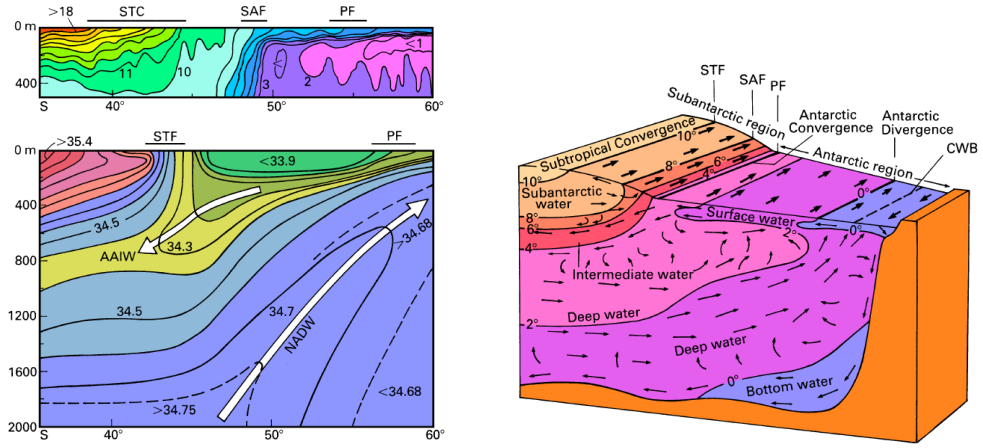

Figure 1.6: *A general sketch of the hydrology and of the meridional overturning in the Southern Ocean. (left panel) Temperature section (above) and salinity section (below) in the eastern Indian sector and identification of the major fronts; (right panel) schematic view of the deep circulation in the Southern Ocean. From Tomczak and Godfrey (2003).*

1.1.3 The Southern Ocean and the global climate

The first evidence of the influence of the Southern Ocean on the global climate is the significant air−sea exchanges of heat that take place locally. The amount of heat lost by the sea mitigates the cold air temperature at high latitudes and regulates meridional heat exchanges with lower latitudes.

The Southern Ocean also affects significantly the general climate by absorbing and storing a great amount of carbon dioxide, an important and beneficial process as it slows the rate of global warming.

However, the most important impact of the Southern Ocean on planetary scale is probably due to the role played by the ACC in the general ocean circulation. The large-scale ocean circulation could, generally speaking, be divided into two parts:

1. the *wind-driven circulation*, caused by the momentum flux from the wind to the ocean surface: it is largely responsible for the upper ocean

currents. This is, however, not fully valid for the Southern Ocean, where the wind stress influences also the deep ocean;

2. the *density-driven circulation* or *thermohaline circulation* (THC), caused by fluxes of heat and freshwater between ocean surface and atmosphere, which propagate to the deeper ocean by advection and mixing. The thermohaline circulation thus generally involves the whole depth, and is responsible for many of the features of the general climate.

On global scale, wind-driven circulation and THC contribute together to the global conveyor belt, which gathers all the main oceanic regimes in a single connected mechanism (Broecker, 1991). Surface warm water flows polarward in the North Atlantic mainly carried by the Gulf Stream. In the Labrador Sea and in the Greenland Sea, the surface water, now colder and denser (NADW), sinks and turns southward at depth. This reaches the Southern Ocean where the nearly zonal ACC spreads the deep water originated in the North Atlatic all around the globe. The water gradually upwells in the Indian Ocean and in the Pacific Ocean as well as in the Southern Ocean (AABW). The loop is eventually closed by the superficial return of the upwelled water from each basin into the Atlantic. Such an interbasin exchange can take place only in the unbounded Southern Ocean and allows a global scale overturning circulation to exist.

The oceanic heat transport accomplished by the global THC and its stability have been subject of intensive studies. It was shown how the global THC is likely to have more than one stable modes of operation (Stommel (1961), Bryan (1986), Hughes and Weaver (1994), Dijkstra (2007)). This hypothesis has been applied to studies of paleoclimate variability (Rahmstorf, 2002) and it is a central question within the present discussion on climatic change, in which the possibility of a future shutdown of the global THC induced by anthropogenic greenhouse gas emissions and/or by natural cycle has been estimated (Stocker and A. (1997), Rahmstorf (2000), Dijkstra and te Raa (2004)). The possible effects of the processes occurring within the Southern Ocean on the stability of the global THC are the AABW-NADW seesaw, i.e. the anticorrelation of the formation rates of AABW and NADW (Weijer *et al.*, 1999), and the interbasin exchanges (Weijer *et al.*, 1999), strictly related to the ACC system.

1.2 The observed Antarctic Circumpolar Current

In a recent past our knowledge of the structure of the ACC was very poor due to the scarce and sparse nature of measured data in the Southern Ocean. In the last decade, however, the *World Ocean Circulation Experiment* (WOCE), in combination with advances in remote sensing, have revealed a number of new features of the ACC as well as of the general Southern Ocean circulation (see Rintoul *et al.*, 2001, for a review).

The strong westerly winds over the Southern Ocean drive the world's largest current system, the ACC, with an associated zonal transport across the Drake Passage of 130 ± 15 Sv (Whitworth III, 1983). The ACC consists of a system of circumpolar fronts that encircle the Antarctic continent, with a zonal extension of about 24000 km. Current speeds at the surface are, on average, small ($O(0.1)$ m/s) if compared with those of other flow regimes, e.g. the Gulf Stream, with its $O(1)$ m/s on the surface, although 0.5 m/s and 1 m/s have been occasionally observed in jets associated with frontal regions. It may seem strange that the world's strongest current is associated with weak surface currents. On the other hand, since in the Southern Ocean density variations with depth are small, the pressure gradient force is more evenly distributed over the water column. As a result, currents are not just restricted to the upper layer but extend to very high depths, sometimes reaching the bottom. This explains why the ACC has the largest mass transport among all ocean currents.

Despite the zonal flow of the ACC is the dominant circulation feature, the weaker meridional mass transport is also significant. The NADW flows from north in the Southern Ocean with an estimated 15 Sv transport. The AABW flows in the opposite direction with a meridional transport of about 5 Sv. The northward Ekman transport in the westerly wind belt closes the mass balance. However, the heat balance is likely not to be satisfied by such a meridional circulation. In fact, the heat loss from the ACC region to the atmosphere has been estimated as 3×10^{14} W (Gordon and Owens, 1987). This must be balanced, in some way, by a poleward heat flux across the Antarctic zonal fronts. The closure of the heat balance is likely to be provided by the meridional migration of large eddies generated by the interaction of the strong zonal currents with the topography. The role of eddies is therefore of

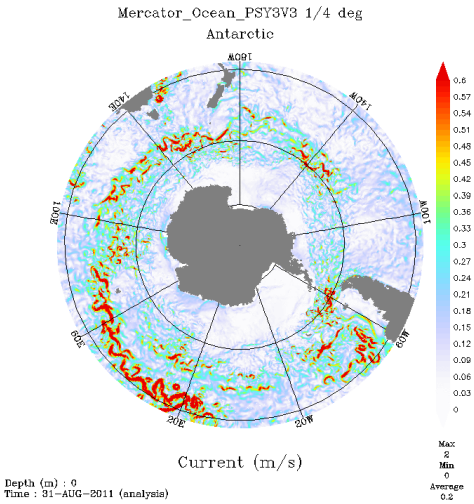

(a) *Superficial current during the South Hemisphere winter.*

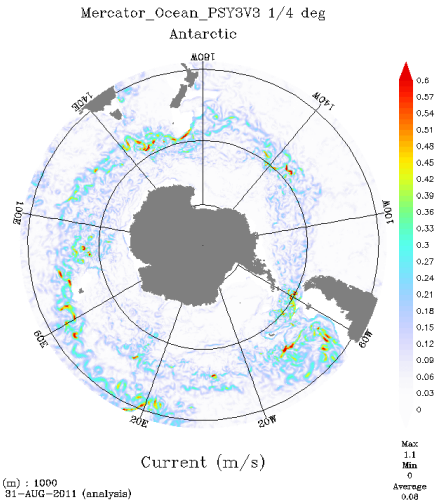

(b) *Current at 1000 m during the South Hemisphere winter.*

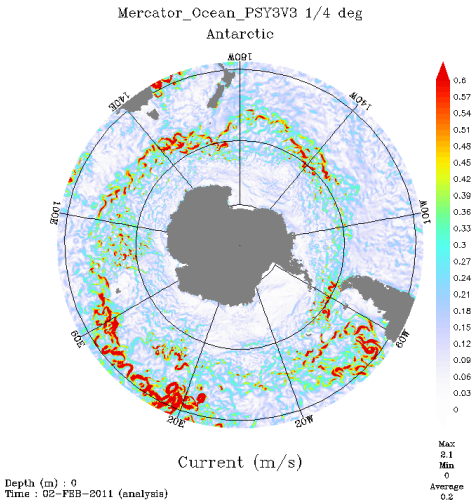

(c) *Superficial current during the South Hemisphere summer.*

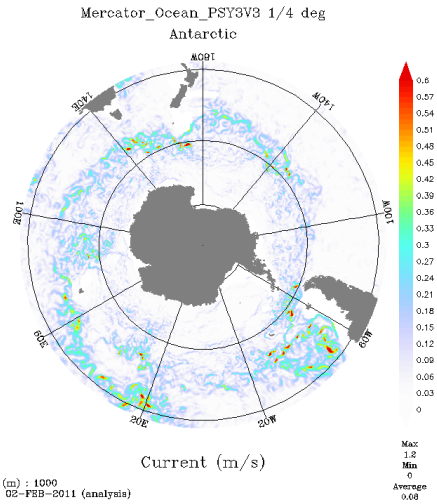

(d) *Current at 1000 m during the South Hemisphere summer.*

Figure 1.7: *Snapshot of the current mean field at the surface and at 1000 m depth for two different period of the year: (top) 31/8/2011; (bottom) 09/02/2011. Data from* Mercator Ocean

outstanding importance for the Southern Ocean circulation.

1.2.1 Eddies and rings: exchange of heat and momentum

In the Southern Ocean, the zonal periodicity in the Drake Passage latitude band does not allow a net meridional geostrophic flow to exist, i.e. a net meridional exchange of heat accomplished by a mean gyre current system. As a consequence, the ACC acts as a brake for meridional flows, partially isolating the polar water from the warmer waters at lower latitudes. However, a dynamical and thermodynamical balance is likely to be provided for by an intense eddy activity. Several observations (e.g Trani *et al.*, 2011) show a large amount of mesoscale variability associated with the zonal fronts of the ACC, mostly concentrated in specific regions along its path, where the flow crosses the main topographic anomalies, i.e. where the conditions for baroclinic instability are satisfied. One such region is the Drake Passage, where numerous cold and warm core rings have both been reported (Peterson *et al.* (1982); Pillsbury and Bottero (1984)). The Figure 1.8 shows a time series of temperature at Drake Passage between June 1975 and January 1976, when five cyclonic (cold core) rings and one anticyclonic (warm core) ring passed over the site of the measurement. These eddies have a diameter of $30 - 130$ km, and they extend to at least 2500 m depth. Analysis of the water properties within the rings suggests that they originate at the PF and at SAF (Pillsbury and Bottero, 1984). After they moved directly across the Drake Passage, parallel to submarine ridges, these rings appears to turn equatorward. Their northward motion, which is at about $4\,\mathrm{cm\,s^2}$, carries cold water to lower latitudes across the zonal fronts, representing, indeed, a poleward flux of heat. Estimates from satellite data Keffer and Holloway (1988) give values of $1.3 - 5.4 \times 10^{14}$ W, a consistent value for balancing the estimated heat loss to the atmosphere.

Other sites of rings generation and migration are the South-West Indian Ridge (Swart *et al.*, 2008), southeast New Zealand (Stanton and Morris, 2004) and, in general, where the flow associated with the fronts crosses shallow bathymetry.

The process of ring migration across the ACC fronts is therefore potentially responsible for a significant meridional heat flux. Moreover, the high eddy activity is also important in the momentum budget of the Southern

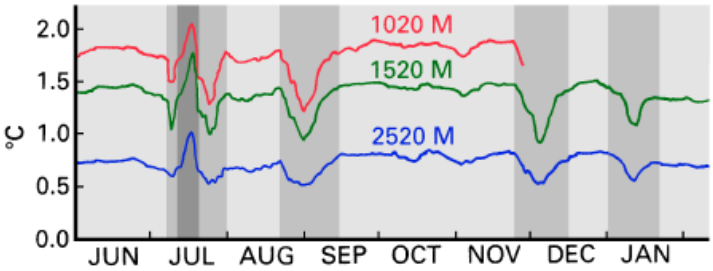

Figure 1.8: *Temperature records obtained at a mooring in the Drake Passage, indicating the transition of of five cold core rings and one warm core ring. From Pillsbury and Bottero (1984).*

Ocean. Eddies not only carry heat northward, but they provide a transfer of momentum as well, dissipating the kinetic energy of the circumpolar fronts and, as a consequence, decelerating some of the strongest jets (Hughes and E. Ash, 2001). As described later, the central mechanism in the balance between wind forcing input and frictional stresses is the vertical transfer of momentum downward across density surfaces (rather than horizontally) accomplished by the eddies, which prevents indefinite acceleration of the zonal flow in the unclosed band (Olbers *et al.*, 2004).

1.3 Variability in the Southern Ocean and its link to climate changes

The processes occurring in the Southern Ocean and those closely connected with the ACC dynamics certainly have impacts on the stability of the global THC. The way in which interbasin exchanges take place, the strength of the ACC transport, the evaporation/precipitation budget, the ice formation and melting, the absorption of carbon dioxide, and the air-sea heat exchanges are just some of the processes that could potentially influence not only the climate within the Southern Ocean, but even the global climate system. Paleoclimate records demonstrate that changes in the global THC have been probably associated with an abrupt climate alteration in the past, involving polar processes which could modify the global water cycle.

The Southern Ocean is a region where very rapid changes have been observed in the recent past. The observed sea surface temperature, for ex-

ample, shows a general warming trend during the last 50 years (Figure 1.9). Associated with this warming, the salinity of the surface water has decreased and precipitation in this region has increased. Recent analysis (Naveira Garbato *et al.*, 2009) have also revealed a substantial variability on interannual to interdecadal time scales associated with the SAMW and AAIW. Sparse ocean observations suggest that large changes are already occurring in the current climate system, in a manner that could be broadly consistent with a more vigorous hydrological cycle. It is still under debate if such a global climate change is dominated by a natural internal variability or if it is significantly related to an anthropogenic impact.

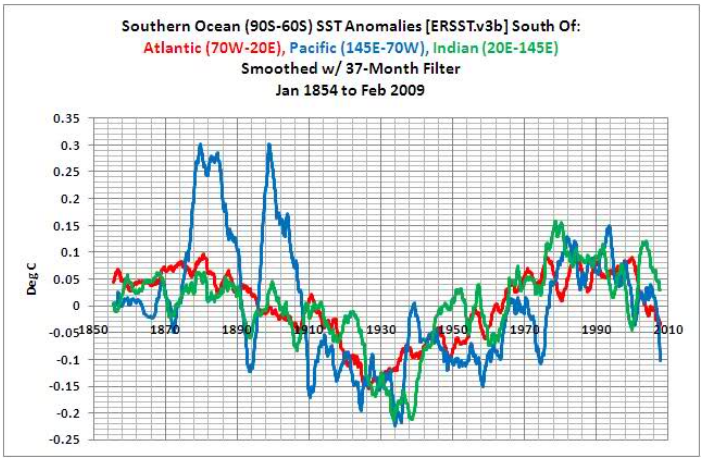

Figure 1.9: *Sea Surface Temperature (SST) anomalies in the Southern Ocean from 1854 to 2009 analyzed by Extended Reconstructed Sea Surface Temperature (ERSST). The analysis is based on the International Comprehensive Ocean-Atmosphere Data Set (ICOADS). At the end of every month, the ERSST analysis is updated with the available GTS ship and buoy data for that month. The anomalies are computed with respect to a 1971-2000 month climatology.*

1.3.1 Variability associated with the ACC

The analysis of observed data evidences a variability associated with the ACC in a relatively small range of time scales. This variability is mainly locally forced by oscillations of the atmospheric forcing, such as the *Southern Annular Mode* (SAM), a dominant mode of variability in the Southern Hemisphere (Sallee *et al.*, 2008). On a monthly time scale there is a con-

nection between the circumpolar transport and the 30-60 days *Madden-Julian Oscillation* (the largest interseasonal atmospheric variability at the tropical latitudes) in the tropical Indian Ocean (Matthews and Meredith, 2004). Furthermore, there is evidence for a wind-driven variability at subannual time scales.

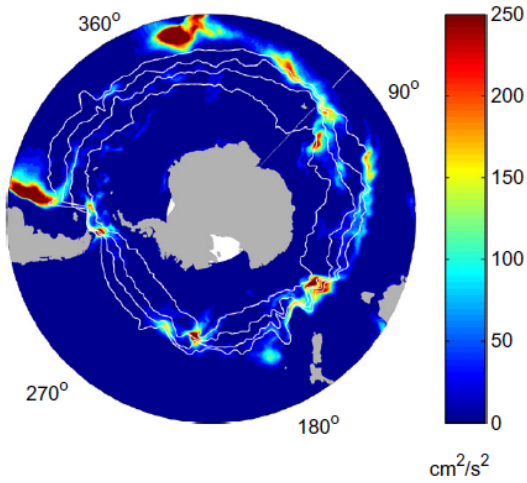

Figure 1.10: *Mean eddy kinetic energy field for the Sothern Ocean from DRAKKAR ocean model output. White lines represent the major fronts of the ACC. Figure from Langlais et al. (2011).*

Figure 1.10 shows the mean eddy kinetic energy from DRAKKAR ocean model (Langlais *et al.*, 2011) and gives a real indication of the mesoscale eddy activity, e.g. mesoscale variability, in the Southern Ocean: the most prominent energetic areas are in proximity of the Brazil/Malvinas confluence and the Aghulas current retroflexion, as well as along the pathway of the ACC, where the intense mesoscale variability is associated with the detachment of eddies from the mean flow.

On longer time scales, measured data (White and Peterson, 1996) have evidenced the existence of the *Antarctic Circumpolar Wave* (ACW), a dynamical phenomenon which may depend on oceanic teleconnections provided by the ACC. The observed ACW consisted of anomalies in the sea-surface temperature, sea-level pressure and sea-ice extent that propagated eastward around the Southern Ocean. Such a wave had a wavenumber 2 and its

cycle around the globe was complete in about 8-9 years, so the apparent period at any location was about 4 years. Despite the ACW events have been identified for a limited time, its dynamics is still a topic of active debate and several numerical models have been used to investigate its nature, proposing a variety of physical hypotheses. The ACW could arise as a result of atmospheric teleconections related with the *El Nino-Southern Oscillation* (ENSO) (Peterson and White, 1998). Other studies suggest a coupled mode of the ocean-atmosphere system within the Southern Ocean for the generation and the maintenance of the ACW (Baines and Cai, 2000). On the other hand, Weisse *et al.* (1999) demonstrate that a ACW-like variability within the Southern Ocean could be reproduced with an uncoupled stochastic atmospheric forcing, strengthening the hypothesis of an ACW due to a intrinsic ocean response to the atmospheric forcing.

Variability at longer time scales cannot be diagnosed with confidence because of the lack of a sufficiently long-period satellite record and the sparse nature of ocean datasets in the Southern Ocean. However, some hints of interannual variability of the ACC transport across the Drake Passage have been evidenced despite the paucity of existing data (Figure 1.11). Moreover,

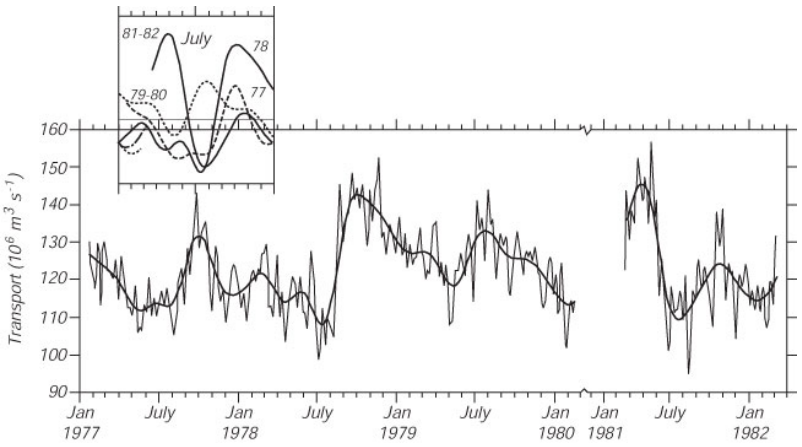

Figure 1.11: *Variability of the transport of the Antarctic Circumpolar Current across the Drake Passage obtained from bottom pressure measurements from January 1977 and March 1982. The thick line is the smoothed, time-averaged transport. From Whitworth III (1983).*

Hogg and Blundell (2006) have indicated the potential for a low-frequency intrinsic variability associated with the ACC using a quasigeostrophic model.

Thus, beyond the variability driven by fluctuations of the atmospheric forcing, mechanisms of variability generated within the ocean system could also be present. Such intrinsic changes can advantageously be investigated by means of *dynamical system theory*.

1.4 The main topics of the thesis

The importance of the oceanic processes that take place in the Southern Ocean, and their involvement in the global climate system, have been stressed in this introductory chapter. In this context, the aim of this thesis is to investigate further the dynamics of the ACC both for the time-mean circulation, and for its variability. The study is essentially based on a process-oriented numerical model approach. Simulations with a *primitive equation ocean model*, the *Princeton Ocean Model* (POM) have been carried out. The results have been used to provide possible theoretical explanations of specific processes occurring within the Southern Ocean.

The first purpose is the definition of a model for the Southern Ocean dynamics that is able to reproduce a realistic ACC mean circulation. Through a series of different model configurations, the role of the bottom topography and background stratification has been found to be significant in reproducing a realistic path of the circumpolar flow and correct values for the zonal transport (Chapter 2).

Changes in the circulation of the Southern Ocean are expected to have large and widespread effects on the circulation at the global scale. Hence, a simple question arises:

- How and why are the Southern Ocean circulation and water properties changing?

In this context, in Chapter 3 the possible existence of *intrinsic variability* of a nonlinear ACC will be investigated. By using a steady forcing, thus excluding externally induced changes, we will identify potential internal mechanisms that could lead to both high and low-frequency variability.

Although it is not possible to make use of a long time series of instrumental records in the Southern Ocean, the short time series available are,

nonetheless, starting providing evidence for a low-frequency variability associated with the ACC. Observations are certainly still not sufficient and an exhaustive physical interpretation of such a variability in terms of dynamical system concepts would require more information. Our model approach is therefore the only one that currently is possible to use. Along this way, the results of our simulations, beyond the pure investigation of Southern Ocean dynamical system, may be useful for analyzing and interpreting future observational data and other numerical experiments.

After having detected signals of intrinsic variability associated with the Southern Ocean system, another question spontaneously arises:

- What is the impact of ACC circulation changes on the circulation of other sectors of the ocean system?

In Chapter 4 *Teleconnection processes* within the Southern Ocean are identified: they can play a decisive role in affecting the global climate, in particular the THC. At this point of the work, it is possible to use data generated by the numerical simulations for a statistical analysis. In particular, in the same chapter, in order to create a *Southern Ocean Network System* and to define a *teleconnection map*, possible dynamical similarities between different regions within the Southern Ocean will be investigated.

In Chapter 5, we will focus on the circulation in the Argentine Basin, a region where a very high variability is evidenced by our results. The main question behind the discussion in this chapter is:

- How do the surrounding oceans affect the dynamics of the ACC?

It will be shown how such a variability, supported also by observational data, is likely to be strictly connected with the transport of the ACC, representing not just a regional process, but influencing the circulation at larger scale.

Chapter 2

A model of the ACC mean flow

2.1 Introduction

The peculiar dynamics of the circulation of the Southern Ocean is still a widely discussed topic among researchers, and many efforts are currently being made for a better understanding of the factors determining the nature of the ACC. In this context, the *momentum balance* of the ACC is a central issue, and its exhaustive physical interpretation is a necessary step to get a deeper knowledge of the effective role played by the ACC in the Southern Ocean dynamics, as well as in the global climate system.

Many attempts have been made in order to reproduce the ACC circulation with numerical models, and the results are quite contrasting. The values of the zonal transport across the Drake Passage, for example, are spread over a large range from well under 100 Sv to well over 200 Sv, as it is shown in Table 2.1. The reason for this discrepancy is due to different factors, such as the model resolution and the representation of the topography (Best *et al.*, 1999), the parameterization of the subgrid scale turbulence (Danabasoglu

and Mc Williams, 1995), the wind forcing and the background stratification (Gent *et al.*, 2001).

Table 2.1: *Volume transport of the ACC diagnosed from some numerical models.*

Model	Category	Transport	Reference
CB96 1IW	coarse resolution	75 Sv	Cai and Baines (1996)
CB96 2IW	coarse resolution	120 Sv	Cai and Baines (1996)
GH00BA	coarse resolution	207 Sv	Gnanadesikan and Hallberg (2000)
NCAR GLOB01 A	coarse resolution	120 Sv	Gent *et al.* (2001)
NCAR GLOB01 B	coarse resolution	117 Sv	Gent *et al.* (2001)
NCAR GLOB01 C	coarse resolution	250 Sv	Gent *et al.* (2001)
NCAR GLOB01 D	coarse resolution	231 Sv	Gent *et al.* (2001)
FRAM	eddy-permitting	195 Sv	FRAM group 1991
POP 11	eddy-resolving	136 Sv	Gent *et al.* (2001)
obeserved	measurements	130 Sv	Whitworth III and Paterson (1985)

In this chapter, our first aim is to determine a realistic steady regime for the ACC using the *Princeton Ocean Model* (POM), the *σ-coordinate primitive equation model* created by Alan Blumberg and George Mellor in 1977. We will start from a simple model implementation (i.e. with a flat-bottom topography with realistic continents for an unstratified ocean) and, through a hierarchy of configurations, we will introduce step by step other factors that can influence the circulation, in so evidencing those that are necessary to determine a reasonable Antarctic Current system. For "reasonable" we mean that our modeled ACC has to be in agreement with observations as far as (i)the position of the main fronts, and (ii) the transport through the Drake Passage are concerned. The transports through the main choke points are, indeed, used in the standard diagnostics for numerical models of the Southern Ocean circulation.

2.2 Why is the ACC dynamically so interesting?

The ACC, with its 130 Sv volume transport across the Drake Passage and its zonal extent of 24.000 km, is the most energetic among the ocean currents.

As already mentioned, the absence of land barriers near the latitude of Drake Passage has a significant impact on the climate of the Southern Ocean as well as on the global climate. The peculiar geometry of the region makes the dynamics of the ACC markedly different from those of other ocean currents. The ACC differs from other oceanic regimes primarily because the flow is predominantly and continuously zonal, as it is sketched in Figure 2.1. On

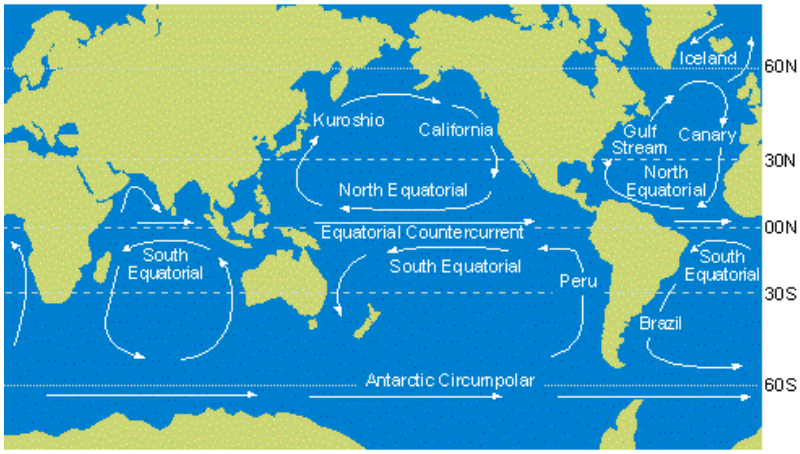

Figure 2.1: *The general circulation pattern. Differently from the tropical and subtropical gyres, the ACC is totally zonal and periodic.*

the one hand, by connecting all major ocean basins, the ACC plays a major role in the conveyor belt circulation and it represents the vehicle for the distribution of water mass properties, nutrients, and organisms within the Southern Ocean. On the other hand, the predominant zonality yields a partial thermal isolation of the Antarctic continent from warmer waters north of the ACC.

The main questions under debate in relation with the ACC dynamics can be summarized as follows.

1. What are the major forces driving the zonal current, and which is the predominant dissipative mechanism that prevents indefinite acceleration of the zonal flow, that is continuously fed by the westerly winds along the unclosed band?

2. How can meridional exchanges of heat, salt, nutrients and other chemical substances take place if the strong zonal ACC acts as a shield sep-

arating the polar region from subtropical region? In other words, how can a southward return flow across the ACC exist given that westerly winds drive a northward Ekman flux?

3. What is the physical mechanism responsible for the deep reaching current profile?

In the next sections these issues will be discussed in detail.

2.2.1 The Sverdrup theory

Before analyzing the results of our simulations, it is worth summarizing the theory of the large-scale wind-driven ocean circulation, evidencing how the circulation in the Southern Ocean is, dynamically speaking, significantly different from those of other oceanic basins. In all the major oceans which are zonally closed by lands, the general features of the time-mean wind-driven circulation can be explained using a simple steady, linear barotropic model in a rectangular basin. In the oceanic interior a relation exists between the vorticity input provided by the wind stress $\vec{\tau}$ and the meridional volume transport M_y. This is the *Sverdrup balance* given by (Pedlosky, 1987):

$$\beta M_y = curl_z \vec{\tau}\,, \tag{2.1}$$

in which β is the latitudinal variation of the Coriolis parameter f, where $f = f_0 + \beta y$.

Starting from the *momentum equation* in cartesian coordinate

$$\frac{\partial u}{\partial t} + u\frac{\partial u}{\partial x} + v\frac{\partial u}{\partial y} + w\frac{\partial u}{\partial z} - fv = -\frac{1}{\rho}\frac{\partial p}{\partial x} + T_x\,, \tag{2.2a}$$

$$\frac{\partial v}{\partial t} + u\frac{\partial v}{\partial x} + v\frac{\partial v}{\partial y} + w\frac{\partial v}{\partial z} + fu = -\frac{1}{\rho}\frac{\partial p}{\partial y} + T_y\,, \tag{2.2b}$$

$$\frac{\partial w}{\partial t} + u\frac{\partial w}{\partial x} + v\frac{\partial w}{\partial y} + w\frac{\partial w}{\partial z} = -\frac{1}{\rho}\frac{\partial p}{\partial z} - g + T_z\,, \tag{2.2c}$$

where T_i are the turbulent frictional forces per unit mass

$$T_i = A_H\left(\frac{\partial^2 u_i}{\partial x^2} + \frac{\partial^2 u_i}{\partial y^2}\right) + A_V\frac{\partial^2 u_i}{\partial z^2}\,,$$

and from the *continuity equation*

$$\frac{\partial u}{\partial x} + \frac{\partial v}{\partial y} + \frac{\partial w}{\partial z} = 0\,, \tag{2.3}$$

Sverdrup assumed that

- the flow is stationary, i.e. $\frac{\partial u_i}{\partial t} = 0\,$,
- the lateral friction is small, i.e. $A_H \left(\frac{\partial^2 u_i}{\partial x^2} + \frac{\partial^2 u_i}{\partial y^2} \right) \approx 0\,$,
- the flow is linear, i.e. $u\frac{\partial u_i}{\partial x} + v\frac{\partial u_i}{\partial y} + w\frac{\partial u_i}{\partial z} = 0\,$,
- the wind-driven circulation vanishes at some depth of no motion D, i.e. there is no interaction between the flow and the bottom topography (the bottom friction vanishes, and $A_V \frac{\partial^2 u_i}{\partial z^2}|_{z=-D} = 0\,$).

Under these assumptions, the horizontal components of the momentum equation (2.2) become

$$-fv = -\frac{1}{\rho}\frac{\partial p}{\partial x} + T_x\,, \tag{2.4a}$$

$$fu = -\frac{1}{\rho}\frac{\partial p}{\partial y} + T_y\,. \tag{2.4b}$$

Defining

$$\frac{\partial \overline{p}}{\partial x_i} = \int_{-D}^{0} \frac{\partial p}{\partial x_i}\, dz\,,$$

and defining the volume transports M_i in the wind-driven layer extending up to the assumed depth of no motion

$$M_i = \int_{-D}^{0} \rho u_i(z)\, dz\,,$$

by integrating over the depth equation (2.4), Sverdrup obtained

$$-fM_y = -\frac{\partial \overline{p}}{\partial x} + \tau_x\,, \tag{2.5a}$$

$$fM_x = -\frac{\partial \overline{p}}{\partial y} + \tau_y\,, \tag{2.5b}$$

This is because under the conditions of negligible lateral and bottom friction

$$\int_{-D}^{0} F_i \, dz = \int_{-D}^{0} A_H \left(\frac{\partial^2 u_i}{\partial x^2} + \frac{\partial^2 u_i}{\partial y^2} \right) dz + \int_{-D}^{0} A_V \frac{\partial^2 u_i}{\partial z^2} \, dz = \\ = 0 + \left[A_V \frac{\partial^2 u_i}{\partial z^2} \right]_{-D}^{0} = \frac{1}{\rho} \tau_i$$

since the horizontal boundary condition at the sea surface is the wind stress τ_i, and the stress at bottom boundary $-D$ is zero because the currents go to zero. Similarly, by integrating the continuity equation (2.3) over the depth, one gets

$$\frac{\partial M_x}{\partial x} + \frac{\partial M_y}{\partial y} = 0 \,, \tag{2.6}$$

as the vertical velocities must vanish at the surface and at the bottom. Differentiating (2.5a) with respect to y and (2.5b) with respect to x, subtracting, and using (2.6) we finally obtain (for the latitudinal component)

$$\beta M_y = \frac{\partial \tau_y}{\partial x} - \frac{\partial \tau_x}{\partial y} \,, \tag{2.7}$$

since $\beta = \frac{\partial f}{\partial y}$. This equation is the same as equation (2.1), i.e. the Sverdrup balance. The right hand side of (2.1) or (2.7) is the vorticity input by the wind stress, which has to be compensated by a change of vorticity of the water column (βM_y) that is induced to move meridionally. If, for example, the wind vorticity input is negative, fluid columns must move southward since their vorticity change is positive in that direction. It has to be noted that the Sverdrup balance takes into account only the interior part of the ocean basin. The pattern of the wind-driven gyre circulation is closed by an intensified *western boundary current* return flow which balances the net meridional mass transport in the ocean interior, thus satisfying mass conservation. In summary, a minimal theory of the wind-driven large-scale ocean circulation, which includes the Sverdrup flow in the oceanic interior and the associated frictional western boundary currents, is basically a linear vorticity balance and represents a valid diagnostic model for most of the large-scale ocean dynamics.

2.2.2 The limit of the Sverdrup theory

The Sverdrup theory is valid under the assumption of a flat bottom and it is applicable to closed basins, in which boundaries must limit a zonal flow, preventing the so-called *free mode* (Rintoul *et al.*, 2001). It holds in the interior of the subtropical gyres where the wind-driven circulation does not penetrate deep enough to interact with bottom topography, making the condition of flat-bottom an acceptable approximation. In the major ocean basins the deep circulation is effectively damped out by the propagation of baroclinic Rossby waves generated at the eastern side of the basin (Anderson and Gill (1975), Pedlosky (1987)), and the Sverdrup balance is therefore applicable. For its ubiquitous validity, the Sverdrup model is one of the cornerstones of theoretical oceanography.

However, the features of the Southern Ocean make its dynamics an outstanding exception, firstly, because of the absence of land at the latitudes of the Drake Passage, which does not allow a gyre regime to take place, and secondly because the flow is significant at all depths so that the circulation is strongly influenced by the bottom topography. In other words, for the Southern Ocean circulation, two conditions on which the Sverdrup theory is based are not satisfied.

Despite the apparent inadequacy of the Sverdrup assumption for the Southern Ocean, several modeling studies have attempted to generate a Sverdrup-like regime for the unbounded Antarctic region. Stommel (1957) suggested that the island arc located east of the Drake Passage could be considered as an effective extension of the Antarctic Peninsula, allowing only for a northward flow of the current. In this way, the general circulation would consist of a western boundary current in the western Argentine Basin and a corresponding southward Sverdrup return flow far from the coast. More specifically, the transport across the Drake Passage, being nearly equal to that of the flow moving northward along the Argentine coasts, would be balanced by the southward transport in the oceanic interior according to the Sverdrup relation. This hypothesis was confirmed by Baker (1982), who found good agreement when comparing the wind stress curl at 55 °S with transport measurements across the Drake Passage. Correspondingly, Webb (1993) and Ishida (1994) proposed similar models in which other topographic features, e.g. the Scotia Island Arch and the Kerguelen Plateau,

could act as a zonal constrain blocking the zonal flow and upsetting the Sverdrup balance (Figure 2.2). A detailed review of Sverdrup-like theories applied to the Southern Ocean is given by Hughes (2002). More recent promoters of Stommel's ideas are Warren *et al.* (1996).

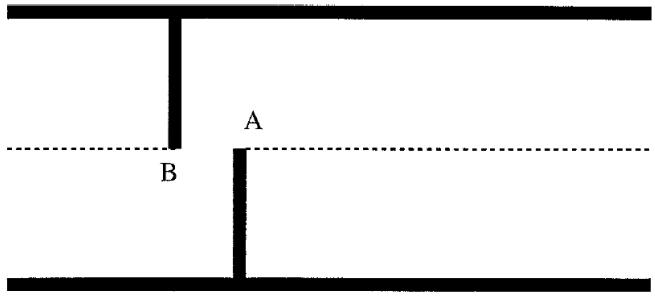

Figure 2.2: *Schematic of Sverdrup-like model of the ACC. The main topographic features such as the Kerguelen Plateau or the Scotia Island Arch could act as effective continents upsetting a Sverdrup regime.*

While a Sverdrupian regime in the Southern Ocean gives reasonable values for the ACC transport when combined with climatologial wind stress estimates, the theory is incomplete and many questions remain unsolved. The essential point is to find the right mechanism that balances the eastward momentum input due to the wind stress. In the following we will show how the *bottom form drag* firstly proposed by Munk and Palmen (1951) is the key for a theoretical explanation of the ACC dynamics.

2.3 The model

The numerical model used in this work is based on the Princeton Ocean Model (POM) developed by Blumberg and Mellor in 1977 and subsequently improved by the scientific community. The latest version (officially dated 2006) is the one used here. The POM is a sigma-coordinate, free surface, primitive equation model that contains a sub-model (Mellor and Yamada, 1982) for the turbulent vertical mixing. The sigma-coordinate system is based on the transformation given by

$$\sigma = \frac{z - \eta}{H + \eta}, \tag{2.8}$$

where z is the conventional vertical cartesian coordinate, $H = H(x,y)$ is the local depth dependent on the horizontal cartesian coordinates x and y, and $\eta = \eta(x,y,t)$ is the free surface elevation dependent on the position and on time t. In this way the *sigma* levels follow the bottom topography

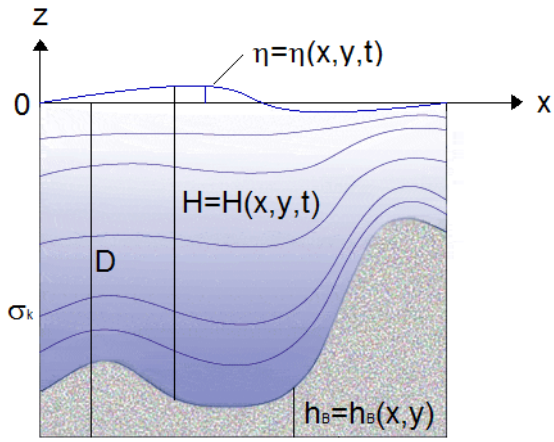

Figure 2.3: *Sketch of a vertical section of the terrain-following sigma-coordinates system.*

(Figure 2.3) and the value of σ ranges from 0 at $z = \eta$ to -1 at $z = H$. The model equations and the numerical techniques used to integrate them can be found in the POM Users Guide (Mellor, 2004) available online at http://www.aos.princeton.edu/WWWPUBLIC/htdocs.pom/PubOnLine/POL.html.

2.3.1 Model geometry

The model has been implemented in a domain that extends meridionally from 37 °S to 73 °S and zonally between 180 °W and 180 °E[1]: this domain is, in fact, a periodic zonal channel. The topography has been projected on a Mercator map by using ETOPO 5 data[2] (Figure 2.4), and an elementary rectangular grid has been used with a horizontal spatial resolution of 1/4°

[1]this domain is relative to the simulations presented in this chapter; in the following chapters simulations implemented in a different domain will be presented.

[2]available online at www.ngdc.noaa.gov

in latitude (y) and $1/2°$ in longitude (x)[3].

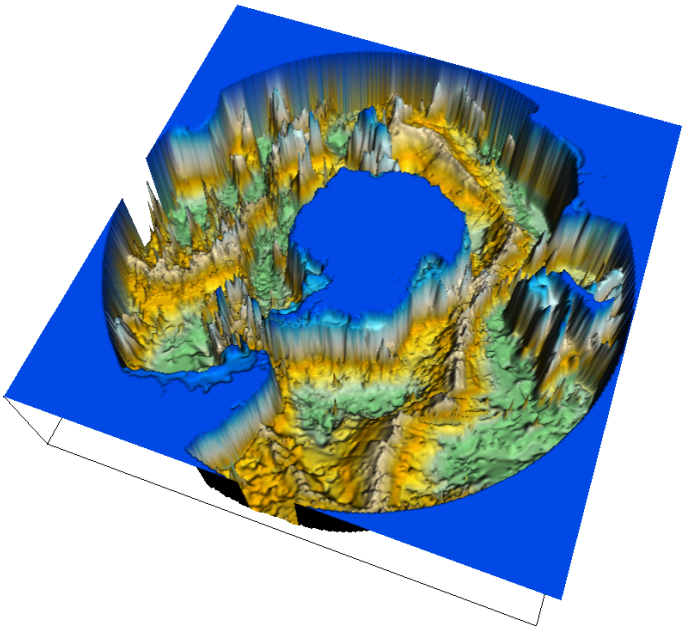

(a) *ETOPO 5 data.*

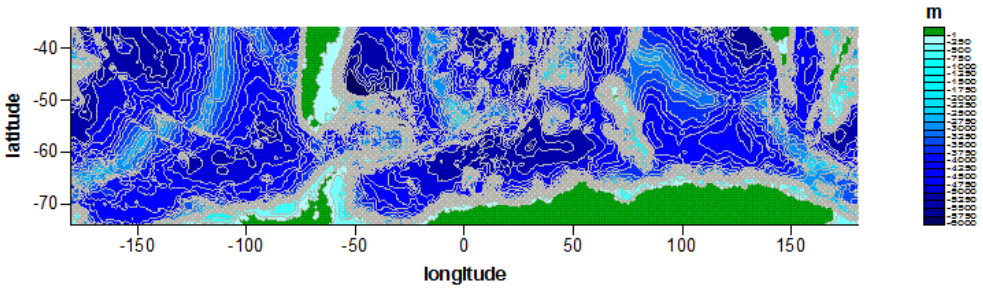

(b) *Projection on Mercator map.*

Figure 2.4: *The domain used: (top) the* 40 km *real data from ETOPO 5; (bottom) the projection on Mercator map (the gray lines indicate the isobaths of the smoothed bathymetry).*

In the first group of simulations (sim. 1-4) the topography is flat, in the second group (sim. 5-12) gaussian humps have been added, whereas in the third group (sim. 13-14) a real smoothed topography obtained from

[3]this resolution is relative to the simulations presented in this chapter; in the following chapters simulations implemented with a different resolution will be presented.

ETOPO5 40 km data has been considered (see Table 2.2).

Table 2.2: *Volume transport of the ACC diagnosed from some numerical models.*

Simulation	Mode	Topography	Lateral Friction
1	barotropic	flat bottom	$A_H = 1000\,\mathrm{m}^2/\mathrm{s}$
2	barotropic	flat bottom	$A_H = 10000\,\mathrm{m}^2/\mathrm{s}$
3	barotropic	flat bottom	$A_H = 25000\,\mathrm{m}^2/\mathrm{s}$
4	barotropic	flat bottom	$A_H = 100000\,\mathrm{m}^2/\mathrm{s}$
5	barotropic	with humps (400m)	$A_H = 1000\,\mathrm{m}^2/\mathrm{s}$
6	barotropic	with humps (400m)	$A_H = 10000\,\mathrm{m}^2/\mathrm{s}$
7	barotropic	with humps (400m)	$A_H = 25000\,\mathrm{m}^2/\mathrm{s}$
8	barotropic	with humps (400m)	$A_H = 100000\,\mathrm{m}^2/\mathrm{s}$
9	barotropic	with humps (800m)	$A_H = 1000\,\mathrm{m}^2/\mathrm{s}$
10	barotropic	with humps (800m)	$A_H = 10000\,\mathrm{m}^2/\mathrm{s}$
11	barotropic	with humps (800m)	$A_H = 25000\,\mathrm{m}^2/\mathrm{s}$
12	barotropic	with humps (800m)	$A_H = 100000\,\mathrm{m}^2/\mathrm{s}$
13	barotropic	real (smoothed)	$A_H = 1000\,\mathrm{m}^2/\mathrm{s}$
14	baroclinic	real (smoothed)	$A_H = 1000\,\mathrm{m}^2/\mathrm{s}$

2.3.2 Initial conditions, forcing and boundary conditions

Starting from an ocean at rest, we have forced the system with a purely zonal, idealized wind stress based on real observed data, as done by Pierini (2005) with a 3-layer shallow water model. The wind is steady and its magnitude varies as a function of latitude (Figure 2.5). The water has a constant density in the barotropic simulations, whereas a background stratification has been imposed in the baroclinic simulations. We will see that such a background stratification takes into account not only the vertical, but also the meridional density gradient.

In order to sustain the prescribed background stratification, an idealized heat flux at the sea surface has also been imposed in the baroclinic simulations. In this way it is possible to prevent a *total mixing*, which would lead to vanishing meridional density gradient due to the vertical mixing provided

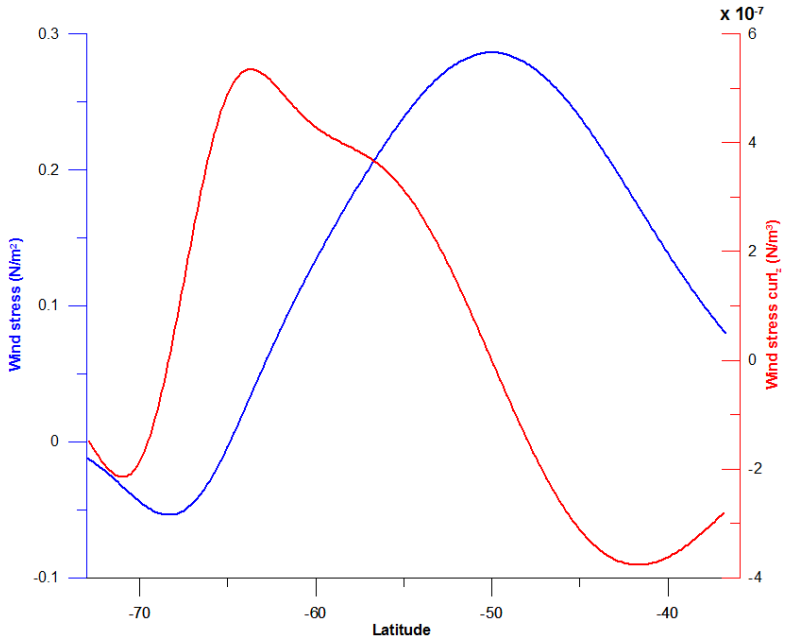

Figure 2.5: *Profile of the adopted idealized wind stress (blue) with the corresponding vertical component of the wind stress curl (red). The latitude of vanishing curl is at* $50\,^{\circ}S$*, and the westerly wind switches into easterly south of* $65\,^{\circ}S$*.*

by the sub-model.

Thanks to the choice of a closed zonal channel, periodic boundary conditions have been imposed along the western and eastern boundaries, i.e., grid points on one edge have been treated as points adjacent to those on the opposite edge. On the northern and southern boundaries, on the other hand, free-slip boundary conditions have been imposed at all depths.

2.4 Barotropic model results

The barotropic model for the ACC represents our first step toward a description of the dynamical processes governing the circulation. Following the classical diagnostic discussion (see Dijkstra, 2008), neglecting the inertial terms (which in effect are of a lower order of magnitude in the implemented

model), the momentum equations for a steady constant density flow are

$$-fv = -\frac{1}{\rho}\frac{\partial p}{\partial x} + A_V\frac{\partial^2 u}{\partial z^2} + F_x\,, \tag{2.9a}$$

$$fu = -\frac{1}{\rho}\frac{\partial p}{\partial y} + A_V\frac{\partial^2 v}{\partial z^2} + F_y\,, \tag{2.9b}$$

$$0 = -\frac{\partial p}{\partial z} - \rho g\,, \tag{2.9c}$$

where F_i are the lateral friction terms, and the continuity equation is

$$\frac{\partial u}{\partial x} + \frac{\partial v}{\partial y} + \frac{\partial w}{\partial z} = 0\,. \tag{2.10}$$

Assuming that the sea surface height is small, the boundary conditions at the sea surface and at the bottom are:

$$z = 0 : \tau_x = \rho A_V\frac{\partial u}{\partial z};\ \tau_y = \rho A_V\frac{\partial v}{\partial z};\ w = 0\,, \tag{2.11a}$$

$$z = -H \approx -D + h_B : \frac{\mathrm{d}H}{\mathrm{d}t} = 0;\ \vec{t}_1\cdot\vec{u} = 0;\ \vec{t}_1\cdot\vec{u} = 0\,, \tag{2.11b}$$

where $\vec{t}_1$ and $\vec{t}_2$ are the tangent vectors at the bottom: the velocity component normal to the surface and to the bottom must vanish.

Results for three different barotropic cases will now be discussed.

2.4.1 Flat bottom case

The simplest model domain consists of an idealized channel with real coastline and flat bottom ($H(x,y) = D = 4000\,\mathrm{m}$):

$$H(x,y) = \begin{cases} 0, & \text{on land,} \\ 4000, & \text{elsewhere .} \end{cases}$$

Four different simulations have been performed in this context varying the lateral viscosity coefficient A_H.

In the flat bottom case, from the boundary conditions (2.11a) we have that the vertical velocity must vanish at the bottom: $w = 0$ at the bottom

$z = -H = -D$. By integrating the equations (2.9a, 2.9b, 2.10) over the depth we find

$$-fV = -\frac{1}{\rho}\frac{\partial P}{\partial x} + \frac{\tau_x}{\rho} - \frac{\tau_b}{\rho} + \overline{F_x}\,, \tag{2.12a}$$

$$fU = -\frac{1}{\rho}\frac{\partial P}{\partial y} + \frac{\tau_y}{\rho} - \frac{\tau_b}{\rho} + \overline{F_y}\,, \tag{2.12b}$$

$$0 = \frac{\partial U}{\partial x} + \frac{\partial V}{\partial x}\,, \tag{2.12c}$$

where τ_b is the bottom stress and

$$U_i = \int_{-H}^{0} u_i\, dz\,, \tag{2.13a}$$

$$\overline{F_i} = \int_{-H}^{0} F_i\, dz\,, \tag{2.13b}$$

$$P = \int_{-H}^{0} p\, dz\,. \tag{2.13c}$$

If we then integrate equation (2.12c) over the zonal direction and use the periodicity of the boundary conditions we find, at every latitude,

$$\oint \frac{\partial V}{\partial y}\, dx = -\oint \frac{\partial U}{\partial x}\, dx = 0 \Rightarrow \frac{\partial}{\partial y}\oint V\, dx = 0 \Rightarrow \oint V\, dx = 0, \tag{2.14}$$

The circumpolar integral of (2.12a) then becomes

$$0 = \oint \frac{\tau_x}{\rho}\, dx - \oint \frac{\tau_b}{\rho}\, dx + \oint \overline{F_x}\, dx. \tag{2.15}$$

Hence, neglecting the bottom friction, the wind stress input has to be balanced by lateral friction. If we denote by $[\tau]$,$[\rho]$,$[U]$,$[L]$,$[D]$ the characteristic orders of magnitude of the wind stress, density, zonal velocity, and basin and depth lengths, respectively, from the balance between the wind stress term and the lateral friction the following balance can be derived,

$$\frac{[\tau_x]}{[\rho]} = \frac{[A_H][U][D]}{[L^2]}, \tag{2.16}$$

which can be written as

$$[U] = \frac{[\tau][L^2]}{[A_H][\rho][D]}.$$

For values $[L] = O(10^7)\,\mathrm{m}$, $[D] = O(10^3)\,\mathrm{m}$, and $[\tau] = O(10^{-1})\,\mathrm{m^2/s}$ the characteristic total zonal transport $[\Phi]$ across two latitudes y_1 and y_2 is

$$[\Phi] = \int_{y_2}^{y_1} [U][D]\,dy = \frac{10^7 L_y}{[A_H]}, \tag{2.17}$$

where $L_y = \int_{y_2}^{y_1} dy$ is the distance between two latitudes. For the Drake Passage, where $[L_y] = O(10^6)\,\mathrm{m}$, we would have:

$$[\Phi] = \frac{10^{13}}{[A_H]}, \tag{2.18}$$

so, to get realistic values of $[\Phi]$, i.e. $O(10^2)$ Sv, we would need abnormally high values for A_H, i.e. $[A_H] = O(10^5)\,\mathrm{m^2/s}$.

The results of the simulations for the flat bottom case confirm, indeed, this analysis: in order to reproduce an acceptable volume transport across the Drake Passage one needs extremely high values of the eddy viscosity A_H, but this would result in unrealistic high transports (see also Figure 2.7). This is the so-called *Hidaka's dilemma* (Hidaka and Tsuchiya (1953); Wolff *et al.* (1996)); similar results have been obtained by using a three-layer *shallow water* model in previous studies (Pierini, 2005; Sgubin, 2008). Moreover, in the flat bottom case we found some hints of a Sverdrup-like regime only in the regions limited by continents, e.g. the Antarctic Peninsula and South America. In the unbounded latitudinal band such a dynamics is not expected to hold, and the flow is periodically zonal (Figure 2.6). In summary, a barotropic flat bottom channel model cannot provide a realistic ACC transport.

2.4.2 Flat bottom with humps: the role of the bottom topography

In the second group of barotropic experiments, four idealized humps have been introduced in the otherwise flat bottom topography: they have been roughly located where the ACC encouters the main topographic fea-

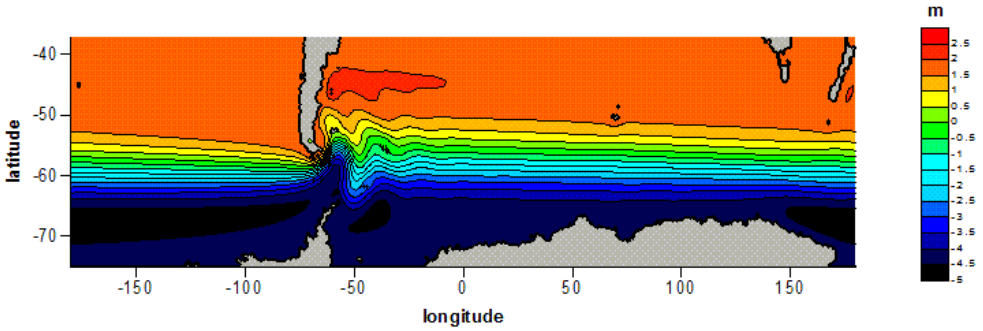

(a) $A_H = 10000\,\mathrm{m}^2/\mathrm{s}$.

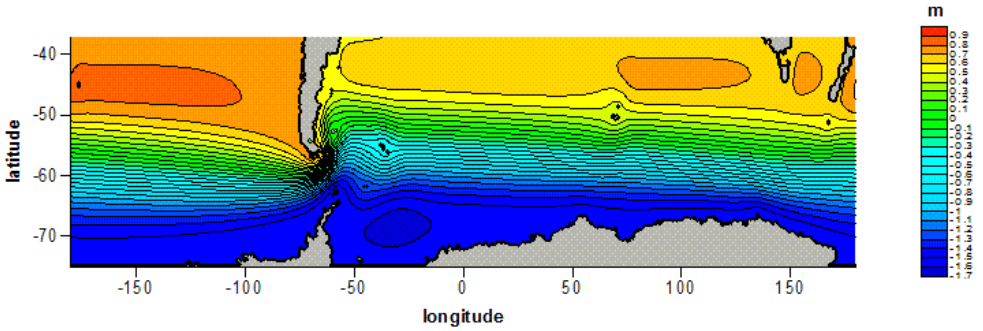

(b) $A_H = 100000\,\mathrm{m}^2/\mathrm{s}$.

Figure 2.6: *Mean Sea Surface Height (SSH) fields for two simulations in the flat bottom case.*

tures, e.g. the Mid-Atlantic Ridge, the Kerguelen Plateau, the Pacific-Antarctic Ridge, the East-Pacific Ridge. The humps have the following *Gaussian* shape:

$$H(x,y) = \begin{cases} 0, & \text{if there is land}, \\ 4000 - h_b = 4000 - \sum_k h_0^k \, e^{-\left[\left(\frac{x-x_c^k}{\delta x}\right)^2 + \left(\frac{y-y_c^k}{\delta y}\right)^2\right]}, & \text{elsewhere.} \end{cases}$$

where $k = 1,4$, h_0^k are the humps heights at their top located at $(x_c^k; y_c^k)$ on the grid, and δ_x^k and δ_y^k are the humps widths in the x and y directions, respectively .

As it can be seen from Figure 2.7, the introduction of a simple bottom topography changes the features of the flow rather significantly: the net zonal transports clearly decrease with respect to those in the flat bottom case,

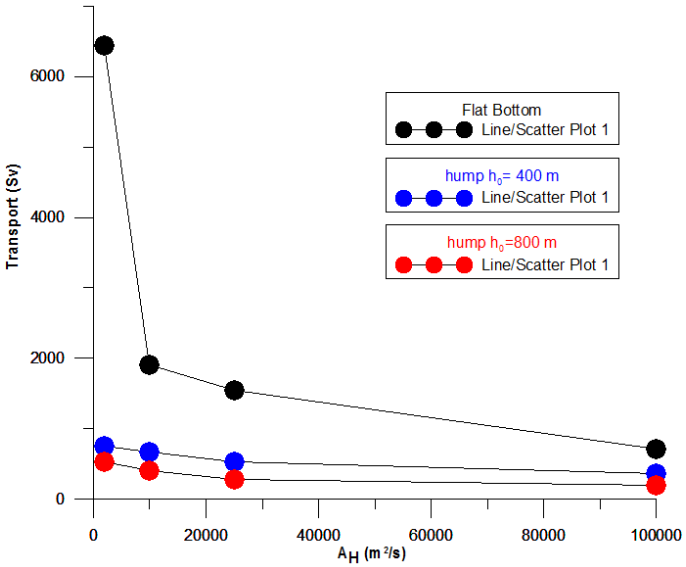

Figure 2.7: *The net zonal transport across the Drake Passage for different values of A_H in the flat bottom case (black line) and in the humps configuaration (blue and red lines). The effect of the bottom topography on the significant decrease in flow transport is evident. In the flat bottom case, to obtain a realistic order of magnitude for the transport, i.e. $O(10^3)$ Sv, an unrealistically high value of A_H is needed: $A_H = O(10^5)$ m^2/s.*

yielding values of $O(10^2)$ Sv which are much more realistic. To understand why that happens we again integrate the equations (2.9) over the depth z. In this case $H(x,y) \neq cost$, so the integral of $\partial p/\partial x_i$ cannot be treated as in the flat bottom case. For the Leibnitz's theorem

$$\frac{\mathrm{d}}{\mathrm{d}x}\int_{f(x)}^{g(x)} F(x,t)\,dt = F(x,g(x))\frac{\mathrm{d}g}{\mathrm{d}x} - F(x,f(x))\frac{\mathrm{d}f}{\mathrm{d}x} + \int_{f(x)}^{g(x)} \frac{\partial F}{\partial x}(x,t)\,dt.$$

Thus, assuming that the sea surface displacements are negligible with respect to the bottom variations, we have

$$\int_{-H(x_i)}^{0} \frac{1}{\rho}\frac{\partial p}{\partial x_i}(x_i,z)\,dz = \frac{\mathrm{d}}{\mathrm{d}x_i}\int_{-H(x_i)}^{0} \frac{1}{\rho}p(x_i,z)\,dz - \frac{p}{\rho}(x_i,-H(x_i))\frac{\partial H}{\partial x_i}(x_i)\,, \quad (2.19)$$

where the second member on the l.h.s. is the so-called *bottom form drag*, which vanishes only if the bottom is flat. Taking into account equations (2.13), the integrated governing equations (2.12) has to be rewritten for varying bottom topography as

$$-fV = -\frac{1}{\rho}\left(\frac{\partial P}{\partial x} - p|_{z=-H}\frac{\partial H}{\partial x}\right) + \frac{\tau_x}{\rho} - \frac{\tau_b}{\rho} + \overline{F_x}\,, \tag{2.20a}$$

$$fU = -\frac{1}{\rho}\left(\frac{\partial P}{\partial y} - p|_{z=-H}\frac{\partial H}{\partial y}\right) + \frac{\tau_y}{\rho} - \frac{\tau_b}{\rho} + \overline{F_y}\,, \tag{2.20b}$$

$$0 = \frac{\partial U}{\partial x} + \frac{\partial V}{\partial x}\,. \tag{2.20c}$$

The circumpolar integral of (2.20a) along a latitude around the Southern Ocean is (neglecting the bottom friction)

$$0 = \oint \frac{\tau_x}{\rho}\,dx + \frac{1}{\rho}\oint p_B\frac{\partial H}{\partial x}\,dx + \oint \overline{F_x}\,dx, \tag{2.21}$$

where, hereinafter

$$p_B = p|_{z=-H}.$$

This implies that the wind stress, which drives the ACC, is balanced by bottom form drag

$$f_D = \frac{1}{\rho}p_B\frac{\partial H}{\partial x} = -\frac{1}{\rho}p_B\frac{\partial h_B}{\partial x}$$

over topographic ridges, and by lateral friction. As the latter is not of significant magnitude, we can argue that the form stress is the main mechanism that balances the momentum input by the wind stress. It should be noted that the form drag is not properly a *stress* since it is associated with pressure gradients in the presence of bottom topography, but it does represent the way in which zonal momentum is extracted from the fluid by the solid earth, like a frictional force does.

The form drag mechanism represents the cornerstone of many hydrodynamical applications, such as the airplane take-off. Moreover, in atmospheric science the importance of the form drag is well known, since it generates a pressure drop as winds pass over mountains which force the wind to slow down. A similar mechanism must occur in the ocean when the flow crosses a

topographic feature, creating a difference of pressure between the upstream and the downstream region, which tends to decelerate the flow across the obstacle.

The balance between the wind stress and the bottom form drag was first suggested by Munk and Palmen (1951): they estimated that the pressure difference across each of the four major ridges (the Scotian Arc, the Kerguelan Plateau, the Macquarie Ridge and the South Pacific Ridge) could be sufficient to balance the zonal wind stress. The use of high resolution models has more recently confirmed such a balance (Ivchenko *et al.*, 1991; Treguier and Mc Williams, 1990; Gille, 1997).

The bottom form drag acts everywhere in the ocean where the variable bathymetry is present, but to be significant the pressure gradient at the bottom must be out of phase with the depth along the flow. To understand the effect of the bottom form drag in the dynamical balance, let us split the ocean into three layers (not necessarily differently stratified) as follow:

- the upper layer δ_1, which corresponds to the Ekman layer (from $z == 0$ to $z = -h_1$)
- the intermediate layer δ_2, which extends from the Ekman layer edge to the top of the highest topographic feature (from $z = -h_1$ to $z = -h_2$)
- the lower layer δ_3, which reaches the bottom topography (from $z = -h_2$ to $z = -H = -D + h_B$)

Taking into account equation (2.14) it is clear that

$$\oint V\,dx = \oint V_1\,dx + \oint V_2\,dx + \oint V_3\,dx = 0,$$

where

$$\oint V_i\,dx = \oint \int_{\delta_i} v\,dzdx.$$

Let us consider the zonal integral along a parallel of the balance of the vertically integrated zonal momentum (2.20a) and neglecting the lateral and the

bottom friction, we have for each layer

$$-f \oint V_1 \, dx = \oint \frac{\tau_x}{\rho} \, dx, \tag{2.22a}$$

$$-f \oint V_2 \, dx = 0 \,, \tag{2.22b}$$

$$-f \oint V_3 \, dx = \frac{1}{\rho} \oint p_B \frac{\partial H}{\partial x} \,, \tag{2.22c}$$

since the pressure gradients have to vanish due to the periodic boundary conditions. In the Ekman layer this means that we have a net northward transport, since f is negative and the zonal eastward wind τ_x is positive. On the other hand, in the intermediate layer there is no net meridional transport since the wind stress is assumed to be negligible outside the Ekman layer, and there is no direct interaction with the bottom topography. The equatorward Ekman transport in the first layer is eventually balanced in the third layer, where the r.h.s. of (2.22c) must be negative. This yields a southward transport in the abyssal layer which closes both the dynamical and mass balances.

In more detail, let us consider two coordinate planes $z = -H_1(x)$ and $z = -H_2(x)$, as sketched in the lower-right panel of Figure 2.8. Let x_w and x_e be two points located along the zonal flow west and east of a topographic feature, respectively. Remembering the Leibnitz's theorem, we have

$$\int_{x_w}^{x_e} \int_{-H_2}^{H_1} \frac{\partial p}{\partial x} \, dz \, dx = P_e - P_w + \int_{x_w}^{x_e} \left(p(x, -H_1) \frac{\partial H_1}{\partial x} - p(x, -H_2) \frac{\partial H_2}{\partial x} \right) dx, \tag{2.23}$$

where

$$P = \int_{-H_2}^{H_1} P \, dz.$$

The term $P_e - P_w$ in the r.h.s. of (2.23) is the net forcing due to the pressure gradients between x_w and x_e, whereas the integral represents the flux of horizontal momentum through the surfaces $z = -H_1(x)$ and $z = -H_2$. For a zonally unbounded ocean, by using the periodic boundary condition $P_w = P_e$, the first term on the r.h.s. of (2.23) is zero, and the net pressure

forcing is due only to the integral terms. If we consider H_1 as the ocean surface and H_2 as the bottom floor, and assume anomalies of the free surface δH_1 with respect to bottom topography anomalies δH_2, , we get that:

- $\oint \left(p(x,-H_1)\partial H_1/\partial x - p(x,-H_2)\partial H_2/\partial x\right)\, dx < 0$ when the layer thickness decreases,

- $\oint \left(p(x,-H_1)\partial H_1/\partial x - p(x,-H_2)\partial H_2/\partial x\right)\, dx > 0$ when the layer thickness increases,

since the bottom pressure anomalies have the same sign as the surface pressure anomalies. As the pressure distribution is out of phase with the topography (Figure 2.8), this explains the decrease of the transport due to the bottom topography: there is a momentum transfer from the ocean water to the bottom topography. This is also related to the fact that a northward flow occurs over the topographic features, whereas a southward flow takes place where the layer thickness increases (Figure 2.8).

Moreover, H_1 and H_2 can also be considered two isopycnal surfaces in a stratified ocean. In such a case there is a horizontal momentum transfer from the two density surfaces: this is the so called *interfacial form stress*, which represents the mechanism allowing the wind stress imparted on the sea surface to reach the deep ocean. Through the interfacial form stress, each layer gains x-momentum from the fluid above and loses x-momentum to the fluid below. Such a process is driven by eddies which are able to tilt isopycnals with a consequent fluctuation of the zonal pressure gradients..

In summary, such an analysis provides possible answers to the three questions of page 25: it has been shown: (question 1) how the zonal wind stress input is likely to be balanced at the bottom by the bottom form drag, (question 2) the role of the interfacial form drag in transferring momentum at depth, and (question 3) how a net meridional water exchange can be possible through northward-southward thickness fluxes across the predominantly zonal ACC.

Figure 2.9 shows the resulting *Sea Surface Height* (SSH) field for two different humps. As we are far away from the equator, the relative vorticity ζ can be neglected with respect to the planetary vorticity f, and the potential

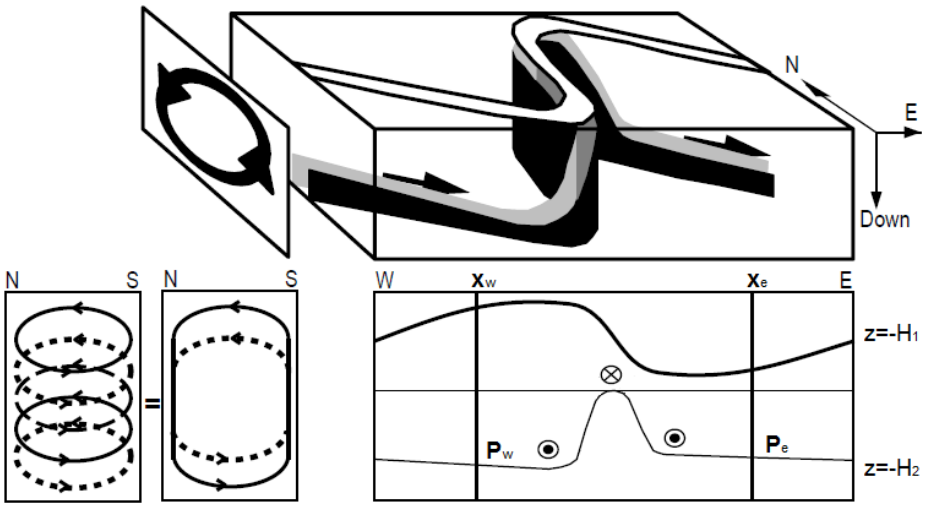

Figure 2.8: *Schematic representation of the form drag contribution. The trajectory of a water particle is shown in three dimensions when the surface H_1 (which could be the free surface or an isopycnal surface) is out of phase with the surface H_2 (which could be the bottom topography or a deeper isopycnal surface). The flow is diverted by the tilted H_2 creating a low pressure zone downstream of the H_2 anomaly. Such a pressure gradient leads a net eastward pressure force flux from H_1 to H_2, i.e. the form drag, which acts as a stress transferring momentum downward. This is the central mechanism that allow the wind stress at the surface to communicate al great depth where, eventually, is removed by the bottom topography. The resulting circulation integrated at constant latitude and depth is a meridional overturning cell, which guarantees water exchanges between different latitudes. Redrawn from Rintoul et al. (2001)*

.

vorticity conservation law

$$\Pi = \frac{f+\zeta}{H} = const$$

reduces to

$$\Pi = \frac{f}{H} = const.$$

The net flow tends indeed to follow the geostrophic contours f/H, as it is shown. It is worth mentioning that the ACC is not zonally homogeneous

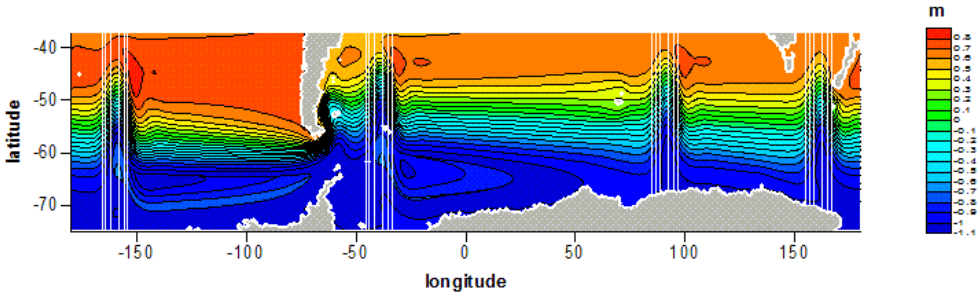

(a) $h_0 = 400\,\mathrm{m}$; $A_H = 1000\,\mathrm{m}^2/\mathrm{s}$.

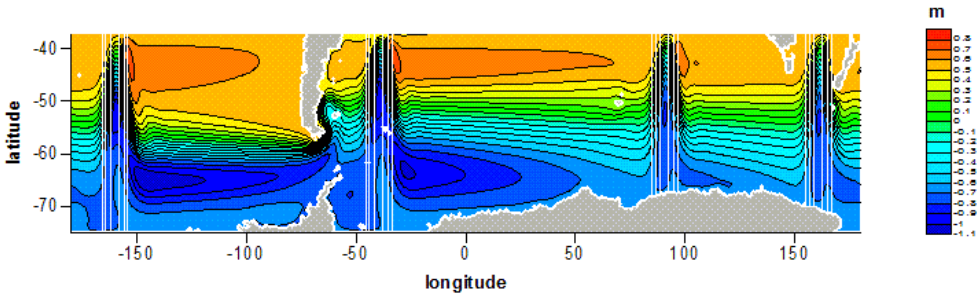

(b) $h_0 = 800\,\mathrm{m}$; $A_H = 25000\,\mathrm{m}^2/\mathrm{s}$.

Figure 2.9: *Mean SSH fields for two simulations in the flat bottom with humps case.*

and may contain regions of northward Sverdrup flow balanced by poleward flow in boundary currents along the edges of the ridges. However, we have seen that the form drag is the leading process in the momentum balance, the Sverdrup theory representing only very partially the dynamics of the ACC.

2.4.3 Realistic topography in the barotropic mode: the topographic steering

In view of the importance of bottom topography in the dynamics of the ACC, the next step toward a more realistic definition of the Southern Ocean circulation is the introduction of a realistic topography. Figure 2.10 shows the mean SSH with real smoothed bottom topography. The flow is clearly predominantly driven by the bottom topography, and the resulting transport across the Drake Passage is much smaller (25 Sv) than the observed one (130 Sv). The mean ACC loses its predominantly zonal structure, as se-

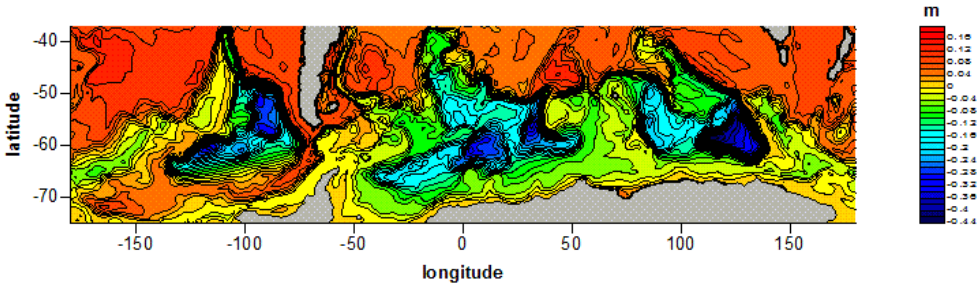

Figure 2.10: *Mean SSH field for a not stratified ocean with real smoothed bottom topography.*

ries of gyres trapped around the main submarine basins appear. This is due to the so-called *topographic steering*, which takes place in the absence of baroclinicity, and consists of a circulation blocked by geostrophic contours. Such a process is very important particularly at high latitudes, where the ocean is weakly stratified and geophysical flows tend to be vertically coherent (or barotropic). In a homogeneous zonally periodic channel with topography, Krupitsky and Cane (1994) identified two different dynamical regimes depending on the height $\widetilde{H}$ of meridional topographic obstacles placed across the channel. Below a critical value of $\widetilde{H}$, a strong zonal flow takes place, whereas if such a threshold is crossed, no circumpolar current exists, as our results show as well. In reality, since the ocean is stratified, baroclinic compensation occurs and velocities tend to decrease with depth, so the flow does not follow the f/H contours (Hughes and Killworth, 1995; Marshall, 1995b) exactly. By assuming a velocity decrease with depth with a fixed *e-folding* scale H_s (in agreement with Gille, 2003) such as

$$u(z) = u|_{z=0}\, e^{-z/H_s},$$

the flow is predicted to follow the f/F_s contours (Marshall, 1995a), where

$$F_s = H_s(1 - e^{-H/H_s}).$$

Under these assumptions Krupitsky *et al.* (1996) developed an equivalent barotropic model of the ACC by effectively reducing the height of topographic elevations. The equivalent barotropic model is quantitatively assessed by Ivchenko *et al.* (1999) and Cane *et al.* (1995) which obtained a good

agreement with the observed zonal transport by assuming the equivalent barotropic structure of the flow.

2.5 Baroclinic model results

In the last part of simulations, the role of the stratification for the Southern Ocean circulation has been considered, and a general vertical density gradient has been imposed along the depth which has been split into 7 equidistant *sigma* levels.

The water in the Antarctic region is strongly cooled by the atmosphere and by the sea-ice formation. In general this yields denser water at higher latitudes with respect to lower latitudes. Thus, in order to study the basic effects of stratification in the ACC dynamics, apart from an increase in density with depth, a general meridional density gradient must be taken into account.

For this reason, a new initialization for the background density distribution has been considered in the model, with stronger vertical stratification at lower latitudes. This has been achieved by varying the temperature profile as a function of latitude φ, as illustrated in Figure 2.11. The salinity, on the other hand, has been assumed constant for each point and at each depth.

In order to maintain the features of such a general background stratification, besides the wind stress field, an idealized steady sea-air heat flux field has been imposed as a further boundary condition (vanishing net heat flux over the whole domain is also imposed). The water thus loses heat at higher latitudes and gains heat at lower latitudes. In this way, it is possible to prevent a total mixing of the water that would follow as a consequence of the POM turbulent mixing sub-model. So, the initial background stratification can be generally sustained over the time of integration.

2.5.1 Realistic topography in the baroclinic mode: the role of the stratification

The initial density distribution imposed through an initial temperature field is

$$\rho = \rho(y, z) = \rho_0 + A(y) + B(z),$$

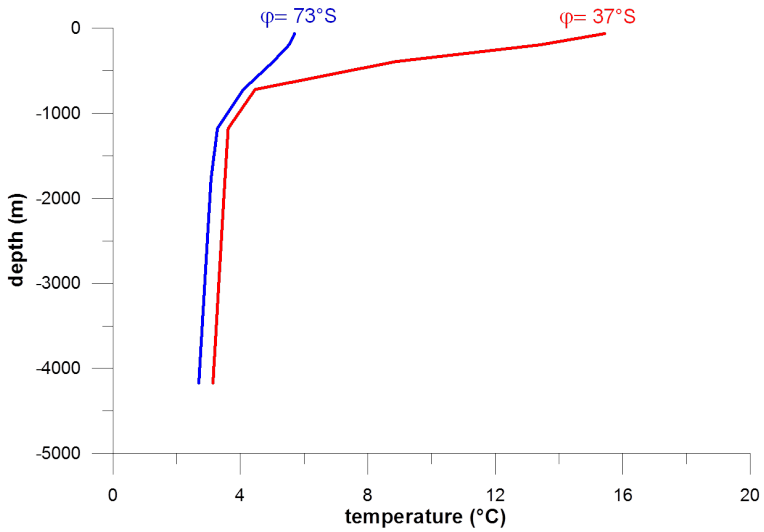

Figure 2.11: *Vertical profile of the temperature for the northernmost point at $\varphi = 37$ °S (red line) and for the southernmost point at $\varphi = 73$ °S (blue line). The salinity is everywhere constant . A meridional density gradient at each depth is therefore present.*

where ρ_0 is the density at the surface of a northernmost point, and $A(y)$ and $B(z)$ are two functions of the latitude y and of the depth z respectively, so that the density increases with depth and poleward.

Figure 2.12 shows that the obtained transport across the Drake Passage is consistent with the observed 130 Sv. Moreover, there is evidence for a variability in the ACC flow, as the transport is not constant after the spin-up but, differently from the barotropic mode, it fluctuates around a mean value. Since the forcing is steady, these oscillations must be intrinsically generated by mechanisms internal to the ocean. The variability obtained is likely to be related to the generation of eddies along the ACC which, in the presence of stratification, is subjected to baroclinic instability. Standing and transient eddies, as already mentioned, play an important role in the downward momentum transfer, as they trigger the interfacial form stress, and in the meridional thermodynamical balance as well, as they provide heat exchange between higher and lower latitudes. A more detailed analysis on the intrinsic variability associated with the ACC will be presented in the next chapter.

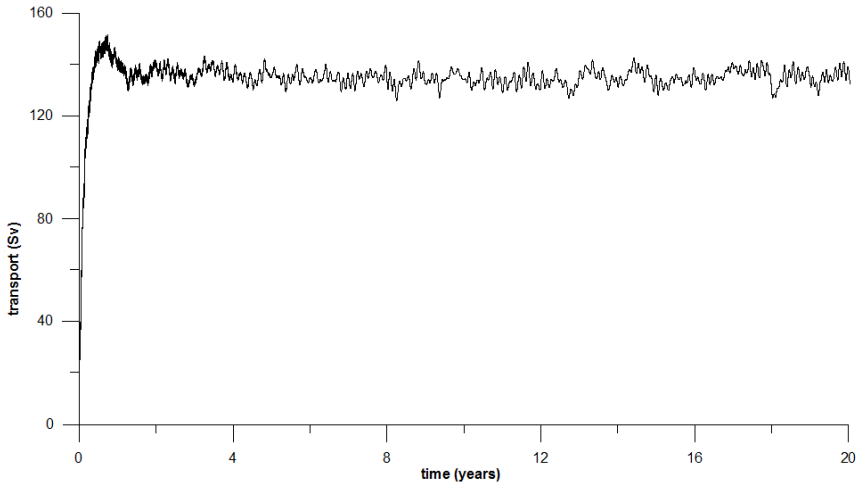

Figure 2.12: *Time series of the simulated zonal transport*

A comparison between the obtained SSH field, which is indicative of the fronts position, and the estimated location of the Polar Front, evidences a very good agreement (Figure 2.13).

To understand physically why in the stratified ocean the flow is able to cross the geostrophic contours differently from the barotropic configuration, where the circulation is controlled by the main topographic features, we start from the equations for the baroclinic momentum balance in the *Boussinesq approximation* which, after neglecting the nonlinear and lateral friction terms, are

$$-fv = -\frac{1}{\rho_0}\frac{\partial p}{\partial x} + A_V\frac{\partial^2 u}{\partial z^2} + F_x\,, \tag{2.24a}$$

$$fu = -\frac{1}{\rho_0}\frac{\partial p}{\partial y} + A_V\frac{\partial^2 v}{\partial z^2} + F_y\,, \tag{2.24b}$$

$$g\frac{\rho-\rho_0}{\rho_0} = -\frac{\partial p}{\partial z} - g\,, \tag{2.24c}$$

where ρ_0 is a constant reference density. It should be noted that differences between equations (2.24) for a stratified fluid and equations (2.9) for a homogeneous fluid are limited to the z-component. By introducing the *baroclinic*

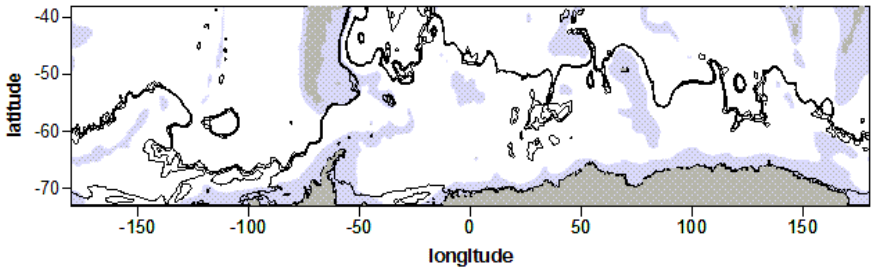

(a) Simulated Polar Front position.

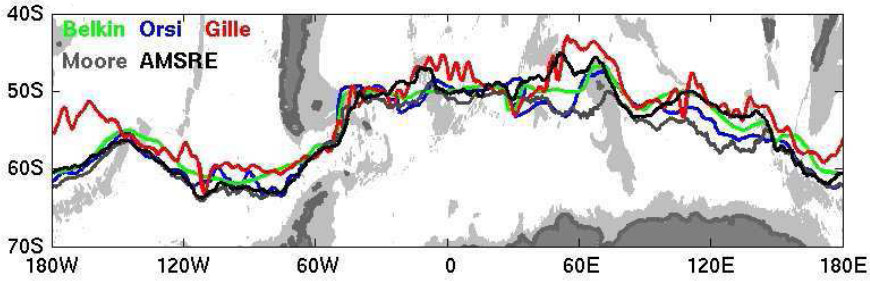

(b) Observed Polar Front position.

Figure 2.13: *Comparison between the simulated and observed position of the Polar Front.*

potential energy

$$\chi = \frac{g}{\rho_0} \int_{-H}^{0} z(\rho - \rho_0)\, dz\,, \tag{2.25}$$

if we multiply (2.24c) by z and integrate over the depth we get

$$\chi = -\int_{-H}^{0} \frac{z}{\rho_0} \frac{\partial p}{\partial z}\, dz = \frac{1}{\rho_0}(H p_B - P)\,. \tag{2.26}$$

The depth averaged horizontal momentum equations can then be derived from (2.24) by making use of (2.13):

$$-\frac{f}{H}V = -\frac{1}{H\rho_0}\left(\frac{\partial P}{\partial x} - p_B \frac{\partial H}{\partial x}\right) + \frac{\tau_x}{H\rho_0}\,, \tag{2.27a}$$

$$-\frac{f}{H}U = -\frac{1}{H\rho_0}\left(\frac{\partial P}{\partial y} - p_B \frac{\partial H}{\partial y}\right) + \frac{\tau_y}{H\rho_0}\,. \tag{2.27b}$$

From equation (2.26) we obtain

$$\rho_0 \frac{\partial \chi}{\partial x_i} = p_B \frac{\partial H}{\partial x_i} + H \frac{\partial p_B}{\partial x_i} - \frac{\partial P}{\partial x_i}. \tag{2.28}$$

where we can rewrite the pressure terms in (2.27a) and (2.27b) as

$$\frac{\partial P}{\partial x_i} - p_B \frac{\partial H}{\partial x_i} = H \frac{\partial p_B}{\partial x_i} - \rho_0 \frac{\partial \chi}{\partial x_i}.$$

Subtracting the x-derivative of (2.27b) from the y-derivative of (2.27a) we eventually obtain the *vorticity equation for the steady state depth averaged flow*

$$\nabla \cdot \left(\frac{f}{H} \vec{U} \right) = J\left(\chi, \frac{f}{H} \right) + \nabla \cdot \left(\frac{f}{H} \vec{M}^E \right), \tag{2.29}$$

where $J(A, B)$ is the Jacobian operator

$$J(A, B) = \frac{\partial A}{\partial x} \frac{\partial B}{\partial y} - \frac{\partial B}{\partial x} \frac{\partial A}{\partial y},$$

and

$$M_x^E = \frac{\tau_y}{\rho_0 f}, \quad M_y^E = -\frac{\tau_x}{\rho_0 f},$$

are the *Ekman transports*. From the rule $\nabla \cdot (a\vec{u}) = a \nabla \cdot \vec{u} + \nabla a \cdot \vec{u}$, where a is a generic scalar and $\vec{u}$ a generic vector, it follows that the equation (2.29) can be written in the equivalent way as

$$\nabla \left(\frac{f}{H} \right) \cdot \vec{U} = J\left(\chi, \frac{f}{H} \right) + \nabla \cdot \left(\frac{f}{H} \vec{M}^E \right), \tag{2.30}$$

since $\nabla \cdot \vec{u} = 0$ for the continuity equation.

In absence of stratification $J(\chi, 1/H)$ vanishes and, neglecting the Ekman transport contribution, the (2.30) indicates that the transport $\vec{U}$ is perpendicular to the gradient of geostrophic contours f/H, i.e. the transport is tangent to the geostrophic contours (that is what we found in the barotropic simulations). When a stratification is imposed, it must be taken into account the

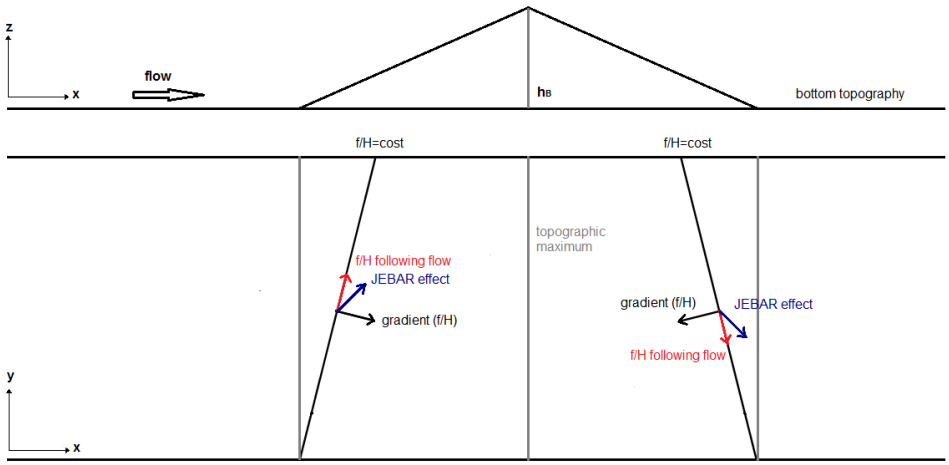

Figure 2.14: *Sketch of the JEBAR effect in a baroclinic flow over a topographic obstacle. If there is a meridional density gradient, with southern water denser than northern water, the mean barotropic flow parallel to the geostrophic contours (constant f/h lines) is deflected by the baroclinicity. The result is a more zonally aligned flow instead of a topographically controlled circulation as the one shown in Figure 2.10.*

$J(\chi, 1/H)$ term, which is usually referred to as the Joint Effect of Baroclinicity and Relief (JEBAR). Such a term describes the combination effect of the stratification and bottom topography, that establish a force which is able to deflect the depth-averaged flow from the geostrophic contours f/H (Mertz and G., 1992). By writing

$$J\left(\chi, \frac{f}{H}\right) = \frac{1}{H^2}\left(\frac{\partial \chi}{\partial y}\frac{\partial H}{\partial x} - \frac{\partial \chi}{\partial x}\frac{\partial H}{\partial y}\right),$$

it is possible to interpret the JEBAR effect: since for our configuration the density decreases northward, $\partial\chi/\partial y < 0$ at a fixed x. Considering a bottom slope along a zonal path, we have $\partial H/\partial x < 0$ left of the topographic maximum and $\partial H/\partial x > 0$ right of the topographic maximum, which means $J(\chi, 1/H) > 0$ upstream of the bottom anomaly and $J(\chi, 1/H) < 0$ downstream of the bottom anomaly. If we define α as the angle between the normal to the geostrophic contours and the depth-averaged velocity and take into account that $\nabla(f/H) \cdot \vec{U}$ is proportional to $cos\alpha$, we have

- $\nabla(f/H)\cdot\vec{U}=0 \;\Rightarrow\; \alpha=\pi/2$
  no stratification and/or no bottom slopes,
- $\nabla(f/H)\cdot\vec{U}>0 \;\Rightarrow\; 0<\alpha<\pi/2$
  left of the topographic maximum,
- $\nabla(f/H)\cdot\vec{U}<0 \;\Rightarrow\; -\pi/2<\alpha<0$
  right of the topographic maximum,

This yields a strengthening of the zonal character of the flow when it crosses a topography anomaly in a stratified ocean, as shown in Figure 2.14.

Chapter 3

Intrinsic variability of the Southern Ocean in an eddy-permitting model

3.1 Introduction

In this chapter the results of an eddy-permitting model for the Southern Ocean circulation will be presented, focusing on the role of the *nonlinear* effects in generating both *high and low-frequency intrinsic variability* of the flow.

The study of nonlinear effects is one of the central issues of *dynamical system theory*, which is an active branch of science with a very broad applicability spacing from classical and quantum mechanics to geosciences, from economy to biology, etc.. In particular, this field of science has seen a rapidly increasing interest starting from the discovery due to Lorenz (1963) about the possibility that (even simple) dynamical systems can yield extreme sensitivity to initial conditions (the so-called "chaos").

The behaviour of a nonlinear system and its features may be investigated through a series of analytical techniques (for a detailed description one can

refer to Strogatz, 1994; Nicolis, 1995; Dijkstra, 2005). By defining the *phase space* as the space in which all possible states of the system are represented by a point belonging to it, the time evolution can be described by:

- a *fixed point* (or steady state), when the system is in equilibrium;
- a closed periodic orbit;
- a quasi-periodic orbit;
- a chaotic orbit.

If, starting from a subspace of the phase space the orbit remains within it, that subspace is called *invariant manifold*. Fixed points, limit cycles and quasi-periodic orbits are particular cases of invariant manifolds. In general, an invariant manifold is defined *stable* if any sufficiently small parturbation in the initial conditions does not alter the qualitative behaviour of the system, i.e. an invariant manifold in a reference configuration remains an invariant manifold in any (slightly) perturbed configurations. On the other hand, chaotic attractors exist as well.

The qualitative features of the evolution of a given dynamical system can be changed (in particular, a stable invariant manifold can be created, destroyed, or changed) as a *control parameter* is varied. This change in the dynamics is called *bifurcation*, and the parameter value at which it occurs is called *bifurcation point*.

Figure 3.1 shows how, by varying the lateral friction coefficient A_H in our model for the Southern Ocean, it is possible to pass from a steady state solution (a fixed point) to a variable behaviour. As the imposed external forcing is steady, this represents an example of the generation of intrinsic variability (or also called *self-sustained oscillations*) associated with the oceanic system. Such a process is strictly linked with nonlinear effects. The first bifurcation from a fixed point leads to a *limit cycle*. By increasing the nonlinearity even further, the system yields a chaotic behaviour, which arises through a sequence of bifurcations involving higher order transitions. (Figure 3.1).

Thus, besides the variability induced by fluctuations of the external forcing, intrinsic variability can also arise due to nonlinear effects internal to the ocean system. In particular, oceanic intrinsic variability on interannual, interdecadal, and longer timescales (the *low-frequency* intrinsic variability) may

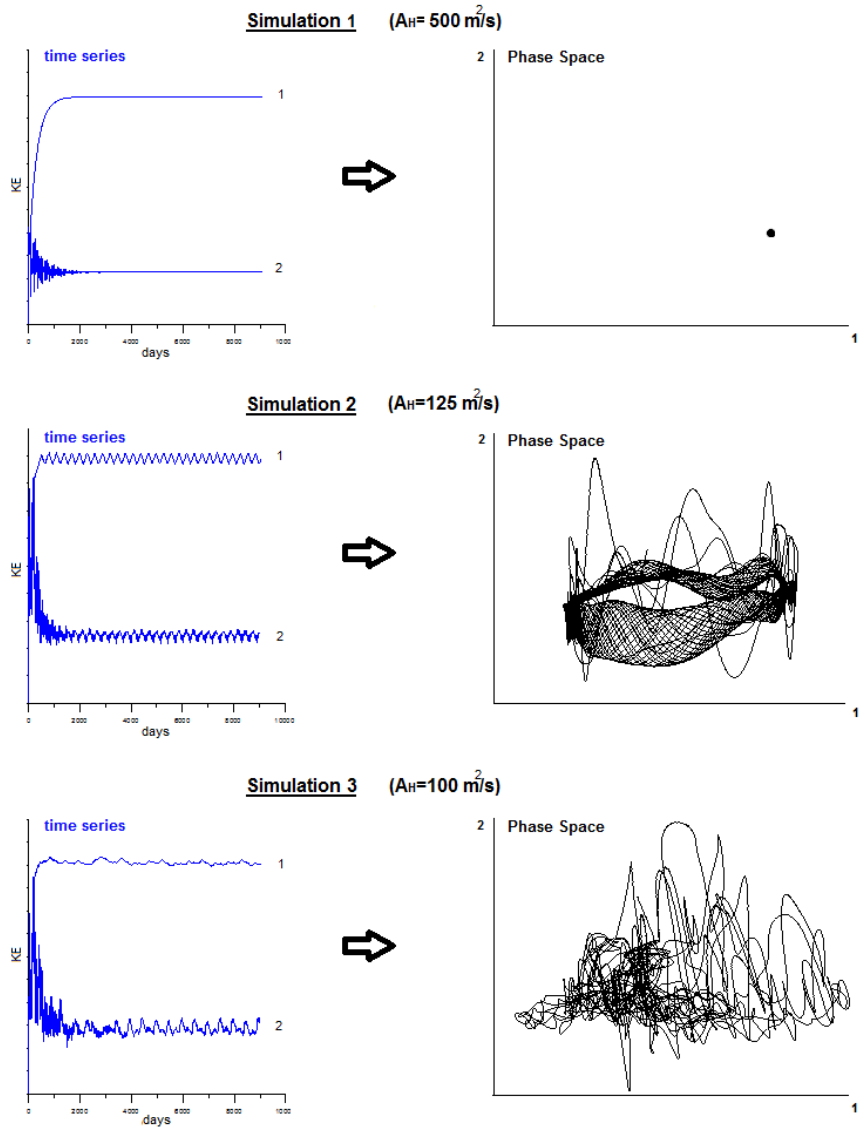

Figure 3.1: *Three different behaviours of a flat-bottom barotropic Southern Ocean obtained by decreasing A_H (emphasizing the nonlinearity). On the left-hand side, time series of the kinetic energy integrated over two different sectors is shown; on the right side, the associated orbits in phase space are plotted. In the first simulation, the system reaches a steady solution represented by fixed point in the phase space. Increasing the nonlinearity the system can produce self-sustained oscillations, which can even lead to chaotic behaviour.*

arise. A review of studies on the intrinsic variability in both the wind-driven and thermohaline ocean circulation, mainly at mid-latitude, can be found in Dijkstra (2005) and Dijkstra and Ghil (2005). In general, such model studies are based on either low-dimensional systems, (e.g. Jiang *et al.*, 1995; Simonnet and Dijkstra, 2002; Simonnet *et al.*, 2005; Pierini, 2011), or, more commonly, on primitive or quasigeostrophic (QG) equations, (e.g. Jiang *et al.*, 1995; McCalpin and Haidvogel, 1996; Spall, 1996; Hogg *et al.*, 2005; Pierini, 2006; Pierini *et al.*, 2009; Pierini and Dijkstra, 2009). As far as the Southern ocean is concerned, the interdecadal variability of the ACC was analyzed by Hogg and Blundell (2006) using a QG model.

In this chapter, by performing very long (more than 100 years) numerical simulations we will start analyzing the possibility of intrinsic variability for the Southern Ocean circulation: to this respect, regions where the intrinsic variability arises will be identified. A statistical analysis of these results will be presented in the following chapters.

3.2 Intrinsic variability in a QG model for the ACC

Our analysis of the self-sustaind oscillations in the Southern Ocean, is inspired to a previous model study of Hogg and Blundell (2006), who already evidenced how interactions between the mean flow and the eddy field associated with the ACC are likely to be the leading mechanism in the generation of internal variability within the Southern Ocean. The results of their 3-layer QG ACC channel model show, in fact, a zonal basic state of the flow which, due to baroclinic instability, gives rise to a strong eddy field. As a consequence, their simulations display a robust mode of intrinsic variability in the flow which, being dependent upon the explicit reproduction of the baroclinic eddies, is sensitive to several factors such as the parameterization of the lateral eddy viscosity (Figure 3.2), the stratification, the bottom stress and the wind stress (Figure 3.3).

The intrinsic variability may be explained as a feedback process between the potential energy supplied by the imposed steady wind stress, and the kinetic energy associated with the formation of eddies. From all the cases shown in Figure 3.2 and 3.3 it is clear that an increase in eddy kinetic energy is linked to a loss of potential energy. As the velocity of the current in

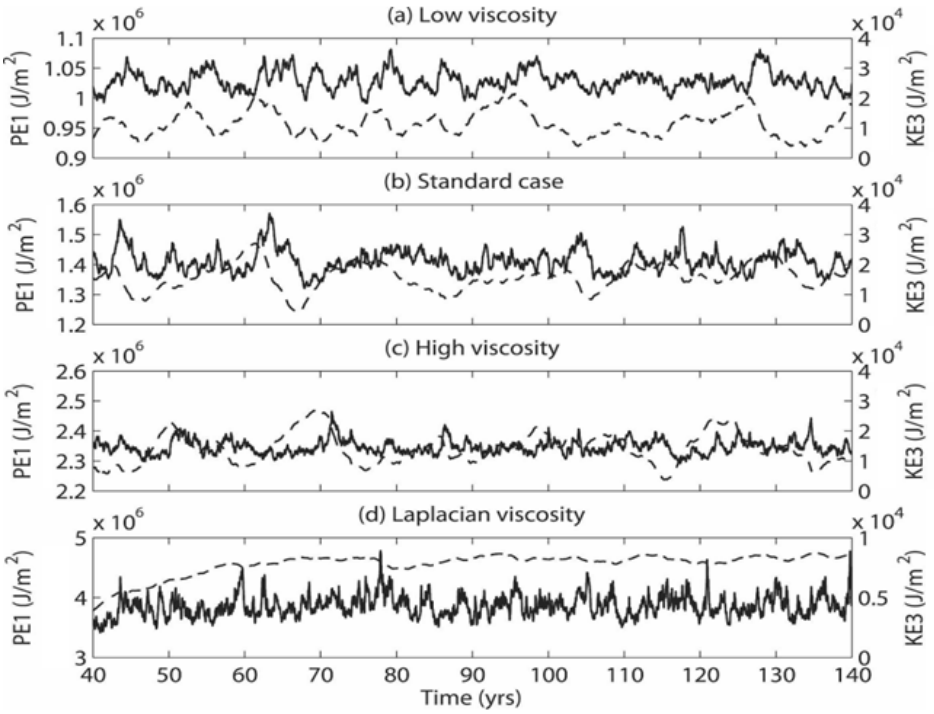

Figure 3.2: *Time series of upper-interface potential energy (dashed lines) and deep layer eddy kinetic energy (solid line) for a series of different simulations. The sensitivity to horizontal viscosity is evidenced by varying the horizontal eddy viscosity coefficient (biharmonic in the first three simulations, laplacian in the fourth simulation): a)* $A_H = 2 \cdot 10^9 m^4/s$, *b)* $A_H = 1 \cdot 10^{10} m^4/s$, *c)* $A_H = 1 \cdot 10^{11} m^4/s$, *d)* $A_H = 600 m^2/s$. *Picture from Hogg and Blundell (2006).*

the upper layer is fed by the wind forcing, the baroclinic instability process, which extracts energy from the mean flow into baroclinic eddies, may exceed a critical threshold. The latter exists because, as already explained in the chapter 2, eddy activity helps to transfer momentum into the lower layers. At the threshold, i.e. at the maximum of eddy kinetic energy, the deep flow allows topography to steer the current, weakening the zonal behaviour of the flow and enhancing baroclinic instability. This cycle is therefore subject to positive feedback, which amplifies the production of the eddies until the storage of available potential energy vanishes, allowing the system to return to its more zonal, lower energy state.

By adopting a similar domain as the one used by Hogg and Blundell

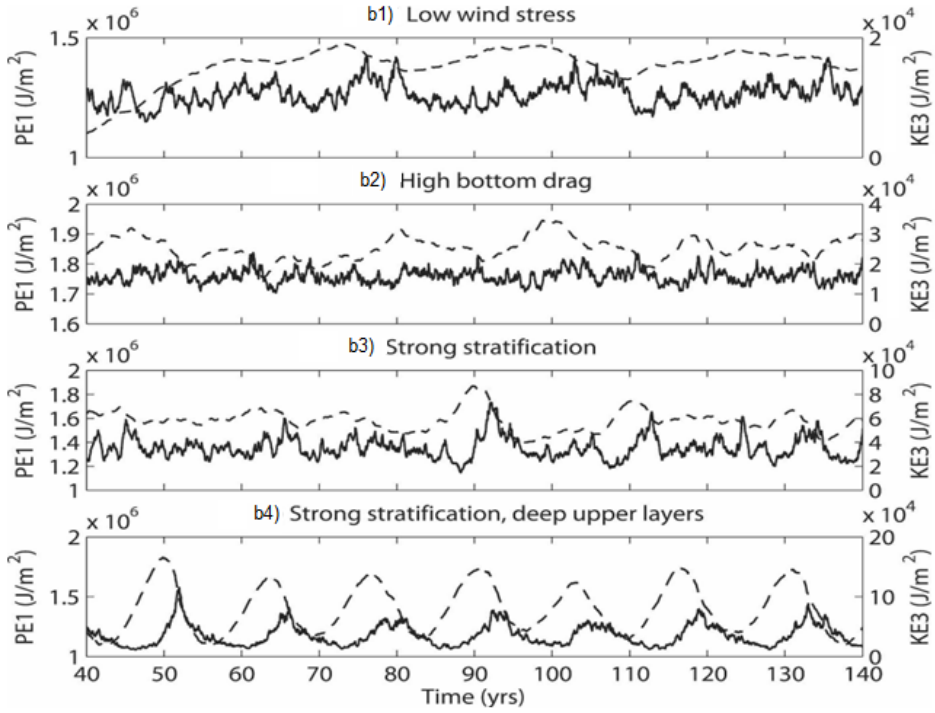

Figure 3.3: *Time series of upper-interface potential energy (dashed lines) and deep layer eddy kinetic energy (solid line) for a series of different simulations. The sensitivity to other physical parameters is evidenced with respect to the standard simulation b) in Figure 3.2 by varying the wind stress in b1), the bottom Ekman layer thickness in b2), the reduced gravity in b3) and the reduced gravity plus layer thickness in b4). Picture from Hogg and Blundell (2006).*

(2006) in their QG model, in the next section we will define an eddy-permitting primitive equations model for the Southern Ocean, which is a based on the baroclinic model already adopted in chapter 2.

3.3 A new model configuration

In Figure 2.12 a case of intrinsic variability within the ACC has already been evidenced for the baroclinic simulation presented in the previous chapter. In order to better analyze the intrinsic variability of the Southern Ocean system, a new model configuration has been implemented, in which the nonlinear behaviour is more efficiently modeled. To do this, a slightly

higher (eddy-permitting) spatial resolution has been adopted for the primitive equation channel model for a stratified Southern Ocean with realistic topography. As a consequence, the model is now able to resolve smaller scale features, since the spatial resolution is smaller than the *Baroclinic Rossby deformation radii*. This will allow us to include in the model the important effect of baroclinic instability, and the consequent eddy-mean flow interaction, although in a simplified framework.

3.3.1 Parameter values

First of all, the number of *sigma* levels has been increased to 12: this should enable us to achieve a better description of the flow-topography interaction, which is likely to be another central process in the generation of internal variability.

Table 3.1: *List of parameter values used in the new model configuration.*

Parameters	Value	Description
$[x_E, x_W]$	$[60°E, 180°E]$	zonal boundaries of the domain
$[y_N, y_S]$	$[32°S, 71°S]$	meridional boundaries of the domain
Δx	$1/3°$	spatial resolution in the y direction
Δy	$1/5°$	spatial resolution in the y direction
Δt_e	20 s	external time step
Δt_i	600 s	internal time step
k_σ	12	number of *sigma* levels
Hor	0.12	Horcon parameter

The higher spatial resolution, the associated shorter time step required to satisfy the CFL numerical stability condition, and the increased number of *sigma* levels make this model implementation much more expensive in terms of computational calculus. To reduce the CPU time needed for each simulation, the extension of the domain of integration has been therefore reduced: the domain still consists of a reentrant zonal channel with periodic boundary conditions, however the eastern edge is now located at 60 °E. This reduced domain does include, however, the Drake Passage region which is likely to be the most active area in terms of internal variability. The topogra-

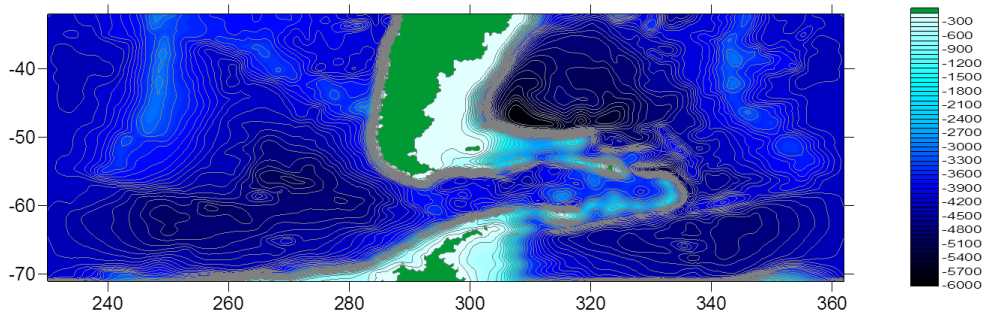

Figure 3.4: *The topography in the new configuration.*

phy has been obtained by interpolating, smoothing and projecting onto the model grid the $1/60^\circ$ GEBCO[1] data, with a linear transition region of 10° between the eastern and western boundaries, as shown in Figure 3.4.

Since the spatial resolution varies with latitude, the *Smagorinski formula* for the lateral viscosity coefficient

$$A_H = C_H \Delta x \Delta y \frac{1}{2} \left| \nabla \vec{u} + (\nabla \vec{u})^T \right|$$

has been used, representing a more suitable parameterization of the horizontal eddy viscosity (C_H is the so-called adimesional *Horcon constant*).

In order to unequivocally recognize the intrinsic origin of the variability the system has, again, been forced by a steady climatological wind stress (Figure 3.5) and, now, also by a steady idealized surface heat flux characterized by a vanishing net heat budget over the whole domain, as it already done for the baroclinic simulation in chapter 2.

3.3.2 Sensitivity experiments

The results obtained with three different simulations will be presented in this chapter. Simulation 1 is the reference simulation; in simulation 2 a weaker smoothing of the bottom topography has been considered while in simulation 3 the background stratification has been changed slightly, as shown in Figure 3.6.

[1]General Bathymetric Chart of the Oceans available at www.gebco.net

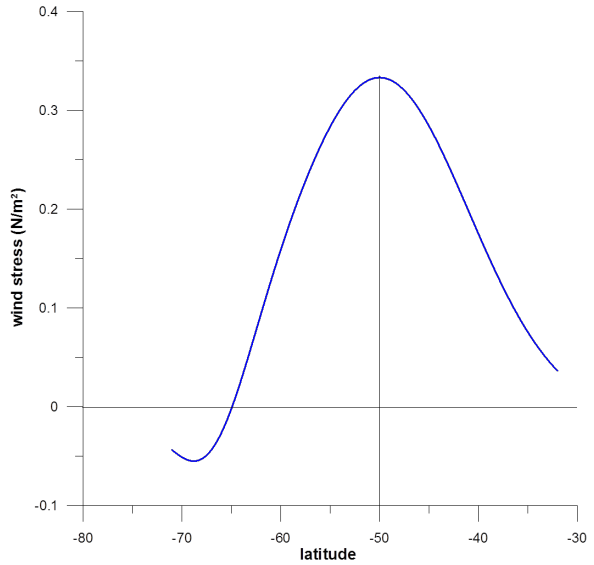

Figure 3.5: *Latitudinal profile of the steady climatological wind stress used in the numerical simulations.*

In chapter 5 the sensitivity of the model to the topography will be investigated, and two additional simulations will be analyzed. Table 3.2 summarizes all the numerical experiments presented for the eddy-permitting model.

Table 3.2: *Summary of the simulations performed with the eddy-permitting model.*

Simulation	Stratification	Topography	Chapter
1	type 1	smoothing 1	3,5
2	type 2	smoothing 2	3
3	type 2	smoothing 2	3
4	type 1	smoothing 3	5
5	type 1	smoothing 4	5

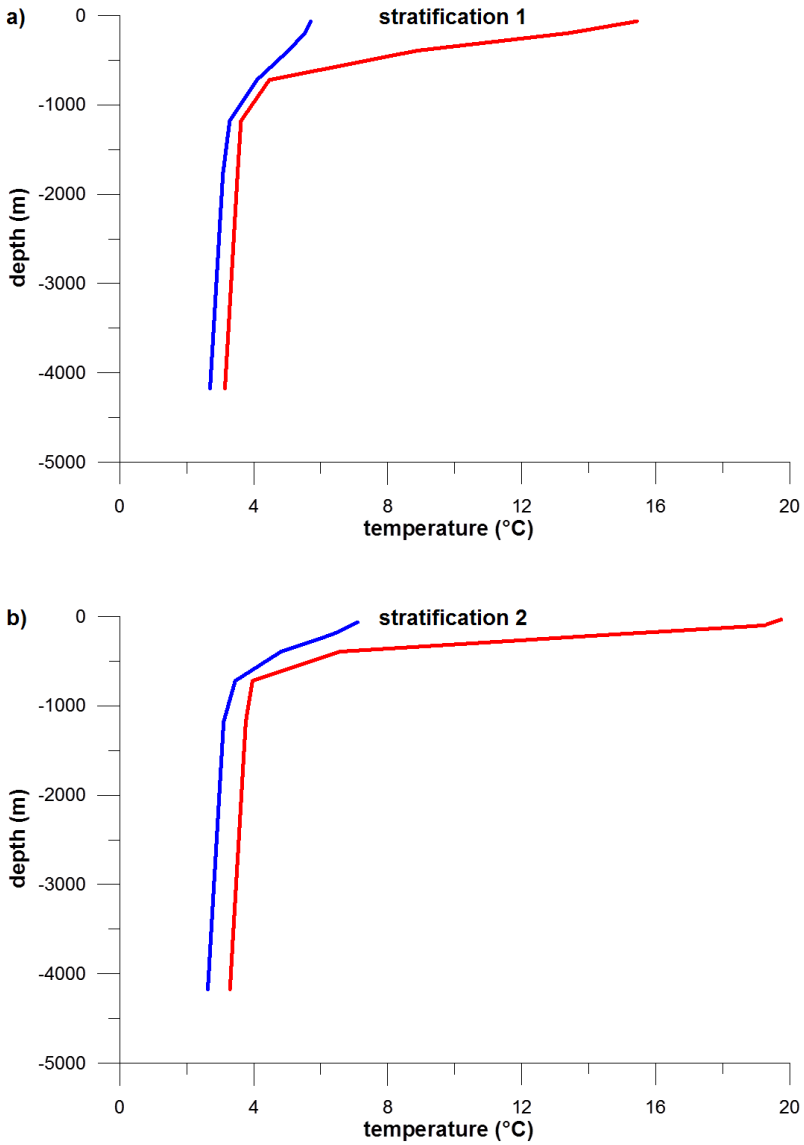

Figure 3.6: *Different background stratifications used in the numerical simulations: a) temperature profiles imposed in simulation 1; b) temperature profiles imposed in simulations 2 and 3. The red lines refer to the northernmost latitude of the domain (at 32 °S), whereas the blue lines refer to the southernmost latitude of the domain (at 71 °S).*

3.4 Results

In this chapter we limit ourselves to a qualitative description of our results, mainly focusing on the spatial pattern of the obtained intrinsic variability.

The higher spatial resolution, the increased number of *sigma* levels and the Smagorinski parameterization of the lateral eddy viscosity, all contribute to enhance the nonlinear character of the circulation. The resulting current system is more unstable with respect to the one reproduced in section 2.5.1, resulting in a high eddy activity associated with the mean zonal fronts of the ACC. The generation of standing and transient eddies has been found to be stronger where the main ACC flows across the most prominent topographic features. Figure 3.7 shows, for example, three different snapshots of the obtained depth averaged current in the region of the East-Pacific Rise, along with the associated high eddy activity. The role of transient eddies in both dynamical and water mass balances of the Southern Ocean circulation has been already stressed by Hallberg and Gnanadesikan (2006) through a series of increasingly high resolution primitive equation model simulations using the Hallberg Isopycnal Model (HIM).

The reproduced general circulation is consistent with observed data and other model results. Figure 3.8 shows our time averaged surface speed in comparison with that obtained by HIM with two different spatial resolutions. Moreover, Figure 3.9 evidences an overall good agreement when comparing a snapshot of the obtained *Sea Surface Temperature* (SST) with that measured by *Mercator Ocean System*.

In Figure 3.10 the 80−year-long time series of the total kinetic energy (KE) and of the net zonal transport across a meridional section are shown for each simulation. As the model starts from a state of rest, the imposed wind stress transfers kinetic energy into the system (and consequently potential energy by tilting the isopicnals), and the zonal flow intensifies. In general, while the transport reaches a quasi-steady state rather quickly (simulation 3), the total KE continues to increase for a longer time due to the baroclinic spin-up, reaching a quasi-steady equilibrium after about $20 - 30$ years. It should be stressed that, after spin up, the variability in each time series is generated and sustained by internal mechanisms, as the forcing is steady.

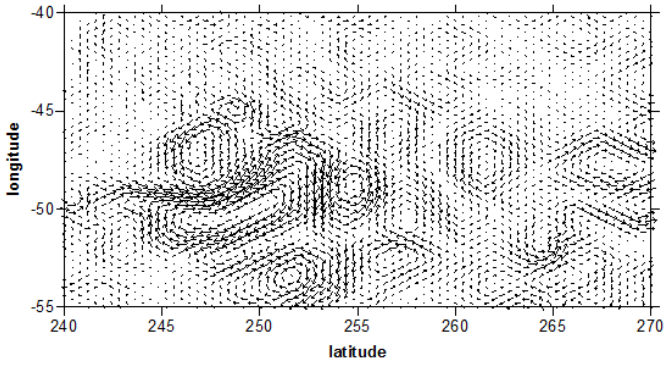

(a) $t = t_0$ *days*.

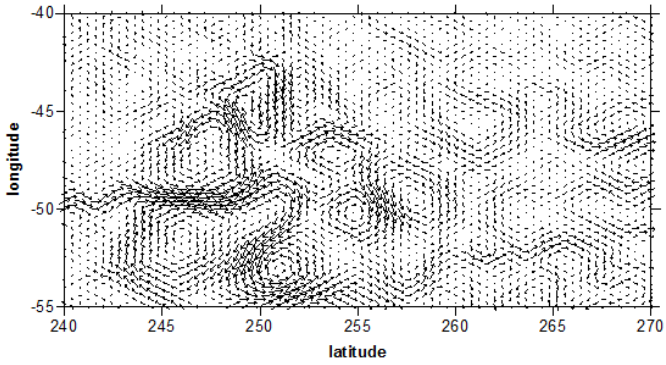

(b) $t = t_0 + 90$ *days*.

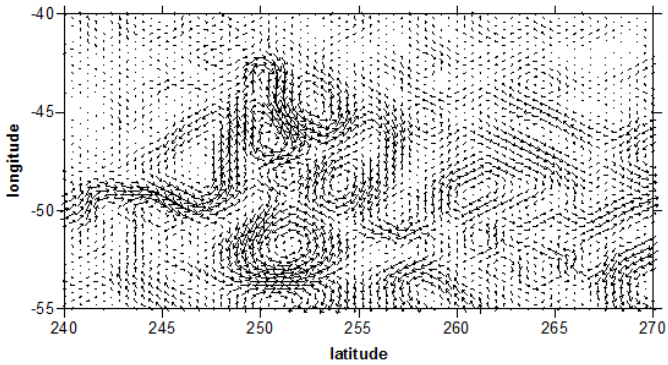

(c) $t = t_0 + 180$ *days*.

Figure 3.7: *Evolution of the depth averaged circulation in the region of the East Pacific Rise: the current field is shown at three different times.*

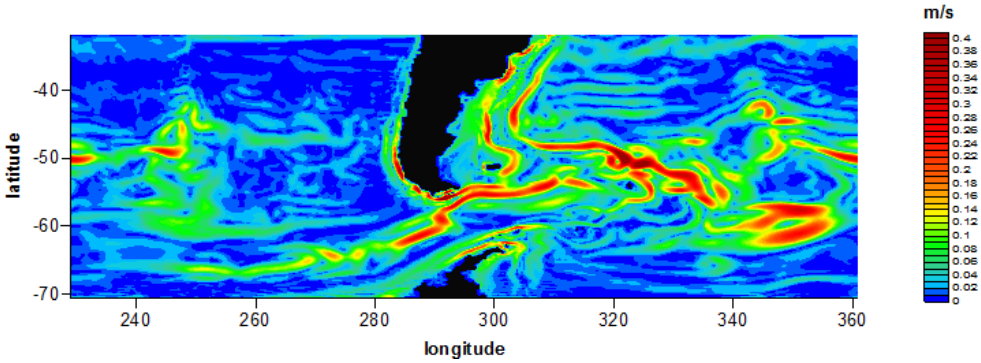

(a) *Resulting time averaged sea surface speed (simulation 1).*

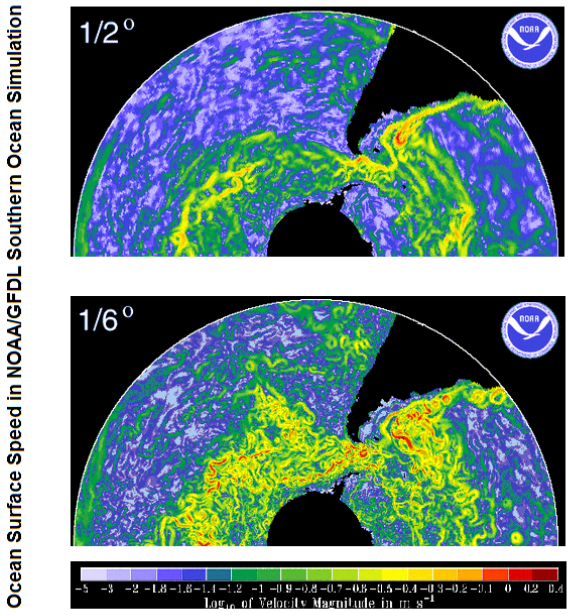

(b) *Sea surface speed from* $1/2^\circ$ *and* $1/6^\circ$ *spatial resolution from HIM..*

Figure 3.8: *Comparison between the general circulation pattern of the Southern Ocean found in our simulation 1 and in the HIM model results (from* `http://www.gfdl.noaa.gov`*).*

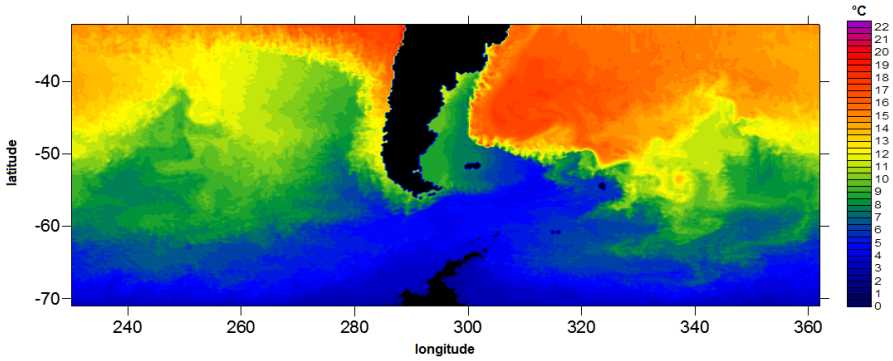

(a) *Simulated SST.*

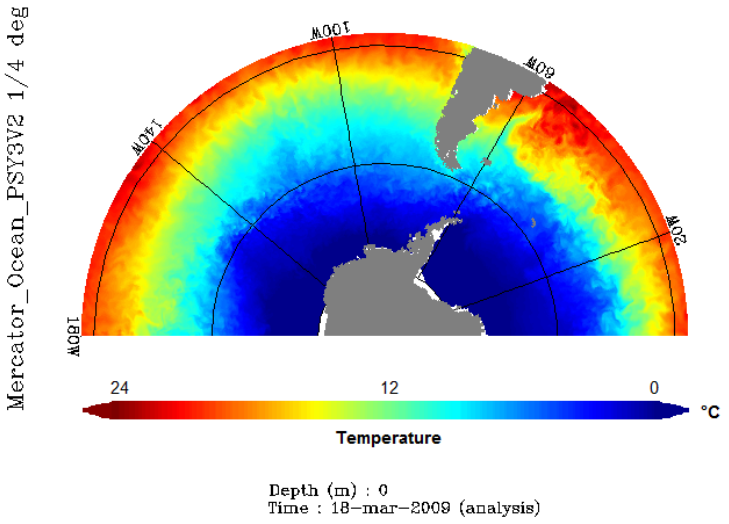

(b) *Measured SST.*

Figure 3.9: *Comparison between a snapshot of the simulated SST field and the* 18/03/2009 *Mercator Ocean measured SST (from* http://bulletin.mercator-ocean.fr*.)*

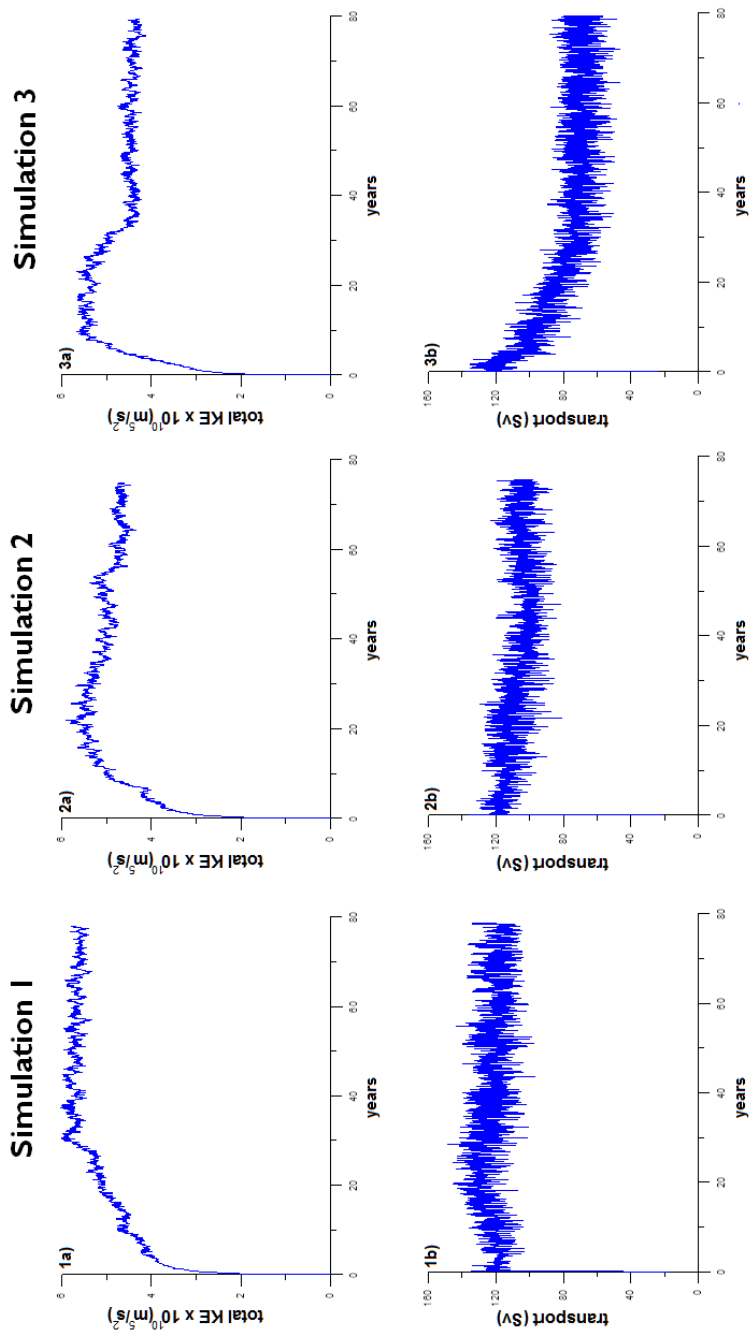

Figure 3.10: *Time-series of the total KE (upper panels) and of the volume transport (lower panels) across the Drake Passage for the 3 simulations. Data sampled every day.*

3.4.1 Spatial patterns of the intrinsic variability

Once the possibility of a significant intrinsic variability within the Southern Ocean is verified, its spatial structure should be investigated. In order to locate regions in which the variability is more prominent, the simulated SSH has been used. For each point of the domain, the SSH *variances* time-series have been calculated and plotted[2].

Figure 3.11 shows the field of variance computed over 100 days with data sampled every day. This is therefore indicative of the spatial pattern of the *high*-frequency intrinsic variability in the Southern Ocean. It is intriguing to note that most of the high-frequency variability is concentrated in the Argentine Basin all around the Zapiola Rise, where Fu (2007) found indeed local oscillations with a 25 day period by analyzing *TOPEX/Poseidon* SSH measurements. Such a high-frequency variability, as it will be discussed in more detail in the chapter 5, might be associated with a topographic Rossby normal mode oscillation.

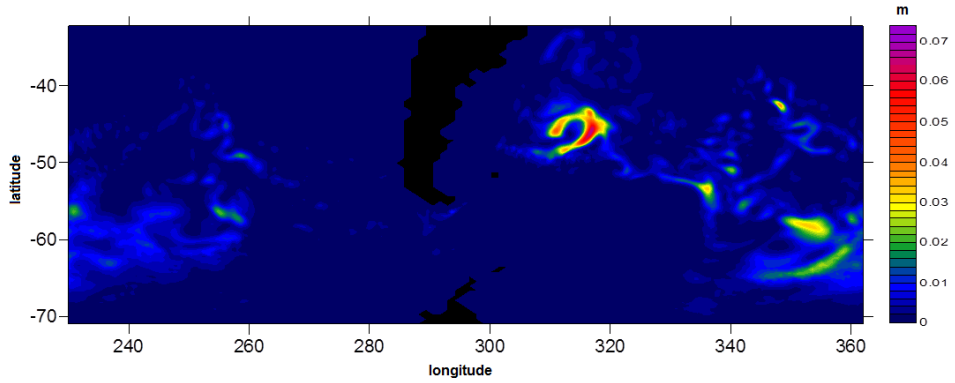

Figure 3.11: *Spatial structure of the high-frequency variability in the Southern Ocean obtained by plotting the variance of the 100-days SSH time-series. Data has been sampled with $T = 1$ day.*

On the other hand, the spatial pattern of the *low*-frequency variability can be detected by computing the variance over 40 years SSH time series with averaged data sampled every 3 months (Figure 3.12). It appears evident that, beyond the variability associated with the main bottom topographic

[2] Only the results of simulation 1 will be shown, the results of the other simulations being qualitative similar.

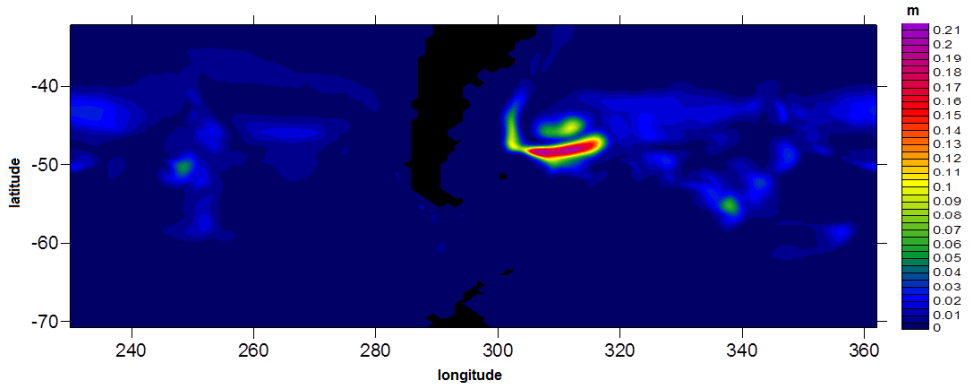

Figure 3.12: *Spatial structure of the low-frequency variability in the Southern Ocean obtained by plotting the variance of the 40-years SSH time-series computed over 3-months averaged data.*

features, e.g. the East-Pacific Rise, most of the low-frequency variability is again located in the Argentine Basin. The variance is particularly significant on the southern flank of the basin where the strong ACC, flowing eastward, is likely to contribute to such a behaviour. This striking result will constitute the basis for a more detailed analysis presented in the following chapters.

Chapter 4

Teleconnection mechanisms in the Southern Ocean

4.1 Introduction

The study of *complex networks* has recently received great attention in many fields of science, being largely inspired by the empirical analysis of real-world networks such as the *social network* or the *World Wide Web* in computer science. Ideas from network science have been applied to many areas, including sociology, mathematics, physics, biology, epidemiology, etc., yielding useful practical implications such as, for instance, the development of vaccination strategies for the control of diseases, the analysis of metabolic and genetic regulatory networks, the design of robust and scalable communication networks, both wired and wireless.

The application of complex network theory to oceanography and, more generally, to climate science, is an active area of scientific research, representing a powerful tool for a statistical analysis of interrelationships between different regions of the climate system, i.e. the so-called *teleconnections*. The aim of this chapter is to construct a teleconnection map for the Southern

Ocean, identifying regions within our domain that evidence statistical correlation with other limited regions. To do this, we assume each point of our domain to be a *node* or *vertex* of the oceanic network system and, by using the time series generated by the numerical simulations, we analyze the degree of correlation for each of the possible pair of nodes of the system. Defining a threshold for the degree of correlation, it is possible to define if two generic points of the system are directly connected (*neighbours*), depending on their degree of correlation.

The discussion is based on the idea of *small-world* system proposed by Watts and Strogatz (1998), in which most of the nodes are not directly connected to one another, but most of them can be "linked" to every other by a small number of topological steps. Specifically, a small-world network is defined as a network in which the typical topological distance L between two randomly chosen nodes (the number of steps required) grows proportionally to the logarithm of the number of nodes N in the network. In other words, a small-world network is characterized by the fact that it is not completely regular or completely random, but lies somewhere in between these two extremes. It is possible to argue that such a characterization is, in general, valid for a generic natural system, which, despite the apparent chaotic behaviour, shows self-organizing features.

4.2 Elements of complex network theory

Before analyzing the teleconnection mechanisms in the Southern Ocean, it is useful to give some introductory definitions of the classical network theory. For a deeper discussion one can refer to a specific textbook of network systems or, more generally, of *topology*, e.g. Diestel (2005), Kelley (1975).

4.2.1 The graph

According to the classical definition, a network or *graph* is an ordered pair $G = (V, E)$ characterized by a set $V = \{1, ..., N\}$ of *vertices* or *nodes* and by a set E of *edges*, or *lines* $\{i, j\}$, that are 2-element subsets of V, as they link couples of nodes.

A graph can be:

- *directed*, when the edges have an orientation, and $\{i,j\} \neq \{j,i\}$;
- *undirected*, when the edges have no orientation, and the generic edge $\{i,j\}$ is identical to the edge $\{j,i\}$;
- *simple*, when it has no loops and no more than one edge between any pair of vertices, where a *loop* is an edge (directed or undirected) which starts and ends on the same vertex;
- *multigraph*, when multiple edges and loops are allowed;
- *weighted*, when a number (weight) is assigned to each edge to represent, for example, costs, lengths or capacities, etc., depending on the problem at hand;
- *unweighted*, when the edges have no weight, or they have the same weight.

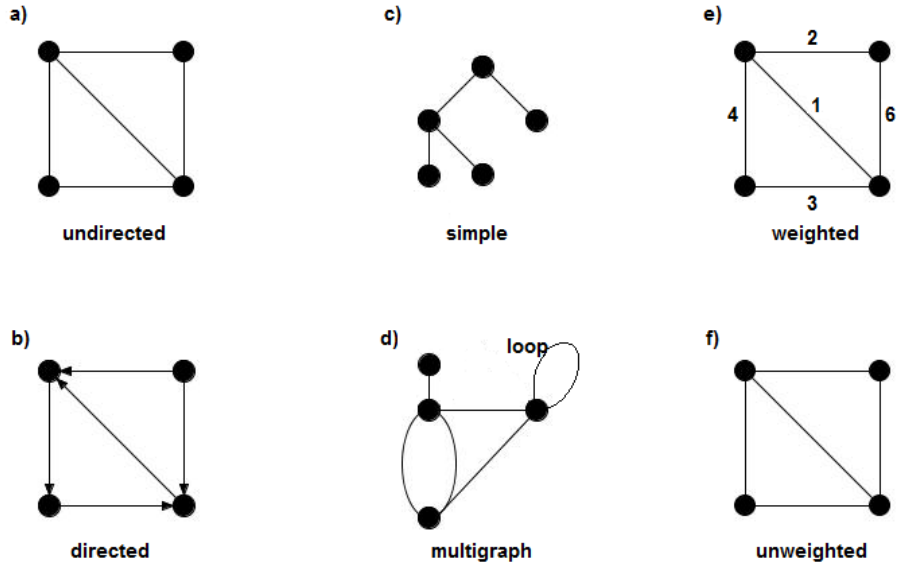

Figure 4.1: *Classification of graphs.*

For our purpose, we consider undirected and unweighted simple graphs, where therefore only one edge can exist between a pair of vertices, while self-loops of the type $\{i,i\}$ are not allowed.

4.2.2 The adjacency matrix

The undirected and unweighted simple graphs can be represented by the symmetric *adjacency matrix*, defined as

$$A_{i,j} = \begin{cases} 0 & \text{if } \{i,j\} \notin E \\ 1 & \text{if } \{i,j\} \in E, \end{cases} \tag{4.1}$$

indicating which nodes of the graph are adjacent to which other nodes. If a graph consists of N vertices, the symmetric $A_{i,j}$ matrix has NxN dimension and its elements represent all the possible combinations between a couple of nodes in the graph, which is 0 if the nodes are not linked and 1 if they are linked by an edge. Figure 4.2 shows an example of undirected and unweighted simple graphs, with the associated adjacency matrix.

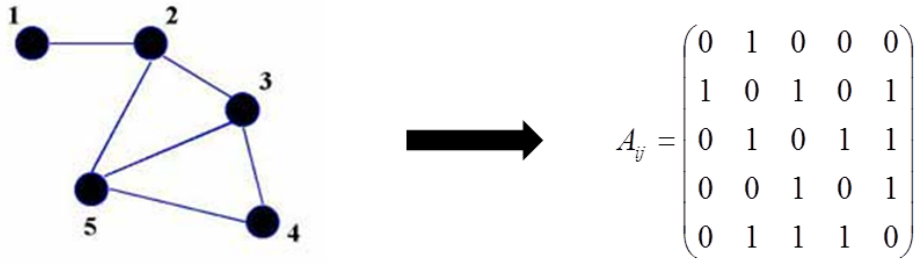

Figure 4.2: *Example of adjacency matrix of an undirected and unweighted simple graphs. Each element of the symmetric matrix corresponds to one of the possible pairs of nodes of the graph.*

4.2.3 Network measures

Within the graph analysis, there are several useful tools which can identify the features of the network under study. One of these is the measure of the *centrality* of the vertices within a graph, that determines the relative importance of a vertex (for example, how popular a person is within a social network, or, how important an airport is in the flight connections around the world). Among all the centrality measures, the *degree centrality* and *closeness centrality* have been selected for this study, which provide an insight into the network topology on the local and global scales, respectively.

Degree Centrality

The degree centrality k_v is a local measure that gives the number of first neighbours, i.e. the number of edges, of a vertex and can be calculated from the network adjacency matrix $A_{i,j}$, and is based on the parameter

$$k_v = \sum_{i=1}^{N} A_{vi}. \tag{4.2}$$

Referring to the graph in Figure 4.2, we have that, for example, the degree centrality for the point 4 is 2 and for the point 5 is 3.

Closeness Centrality

The closeness centrality CC_v is a global measure that gives the inverse of the averaged topological distance between a vertex v and all the other vertices in the network reachable from it. It is defined as

$$CC_v = \frac{N-1}{\sum_{i=1}^{N} d_{vi}}, \tag{4.3}$$

where d_{ij} is the topological distance or *shortest path*, that represents the minimum number of edges that must be crossed to reach a vertex j from the vertex i. The shortest path can be calculated by the so-called *Dijkstra algorithm* (Dijkstra, 1959). The closeness centrality, therefore, ranges between 0 and 1 and is larger when v is topologically close to the rest of the network. Referring to the graph in Figure 4.2, we have that, for example, the closeness centrality for the point 1 is 0.3077 and for the point 3 is $0,8$.

4.3 Construction of the network system

To construct a network system for the Southern Ocean we essentially follow the method adopted by Donges *et al.* (2009). The vertices of our network coincide with the grid points of our spatial domain. Starting from the time series of SSH and SST generated by the model at each grid point, edges are added between pairs of vertices depending on the degree of statistical interdependence between the corresponding pairs of anomaly time series.

4.3.1 Correlation measures

We thus need a *correlation measure* C_{ij} that can be, for example, the *Pearson correlation*, which estimates the strength of the linear relationship between two *random variables* $v_i(t)$ and $v_j(t)$, or the *mutual information*, which is a nonlinear measure of the mutual dependence between two time series $v_i(t)$ and $v_j(t)$.

Pearson correlation

The most familiar measure of dependence between two random variables is the Pearson correlation, obtained by dividing the *covariance* of the two variables by the product of their *standard deviations*. Indicating with the overline the *mean* of a quantity and with $\mu = \overline{v}$ the *expected value* of a time series, the covariance between two generic time series v_i and v_j is defined as

$$\mathrm{cov}(v_i, v_j) = \overline{(v_i - \mu_i)\left(v_j - \mu_j\right)} = \overline{(v_i X_j)} - \mu_i \mu_j,$$

while the standard deviation of the time series is given by

$$\sigma_v = \sqrt{\overline{(v_t - \mu)^2}}.$$

The Pearson correlation is, hence, a coefficient whose value can range from -1 to 1, and is defined by

$$R_{ij} = \frac{\mathrm{cov}\left(v_i(t), v_j(t)\right)}{\sigma_{v_i(t)} \sigma_{v_j(t)}} = R_{ji}\,. \tag{4.4}$$

Mutual Information

The mutual information of two random variables is a quantity that measures the mutual dependence of the two variables. It is able to detect nonlinear relationships between two time series, and can be interpreted as the excess of information generated by assuming two time series to be indepen-

dent, and is able to detect nonlinear relationships. It is defined as

$$M_{i,j} = \sum_{a \in v_i} \sum_{b \in v_j} p(a,b) log \frac{p(a,b)}{p(a)p(b)}, \tag{4.5}$$

where $p(a)$ and $p(b)$ are the probability density functions (PDF) of the time series v_i and v_j, respectively, and $p(a,b)$ is the joint probability density functions of v_i and v_j. The standard unit of measure of mutual information is the bit, when base 2 logarithms are used.

4.3.2 Teleconnection maps

For the definition of our network, the Pearson correlation[1] has been computed between time series of all the possible couples of points of the domain, in so quantifying the statistical interdependence between each point. In particular, we have considered the absolute value of the Pearson correlation $C_{ij} = \left|R_{ij}\right|$, since large negative and positive values are both indicative of a strong linear statistical interdependence.

We have used values of SSH and SST generated by the model for the simulation 1, moreover we have considered a 50 years signal for these parameters, starting from $t_0 = 20$ yr of the simulation, so that the spinup phase is not included. Each sample of the time series is a value averaged over 3 months since we are more interested in teleconnection mechanisms on interannual time scale. Each vertex is therefore associated to a 200 value-time series. We have furthermore normalized the time series by the unit variance.

Once a threshold for the degree of correlation is chosen, we have added an edge between all the pairs of nodes which exhibit a correlation higher than such a threshold. In this way it is possible to identify all the neighbours of generic node and to determine the adjacency matrix. The teleconnection maps are eventually produced by using one of the network measures introduced in section 4.2.3. Figure 4.3 schematizes all the steps followed in constructing the network to obtain a teleconnection map. These maps show regions within the domain which are particularly interrelated with the rest

[1] results using the mutual information as the correlation measure will not be shown in this preliminary analysis

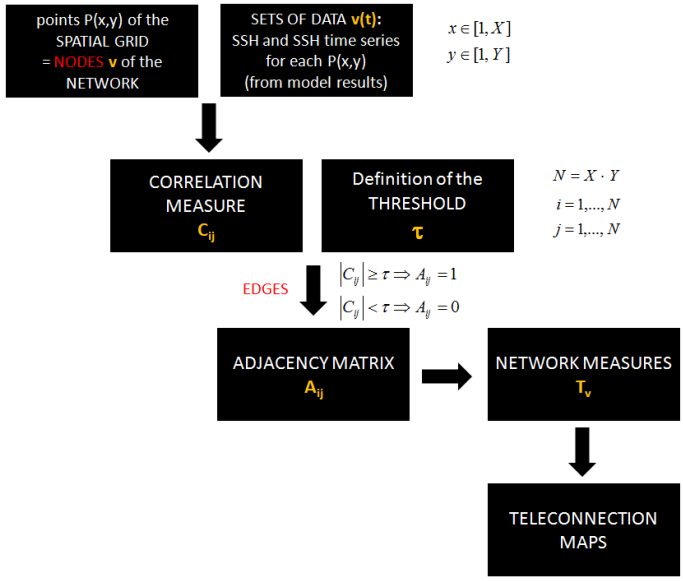

Figure 4.3: *The construction of the network for the Southern Ocean starting from data sets generated by the model.*

of the network, localizing limited areas that could be of significant importance in determining processes in other parts of the domain.

4.4 Teleconnectivity in the Southern Ocean

Figure 4.4 shows the teloconnection maps for the SSH both obtained by using the degree centrality and the closeness centrality as a network measure. Correspondingly, Figure 4.5 shows the teleconnection maps for the SST. Each of the teleconnection maps shows bounded regions which are interrelated to some degree with the rest of the network system, and, in contrast, regions whose behaviour is more independent. However, an interpretation of such a result is not unique. In evaluating these fields, in fact, one can just suppose that processes occurring in regions characterized by a significant centrality could effectively influence, in broad terms, the general behaviour of the system. This could imply that anomalies in a well teleconnected region of the domain could induce anomalies that will affect the behaviour elsewhere, and *vice versa*, but nothing more can be inferred about

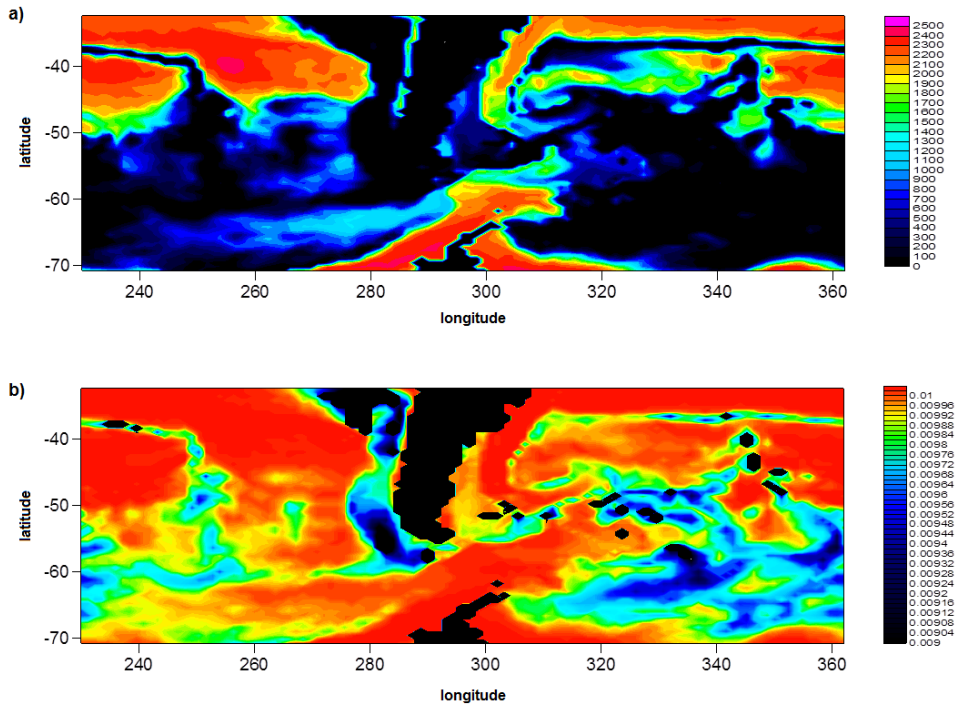

Figure 4.4: *Teleconnection in the Southern Ocean starting from the SSH data set produced the numerical model (simulation 1). a) Degree centrality. b) Closeness Centrality*

the exact location where such anomalies can occur.

4.4.1 The influence of the intrinsic variability in the network system

In order to better understand the teleconnection mechanisms in the Southern Ocean, it is possible to associate them with the intrinsic variability evidenced in chapter 3. In general, two signals that are constant or slightly variable have a high degree of correlation. Starting from such a consideration, it is interesting to investigate if there are regions within the Southern Ocean which show a significant internal variability and, at the same time, which also evidence an high degree of correlation with the rest of network system. This allows one to assess the importance of the intrinsic variability

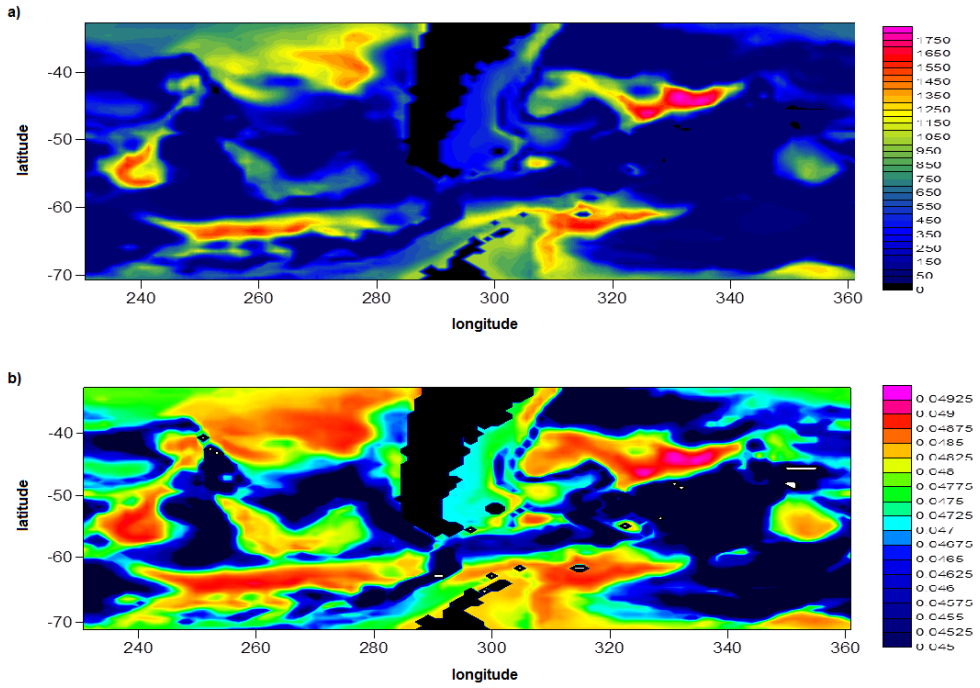

Figure 4.5: *Teleconnection in the Southern Ocean starting from the SST data set produced the numerical model (simulation 1). a) Degree centrality field. b) Closeness centrality*

on the general circulation at the domain scale. To do this, a new parameter has been introduced, the *weighted anomaly* W_v, which values the degree of influence of the variability evidenced within the system. By normalizing the random variable as follows

$$\langle v(t) \rangle = \frac{v(t)}{\max|v(t)|} ,$$

we have defined the weighted anomaly as

$$W_v = \left\langle \sigma_v^2 \right\rangle \langle T_v \rangle \ , \tag{4.6}$$

where σ_v^2 is the variance of the time series in a node, and T_v the corresponding network measure, i.e. the degree centrality or closeness centrality.

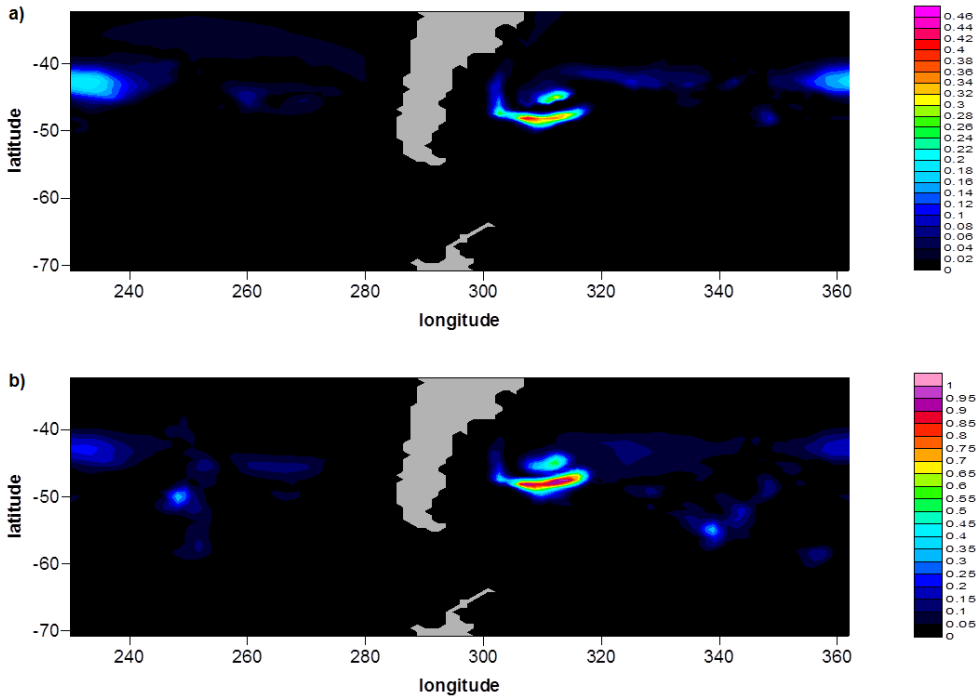

Figure 4.6: *Weighted influence of the intrinsic variability in the Southern Ocean system obtained from SSH time series. a) Degree centrality. b) Closeness Centrality*

Figure 4.6 shows the *weighted anomaly* for the SSH using both the degree centrality and closeness centrality. The main, striking feature is that, again, we can identify the Argentine Basin as the most active region of teleconnection. This allows us to argue that the variability in the Argentine Basin has the greatest impact in terms of general dynamics.

This result is not trivial, as it may well happen that a region characterized by a strong intrinsic variability is not a well teleconnected region. This is not the case of the Argentine Basin, that is therefore likely to influence the behaviour of the circulation at a much larger scale.

Such an analysis has stimulated us to proceed studying in detail the mechanisms of intrinsic variability occurring in the Argentine Basin. This is the subject of the next chapter.

Chapter 5

Different regimes in the Argentine Basin

5.1 Introduction

Encouraged by the results of the analysis of the spatial patterns of the intrinsic variability within the Southern Ocean (chapter 3), and by the considerations made about the teleconnection mechanisms (chapter 4), here we focus on the interpretation of the results of the simulations with reference to a specific area: the Argentine Basin (AB).

The AB is a very distinctive oceanic region located in the south-western Atlantic Ocean near the South American coast. This area is characterized by a deep bottom (with depth exceeding locally 6000 m) that is bounded by a very steep continental slope. A sedimentary deposit is located in the middle of the basin, the so-called Zapiola Rise (ZR), on top of which, at around (45°S, 45°W), the ocean bottom is about 1000 m higher than the abyssal plain.

From the dynamical point of view, the AB is a crucial region where different water masses encounter and mix, and where the circulation is likely to

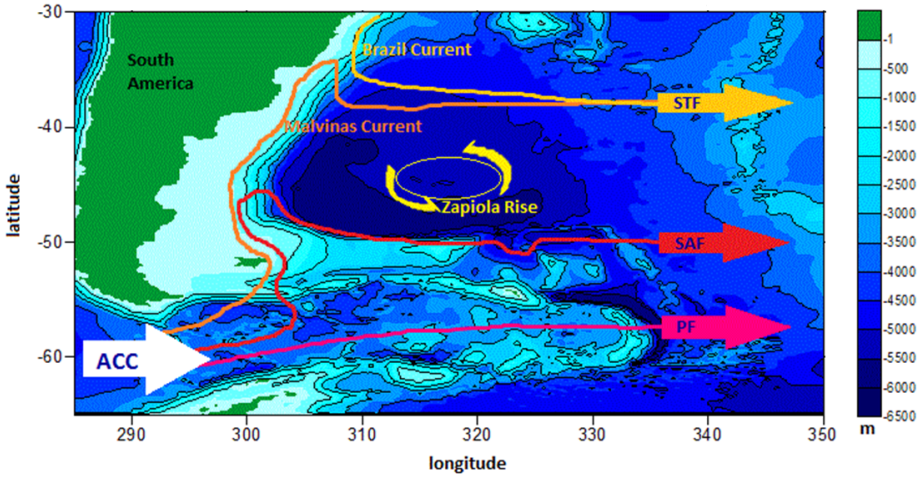

Figure 5.1: *Sketch of the circulation in the south-western Atlantic. The ACC dominates the southern part of the basin with its strong transport of 130-140 Sv, splitting into two major fronts, the PF and the SAF. Part of this water turns north forming the western boundary Malvinas Current with estimated transport of 60-80 Sv. From the north, the Brazil Current flows southward along the continental shelf carrying about 20 Sv, and joins with the Malvinas Current at around 39°S creating the very energetic and turbulent region known as the Confluence Zone or Brazil/Malvinas Confluence (BMC).*

affect the meridional water exchanges between the Southern Ocean and the subtropical region, with an associated strong impact on the global climate system. Figure 5.1 shows the pattern of the mean circulation in the south-western Atlantic. At Drake Passage the strong Antarctic Circumpolar Current (ACC) flows, from the Pacific Ocean, into the Atlantic, where it splits into three major fronts, the Polar Front (PF, that crosses the Scotia Sea), the Sub Antarctic Front (SAF, that follows the Falkland Plateau and turns eastward in proximity of the southern part of the AB), and the Malvinas Current (a western boundary current supported by the continental slope along the South American coasts). The latter, carrying relatively cold water and flowing equatorwards, encounters a warmer western boundary current flowing from the north, the Brazil Current, generating one of the most turbulent and energetic regions in the ocean, the Confluence Zone (CZ) at around 39°S. Such a convergence area yields a strong zonal flow, the Sub Tropical Front (STF), that is considered the northern limit of the Southern Ocean. In addition, just between the SAF and the STF, an intense barotropic anticyclonic

circulation trapped above the ZR has been recently discovered (Saunders and King, 1995): the Zapiola Anticyclone (ZA), with an estimated transport of about 80-100 Sv. The resulting circulation pattern is hence strongly influenced by the bottom topography, and the ZA is probably able to enhance meridional water masses exchanges.

There are several evidences of the variability in the AB over a wide range of time scales. Analyzing SSH observations from satellite altimeter data, (Fu *et al.*, 2001; Tai and Fu, 2005) found a counterclockwise rotating barotropic wave around the ZR with a period close to 25-days, that they interpreted as a barotropic topographic Rossby wave associated with the geometry of the basin. This is usually denoted as Rossby wave "mode" (Pedlosky, 1987; Pierini, 1996; Weijer *et al.*, 2007a), as it may be seen as the solution of an eigenvalue problem. A statistical analysis of altimeter data supported by an idealized model study suggest that the 25-day periodicity could result from the superposition of more than one barotropic basin mode (Weijer *et al.*, 2007a,b). Hughes *et al.* (2007) examined bottom pressure records in the AB and found three forms of high-frequency variability, confirming the existence of a dominant mode at around 20-25 days. Figure 5.2 shows such a high-frequency variability.

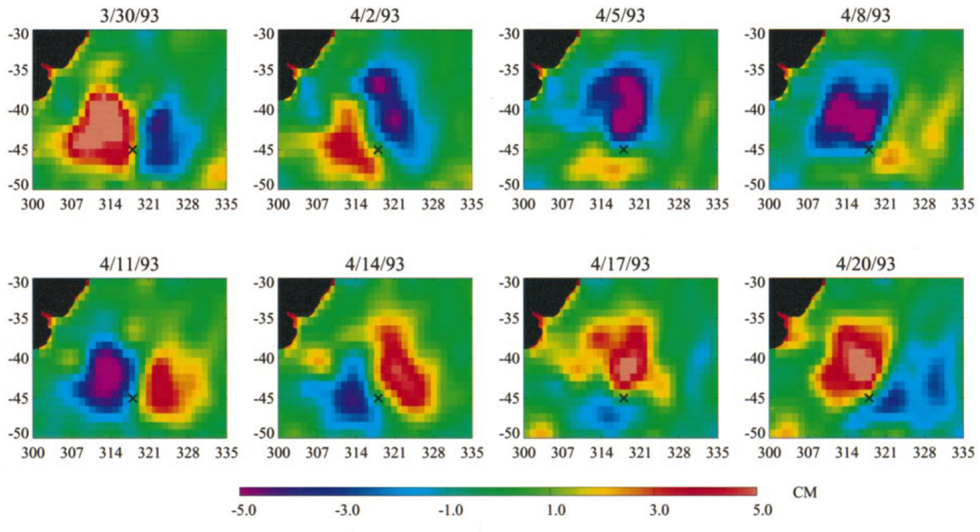

Figure 5.2: *High-pass filtered SSH anomaly sampled every 3 days between 3/30/1993 and 04/20/1993 obtained from TOPEX/Poseidon measurements. From Fu et al. (2001)*

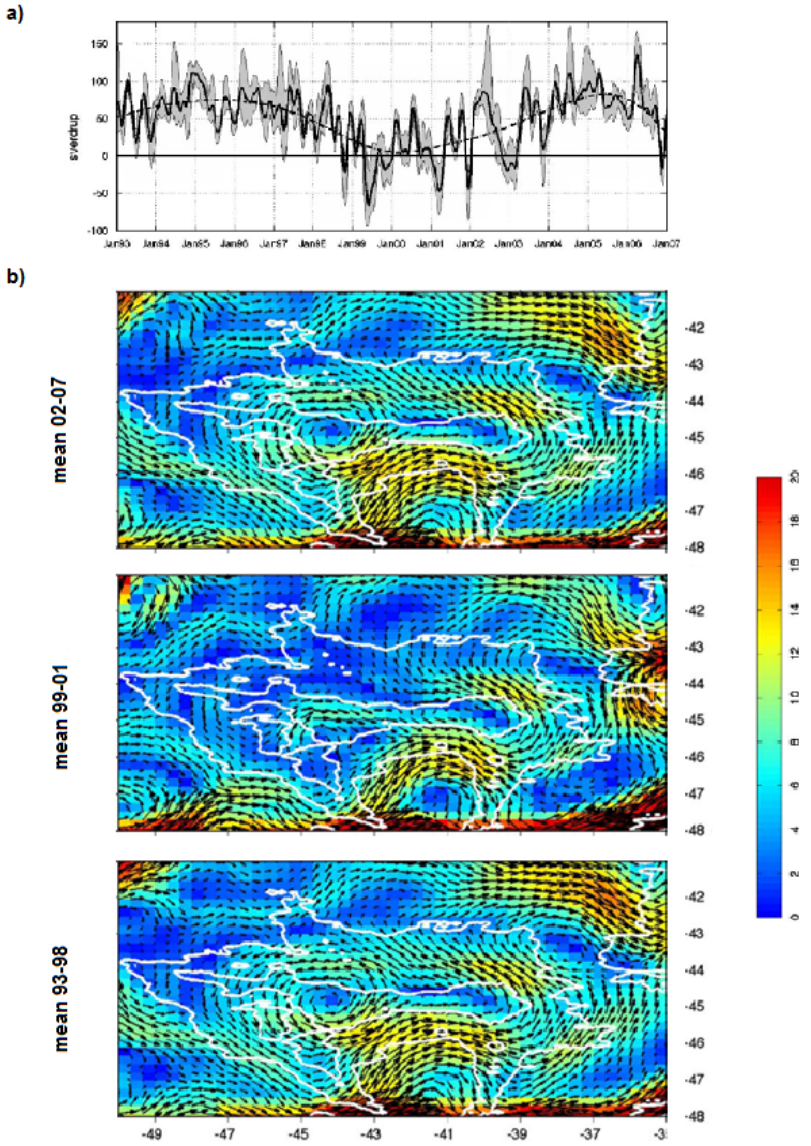

Figure 5.3: *(a) Low-frequency variability in the transport time series of the ZA associated with acceleration and deceleration of the main flow: this variability is likely to be intrinsically generated. Indications for a possible collapse of the ZA for a limited time (1999-2001) are also evidenced (b). From Saraceno et al. (2009).*

A significant interannual variability of the ZA is also evident from satellite altimetry observations, and recent model results have suggested a theo-

retical interpretation. Saraceno *et al.* (2009) documented for the first time a clear low-frequency variability of the transport associated with the acceleration or deceleration of the main anticyclonic flow; indications for a possible collapse of the ZA also emerged for a limited time (Figure 5.3). Volkov and

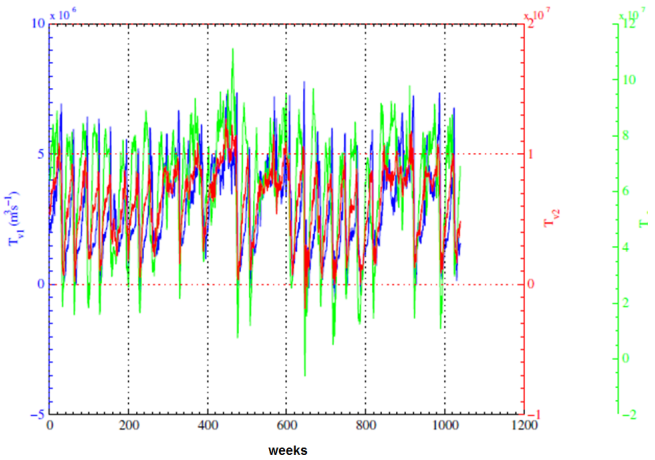

Figure 5.4: *Transport oscillations with a period of 6-7 yr that is set by basin mode perturbations. The time series evidences occasionally an irregular behavior: some stable periods appear, in which the transport remains high for a relatively long time. From Bigorre and Dewar (2009).*

Fu (2008) found that the interaction between the flow and the bottom topography are the dominant factors that determine the interannual variability of the ZA, yielding vorticity fluxes mainly advected from the southern part of the basin, where the SAF is located, and from the Confluence Zone. In an idealized model study, (Bigorre and Dewar, 2009) focused on the variability of the circulation around a large scale topographic anomaly, i.e. a seamount, in one case very similar to the ZR. They showed that the transport around the topographic feature is affected by a low-frequency variability that may be the direct response to the variability of the eddy field. They also found an almost periodic modulation set by the basin mode perturbation. However, this 6-7 years period was not always regular (Figure 5.4), and they could isolate a stability regime occurring when the gyre intensity was too intense to allow background perturbations to be significant; in contrast, when the strength of the topographic circulation decreased, perturbations became important and were able to shed the anticyclone away, leading in some cases

to a collapse of the counterclockwise flow around the seamount.

The current lack of long time series in the AB makes numerical simulations a fundamental tool to analyze the dynamics in the AB. Despite efforts in this sense, numerical models have only rarely proved able to reproduce all the main dynamical phenomena occurring in this region. By using a sigma-coordinate primitive equation model, de Miranda *et al.* (1999) performed the first realistic simulation of the ZA: they reproduced (with good agreement with observations) both the features of the strong recirculation flow over the ZR, and the distribution of the eddy kinetic energy, that is mostly concentrated near the Confluence Zone. They also extended the theory suggested by Dewar (1998), who provided the first theoretical interpretation of the existence of the ZA using an idealized QG model, evidencing that the strong anticyclonic flow over the main topographic feature was driven by eddies and controlled by bottom friction. Sensitivity experiments performed both with QG and primitive equations models showed that, by damping out the effects of eddies via increasing the lateral friction, the anticyclone over the topographic bump vanishes, thus evidencing that the eddy field is indeed responsible for exciting and maintaining it.

The Parallel Ocean Program (POP) model, a z-coordinate primitive equation model, is also able to reasonably reproduce the ZA; however the associated ZA transport (20 Sv) is considerably weaker than the 100 Sv transport suggested by measured data. According to de Miranda *et al.* (1999), the quantitative difference with POP results, has to be accounted for the type of vertical coordinates adopted: in the z-coordinate models, the flow at lower levels above the bottom topography interacts with vertical walls rather than with the sloping bottom; hence, lateral friction is likely to be the dominant dissipative mechanism in a z-coordinate model, the bottom friction being generally weakly significant. On the other hand, in sigma-coordinate models, since sidewall boundary layers can occur only near the coastlines, the values of later friction near the bottom cannot in general account for bottom friction. For this reason the sigma-coordinate system is considered the best when dealing with very complex bathymetries and/or in capturing the dynamical effects induced by the bottom topography.

In this chapter our purpose is to carry out a dynamical investigation of the internal variability in the Argentine Basin. Supported by the recent

discovery of the long-term variability of the ZA (Saraceno *et al.*, 2009), our analysis can be seen as an extension of the work of (Bigorre and Dewar, 2009); here we use a sigma-coordinate Primitive Equation Model instead of the QG model, and a realistic topography instead of a rectangular basin with a seamount. Far from willing to represent all the phenomena occurring in the South Atlantic, we develop a process study (a steady forcing is used) with essential elements of realism (a sophisticated ocean model and a realistic bottom topography and stratification are used), focusing mostly on the analysis of the intrinsic low-frequency variability. We conjecture that the nature of this variability is linked to the variability of the northern branch of the ACC, i.e. the SAF, which, through the southern limit of AB, is able to control the circulation around the ZR. Variations of the strength of the SAF affect the circulation within the AB, inducing accelerations and decelerations of the ZA. In particular, a significant deceleration can allow the flow to be more sensitive to topographic perturbations, yielding variations in the eddy field. This supports the recent work of Bigorre and Dewar (2009), who argued that the nature of the long-term variability of the ZA is tightly related to the eddy field activity. Good agreement can also be found with the analysis performed by Saraceno *et al.* (2009), who found a high correlation between ZA transport time-series and EKE time-series in points located near the position of SAF.

5.2 Analysis of the results

We start by analyzing in more detail the results of the reference simulation and of simulations 2 and 3 already presented in chapter 3 (see Table 3.2).

The main circulation simulated in the reference case is, as already shown in Figure 3.8 and Figure 3.9, an acceptable representation of the real circulation in the eastern South Pacific/western South Atlantic part of the Southern Ocean: the main frontal behaviour of the ACC is well reproduced, as well as the strong recirculation pattern within the AB. Values of the transport across the Drake Passage are in good agreement with the generally accepted estimate of 130 Sv. Since the domain is limited by the northern boundary at 32°S, such a model is unable to reproduce the CZ, since a double-gyre wind

stress forcing would be needed, along with a more extended domain. This is a drawback of our study, since the CZ has been shown to be, together with the SAF, the main source of eddy activity in the AB. On the other hand, our implementation can also be seen as an interesting diagnostic tool, since we isolate the contribution of the southern branch of the ZA in producing intrinsic variability: in other terms, we focus mainly on the effect of a variable SAF within the AB.

By analyzing the time series of the transport across the Drake Passage and the total kinetic energy Figure 3.10, the presence of an intrinsic variability is evident. It has already been shown that both the low-frequency (Figure 3.12) and high-frequency (Figure 3.11) variability of the SSH are more prominent in the region of the AB. For the (more energetic) long-term variability, there is a net band of maximum variability that roughly coincides with the position of the SAF. On the other hand, for the high-frequency variability, the highest oscillations occur around the ZR, indicating a significant wave propagation around the topographic feature.

5.2.1 Long-term variability of the Zapiola Anticyclone: two different regimes

For a deeper analysis of the low-frequency variability in the AB, we have chosen a point P located in the area of maximum variance (at around 47 °S, 45 °E) and we have analyzed the relative SSH and SST time series produced by the three simulations. Signals of both SSH and SST evidence a very clear behaviour of the AB circulation structure common to the three simulations: the existence of two completely different regimes. In the reference case, after a first period (30 yr) of relatively low variable character, the evolution of the SSH and SST in point P switches abruptly to a more variable regime. This might, at first sight, be explained in terms of the spinup phase, but the analysis of the other simulations clarifies that this is not the case. The other time series show, in fact, an opposite behaviour, with an initially very variable signal which suddenly becomes less variable (Figure 5.5). In order to stress the bimodal behaviour of the ZA flow, in Figure 5.7 the *Probability Density Function* (PDF) relative to SSH and SST signals of Figure 5.5 for the reference simulation are shown. It is therefore possible to distinguish between two distinct flow regimes in the AB connected by rapid switches.

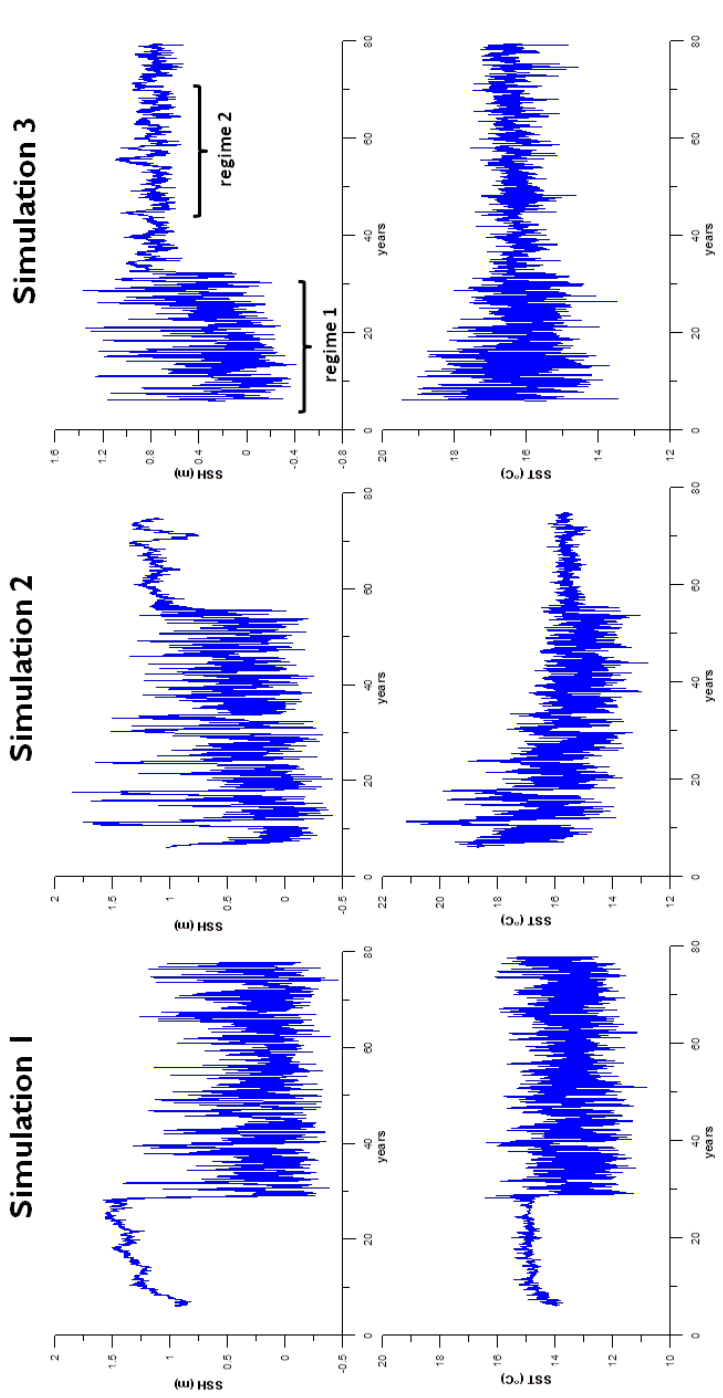

Figure 5.5: *Time-series of the SSH (upper panels) and SST (lower panels) in the point P located at 47 °S, 45 °E, for the 3 simulations. Data sampled every day.*

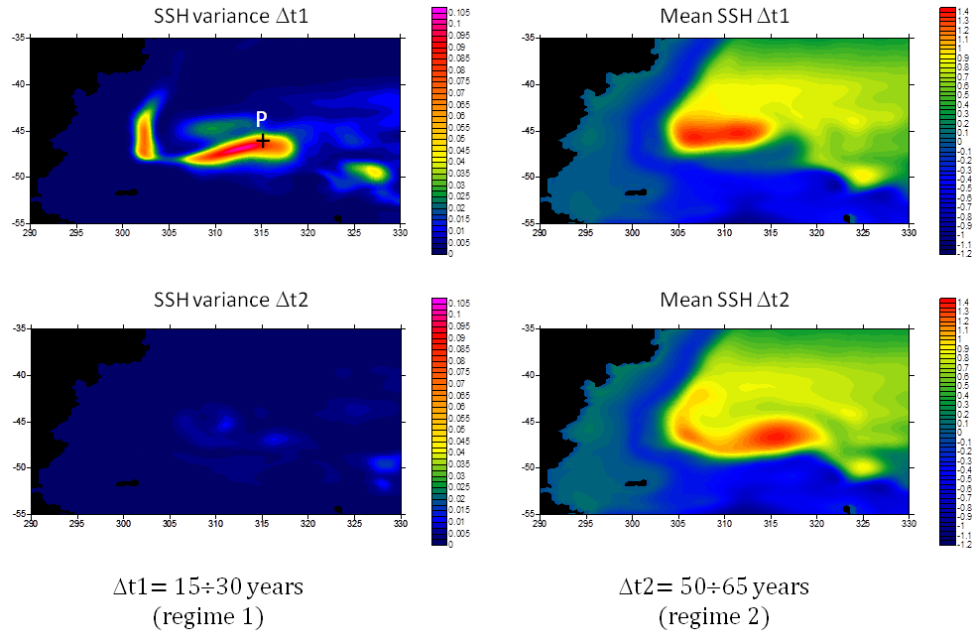

Figure 5.6: *SSH variance and SSH mean fields for the two different regimes resulting from simulation 3.*

What is also striking is the difference in variance between the two different flow regimes, as shown in the Figure 5.6. We will discuss in the section 5.4 how such a switch is sensitive to the bottom topography.

5.2.2 Short-term variability of the Zapiola Anticyclone: wave propagation around the topographic anomaly

As it was already shown in Figure 5.2, altimeter data evidence a 25-day rotating dipole wave around the ZR whose spatial scale is about 1000 km. The spatial and temporal characteristics of the wave can be explained by the solution of a linearized barotropic vorticity equation. The observed wave appears indeed to be a normal mode associated with the local geostrophic contours f/H (Fu *et al.*, 2001).

Our model is also able to qualitative reproduce such oscillations around the ZR as it it shown in the Figure 5.8. The results clearly evidence a wave which rotates counterclockwise around the ZR (located at 45 °S, 45 °E).

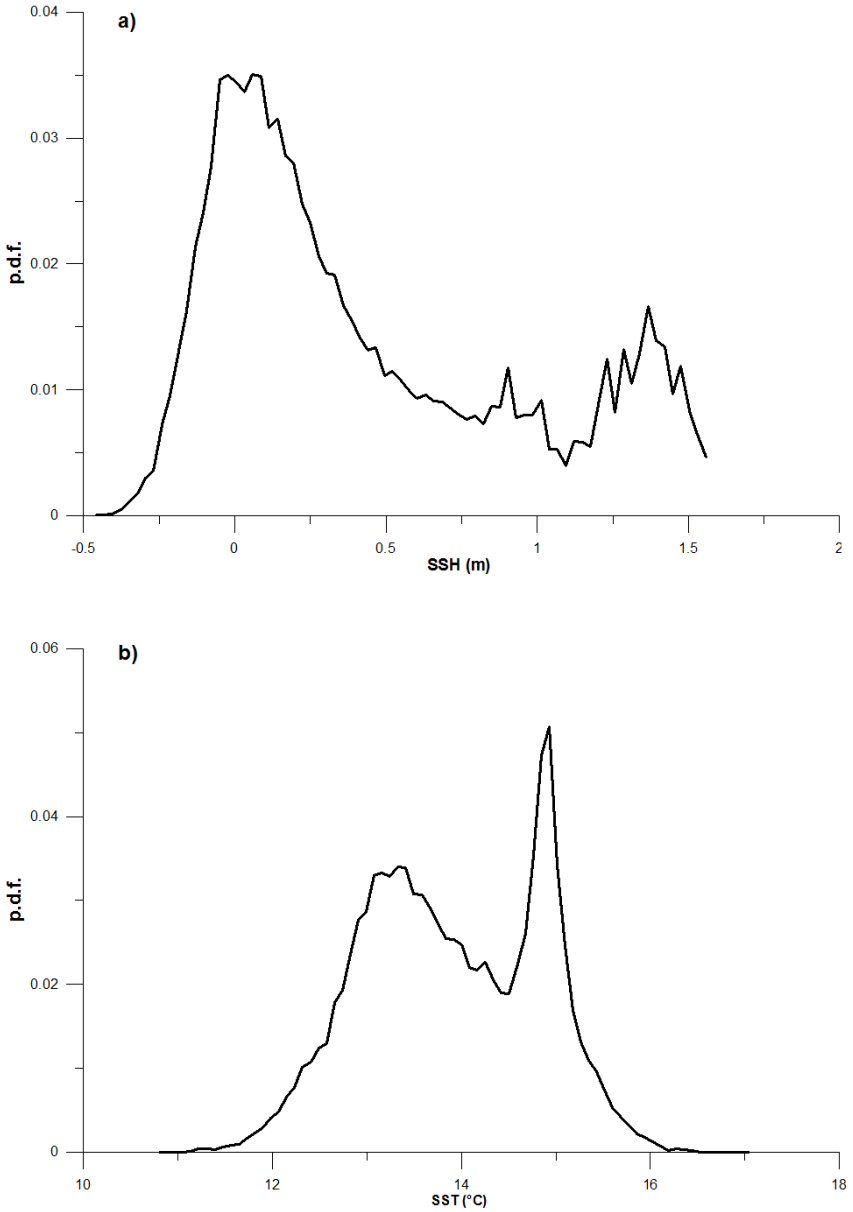

Figure 5.7: *Probability density function of the SSH (a) and of the SST (b) time series for the point P located at 47 °S, 45 °E, for the reference simulation.*

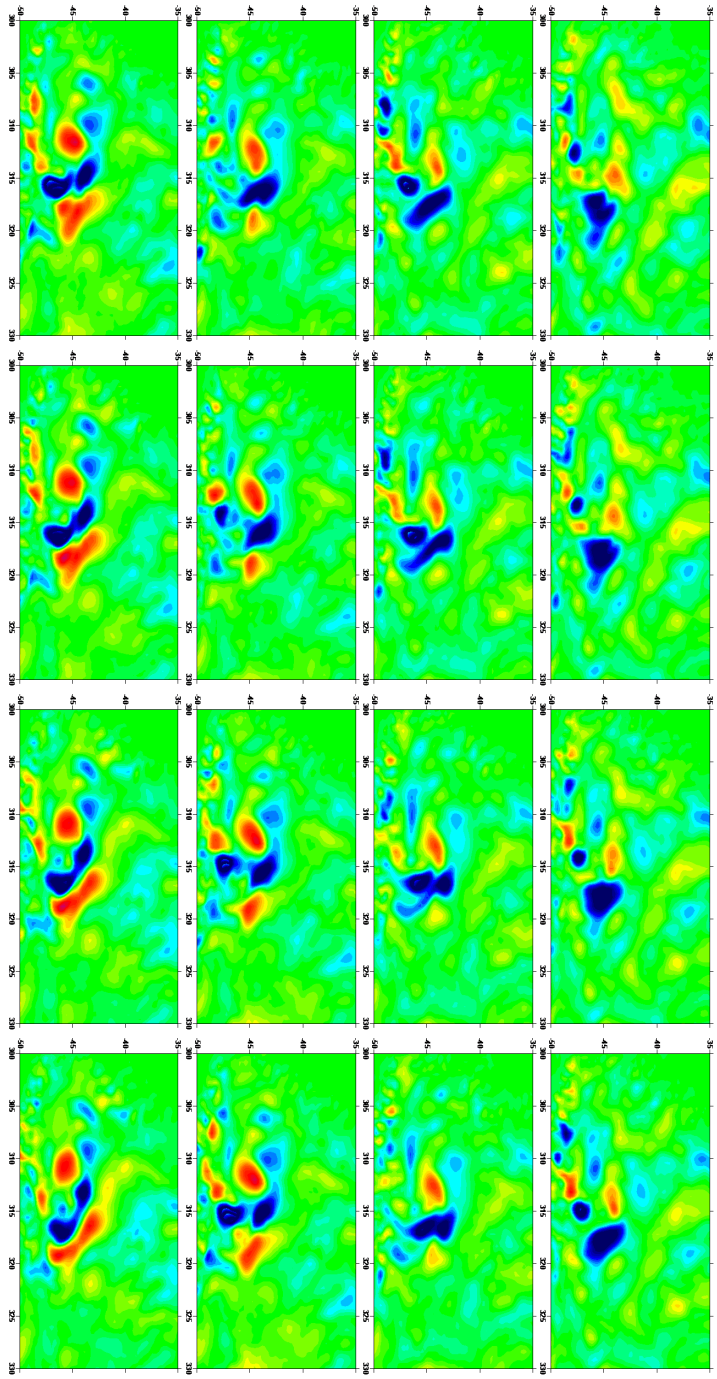

Figure 5.8: *Anomaly fields of the SSH obtained from the numerical simulations over 36 day.*

However, such a simulated oscillation yields energetic peaks around $T = 50$ days (Figure 5.9). Since this wave is likely to be a normal mode of the

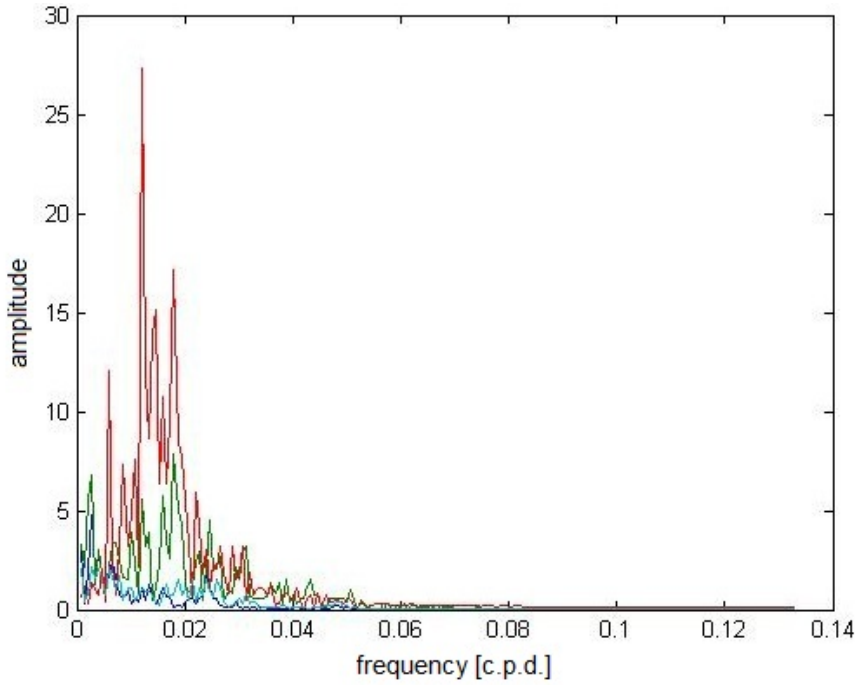

Figure 5.9: *Frequency spectrum for the SSH anomalies associated with 4 points around the Zapiola Rise. The spectrum is obtained from 1 yr-time series, with data sampled each day.*

basin controlled by the local topographic beta-effect, such a discrepancy in frequency is probably due to the (necessary) smoothing of the topography. Nevertheless, on the basis of this result it can be conjectured that the intrinsic low-frequency variability in the AB can potentially be one of the processes triggering a high frequency mode of variability within the basin.

5.3 A numerical issue concerning the *sigma*-coordinate system

The choice of the POM is mainly due to its sigma-coordinate system, which is a necessary feature when dealing with significant topographic variations such as those present in the AB (where the ZA is strongly influenced

by the bottom features) and, more in general, in the Southern Ocean. The quantitatively good results in reproducing a realistic ZA obtained in a recent model study of similar nature (de Miranda *et al.*, 1999) has, in fact, been attributed to the particular choice of the sigma-coordinate system. Together with the turbulence sub-model, the bottom-following vertical coordinate system allows the model to produce a realistic bottom boundary layer, which is likely to play a central role in controlling the anticyclonic circulation in the AB (Dewar, 1998).

Altought the sigma-coordinate system is probably the best approach in treating with complex topography, it represents, at the same time, a big constraint. The determination of the bathymetry is, in fact, the most delicate matter in implementing such a kind of model. If the bottom topography is particularly steep - this is the case of the AB - the discrete form of the pressure gradient terms can produce large systematic errors in the calculation, the so-called PG error (Messinger, 1982). The reason for this is that in σ-coordinates, the horizontal density gradient is the difference between two large terms:

$$\frac{\partial \rho}{\partial x}\Big|_z = \frac{\partial \rho}{\partial x} - \frac{\sigma}{H}\frac{\partial H}{\partial x}\frac{\partial \rho}{\partial \sigma}\,. \tag{5.1}$$

This may cause large truncation errors in the estimate of the local pressure, as well as hydrostatic inconsistency.

A reduction of the PG errors to acceptable values can be achieved by properly smoothing the bathymetry according to a criterion involving the bottom slope, and the resolution of the horizontal and vertical grids. This procedure represents therefore a crucial issue in implementing a sigma-coordinate model: if from one hand the smoothing method should reduce the computational errors just mentioned, on the other hand it is important to retain as much as possible the main features of the topography, in order to reproduce consistently the interactions between the flow and the oceanic bottom.

This problem was already handled with success by Barnier *et al.* (1998), Marchesiello *et al.* (1998) and de Miranda *et al.* (1999) in setting up a consistent model for the South Atlantic circulation. They proposed a criterion for the smoothing which has to satisfy certain conditions for each point (i, j) of the grid model. Defining the local parameter $r_h(i, j)$ as the maximum rel-

ative variation of the depth H over a grid element, local PG errors can be limited if

$$r_h(i,j) = \frac{\Delta_{x,y} h}{\overline{h}^{x,y}} = \\ = \frac{\max[\,|H(i+1,j) - H(i,j)|, |H(i,j+1) - H(i,j)|\,]}{\frac{1}{2}\min[\,H(i+1,j) + H(i,j),\, H(i,j+1) + H(i,j)\,]} < c\,, \quad (5.2)$$

where c is a constant usually taken as 0.2.

Furthermore, in order to avoid hydrostatic inconsistency, which is strictly linked with the vertical integration scheme, another condition for the smoothing should be respected. It is based on the argument that a numerical scheme becomes consistent if the maximum relative increase in bottom topography is less than the distance between two consecutive sigma levels. Thus, the bottom topography, already smoothed until the condition 5.2 is satisfied, should be smoothed again until the following criterion is respected everywhere in the model for every vertical level k:

$$\left| \frac{\Delta_{x,y} h\ \sigma(k-1) - 1}{\overline{h}^{x,y} \sigma(k+1) - \sigma(k-1)} \right| < 1\,. \quad (5.3)$$

To understand the magnitude of the PG errors using a *sigma*-coordinate model, in Figure 5.10 we show the results of two different numerical experiments for a stratified Southern Ocean: in the first one an unsmoothed topography has been adopted, while in the second one a smoothing criterion for the topography which satisfies equations 5.2 5.3 has been applied. Starting from rest and without any external forcing, both simulations evidence behaviours due to the PG errors. However, a significant difference between these two experiment is clearly evident: when the coarse topography is used, the PG increases with time, leading inevitably to spurious results, whereas using an suitably smoothed topography, the PG error can be limited within neglecting values, not influencing the final result.

The results just obtained stimulate a more thorough analysis of the sensitivity of the results to the choice of topography which is strictly related to the smoothing method adopted.

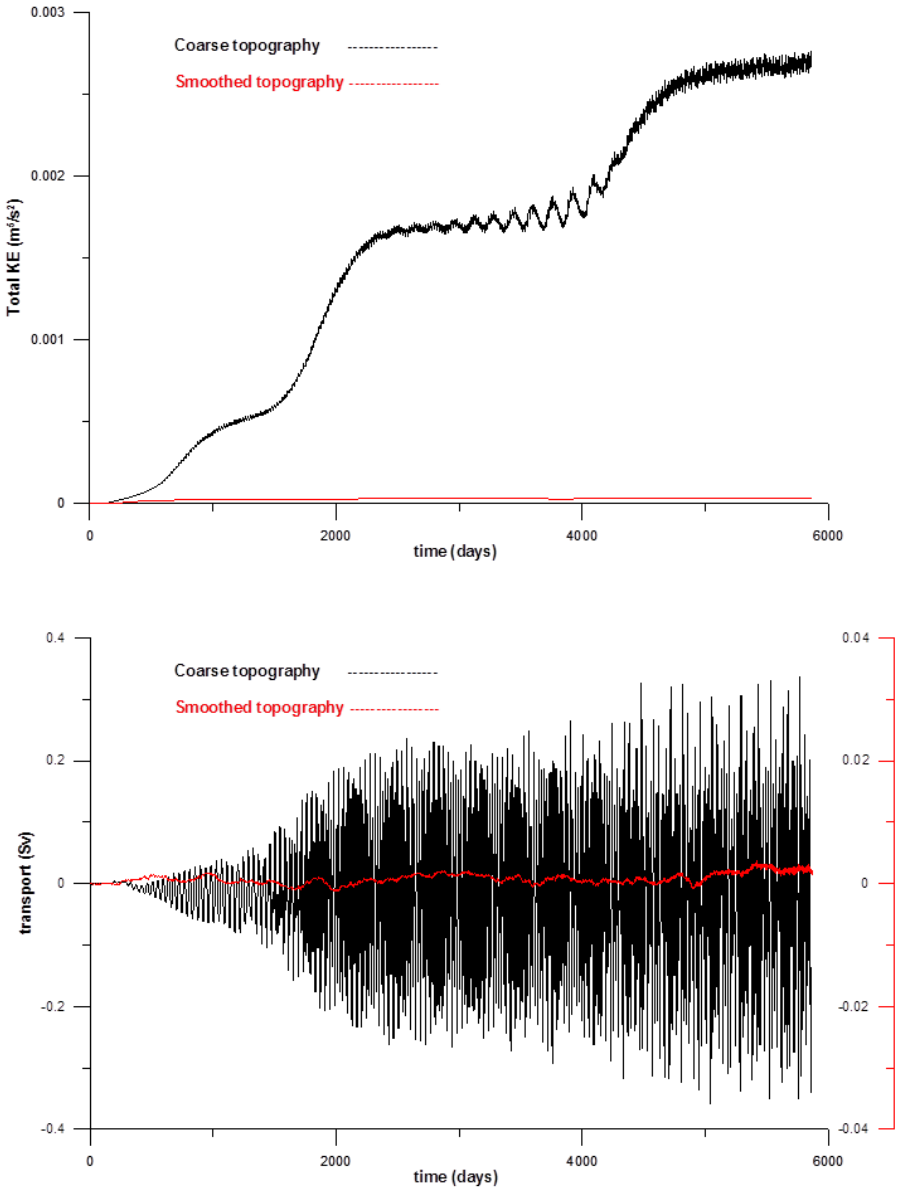

Figure 5.10: *Computational PG error for two model implementations using a smoothed (red line) and an unsmoothed (black line) topography: a) total kinetic energy; b) transport across a meridional section. After* 20 *yr the PG error produces spurious velocities which are* $O(10^{-2})\,\mathrm{m/s}$ *for the coarse topography case and* $O(10^{-4})\,\mathrm{m/s}$ *for the unsmoothed topography case.*

5.4 Sensitivity to topography

Which is the best smoothing scheme for the AB topography? In which way can different criteria for the smoothing affect the model results? On the one hand, the circulation in the AB is strongly influenced by bottom topography, so, in order to preserve fundamental features the topography should be smoothed according to a criterion that is the least possible restrictive. On the other hand, the very steep continental slope around the AB is a strong source of PG errors, which can be limited only by means of a substantial topographic smoothing.

Here we compare results for the AB circulation obtained by using three different topography smoothing criteria. In the first -reference- simulation we have followed condition (5.2) with $c = 0.2$ and condition (5.3); the second experiment (simulation 4) differs from the reference simulation because now $c = 0.15$. In the third experiment (simulation 5) a more selective criterion has been adopted by imposing again $c = 0.15$ but emphasizing the height of the ZR, which would otherwise be too flattened.

Figures 5.11 5.12 5.13 show the results of these sensitivity experiments in terms of the field of SSH variance and of the SSH time series relative to the point P located at 47 °S, 45 °E. The double regime vanishes in simulation 4, the variability being less prominent in this case. We can thus argue that the role of the bottom topography is likely to play a central role in determining the two regimes in the AB and the related rapid switches connecting them. In particular, since we applied $9x9$ cells *Gaussian filters* to the bathymetric data until the conditions 5.2 and 5.3 are satisfied for each point, the final topography yields extremely flattened regions. The ZR, for example, is reduced by a factor 3 with respect to its original value. In other words, in order to be sure to limit the PG errors in the calculation, we have renounced to a realistic reproduction of the currents by effectively damping some of the main topographic features. In simulation 5 we analyze more in detail the role of the ZR in the AB circulation. We use the same smoothing as in simulation 4 but we impose an emphasized seamount in the middle of the AB so that the ZR is not unrealistically reduced. The results show that, again, the system switchs abruptly from one regime to another. These switches are not isolated but occur several times during the integration, while more sta-

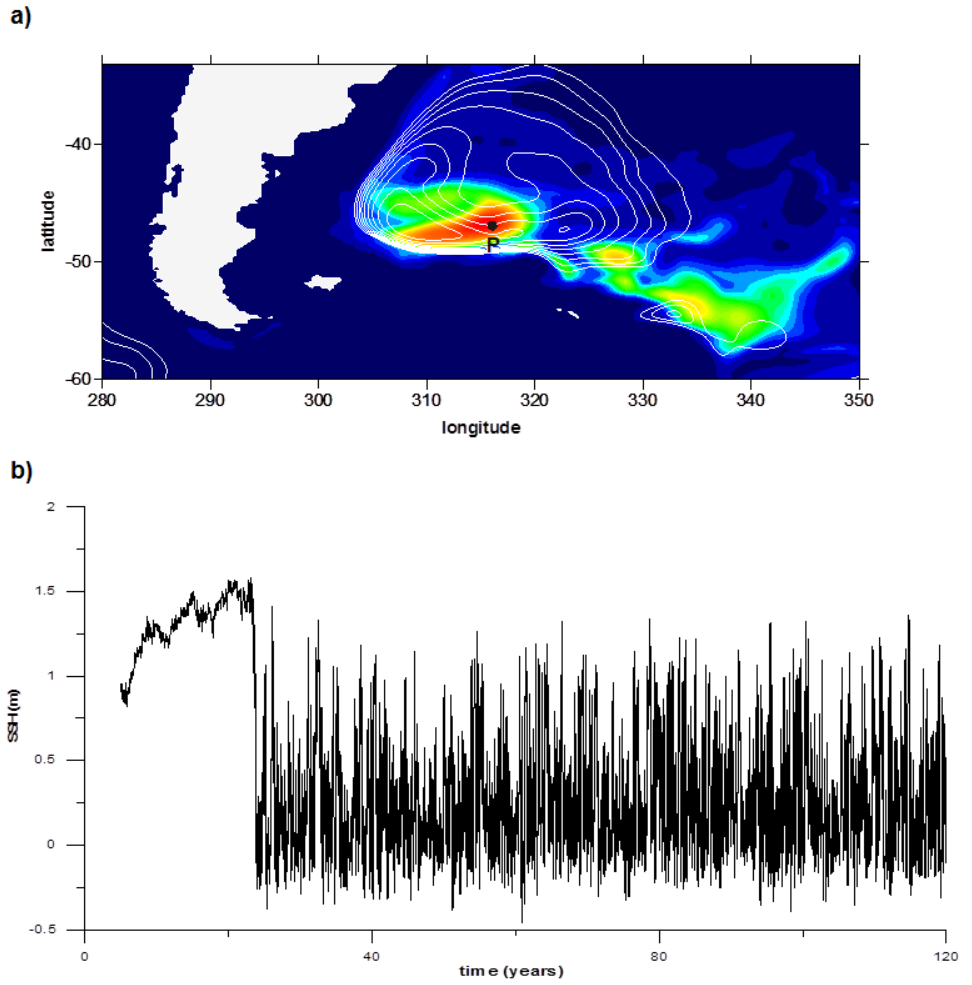

Figure 5.11: *Sensitivity of the AB circulation to topography: results for the reference simulation. a) SSH variance field over the isobaths (white lines); b) SSH time series taken in point P.*

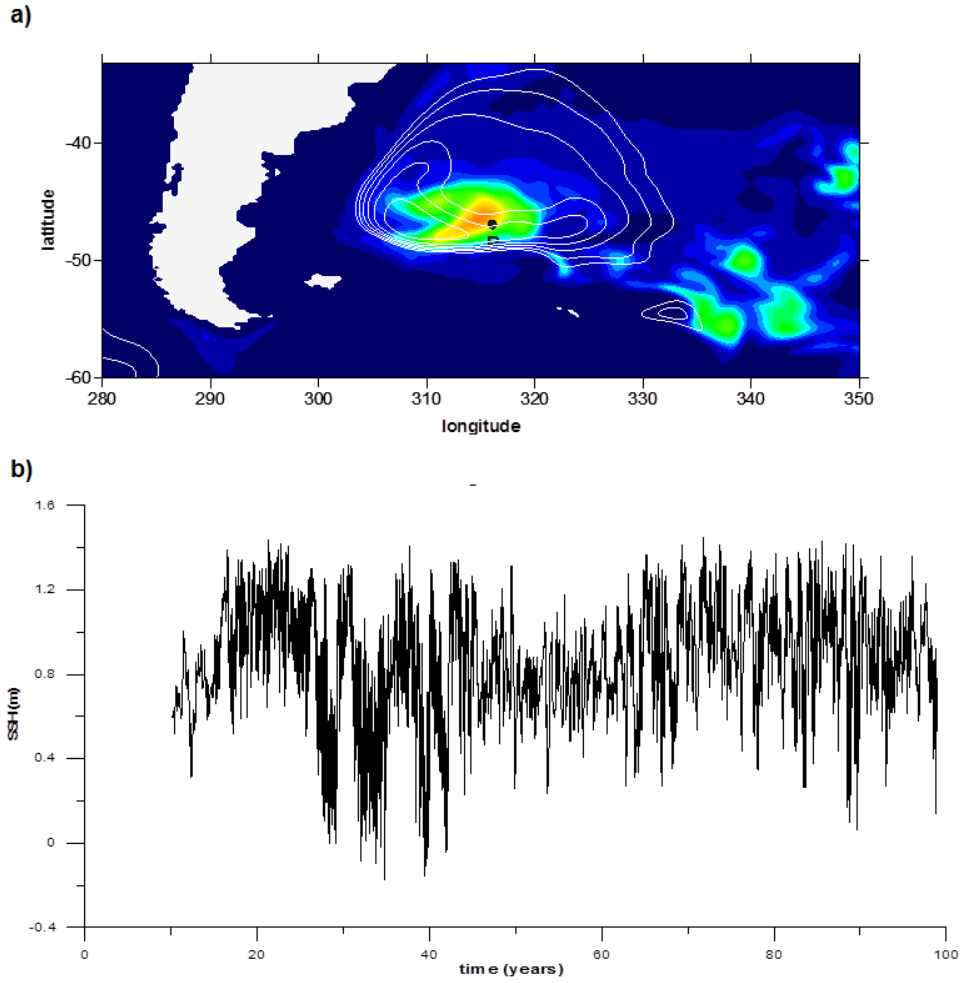

Figure 5.12: *Sensitivity of the AB circulation to topography: results for simulation 4 (more restrictive smoothing). a) SSH variance field over the isobaths (white lines); b) SSH time series taken in point P.*

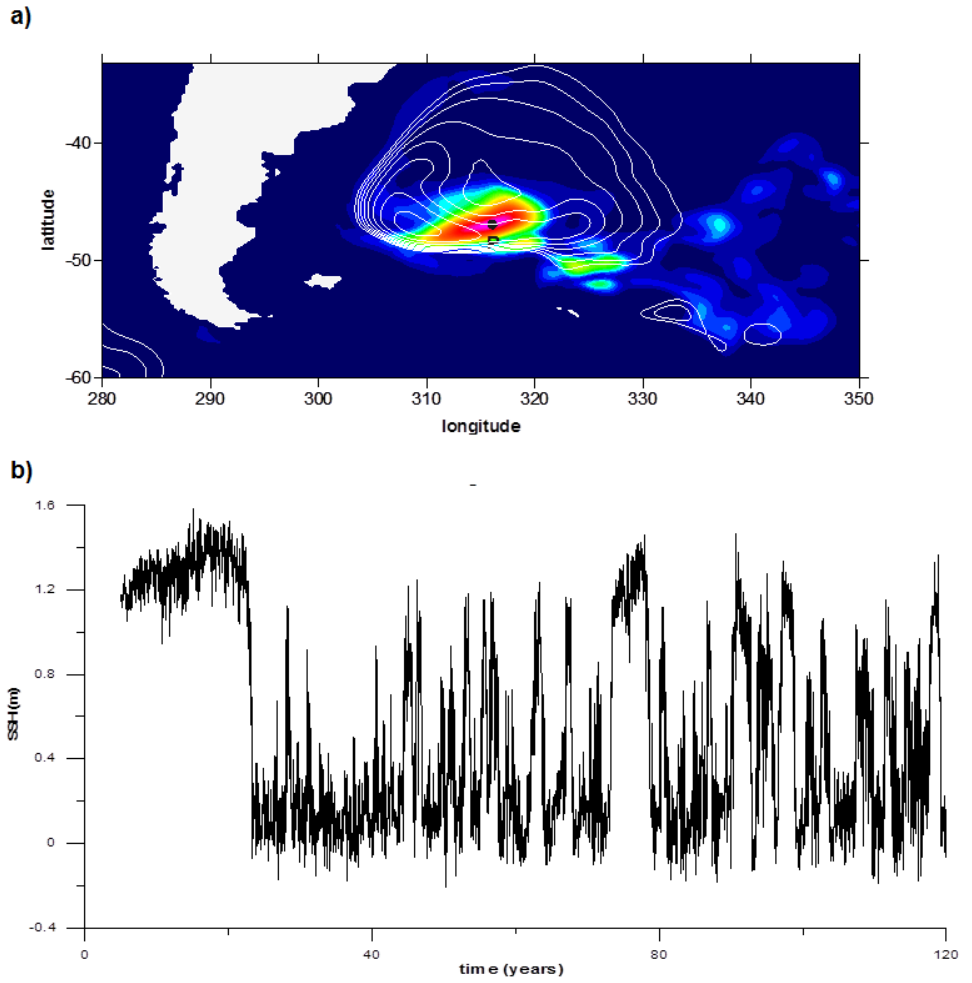

Figure 5.13: *Sensitivity of the AB circulation to topography: results for simulation 5 (trivial selective smoothing). a) SSH variance field over the isobaths (white lines); b) SSH time series taken in point P.*

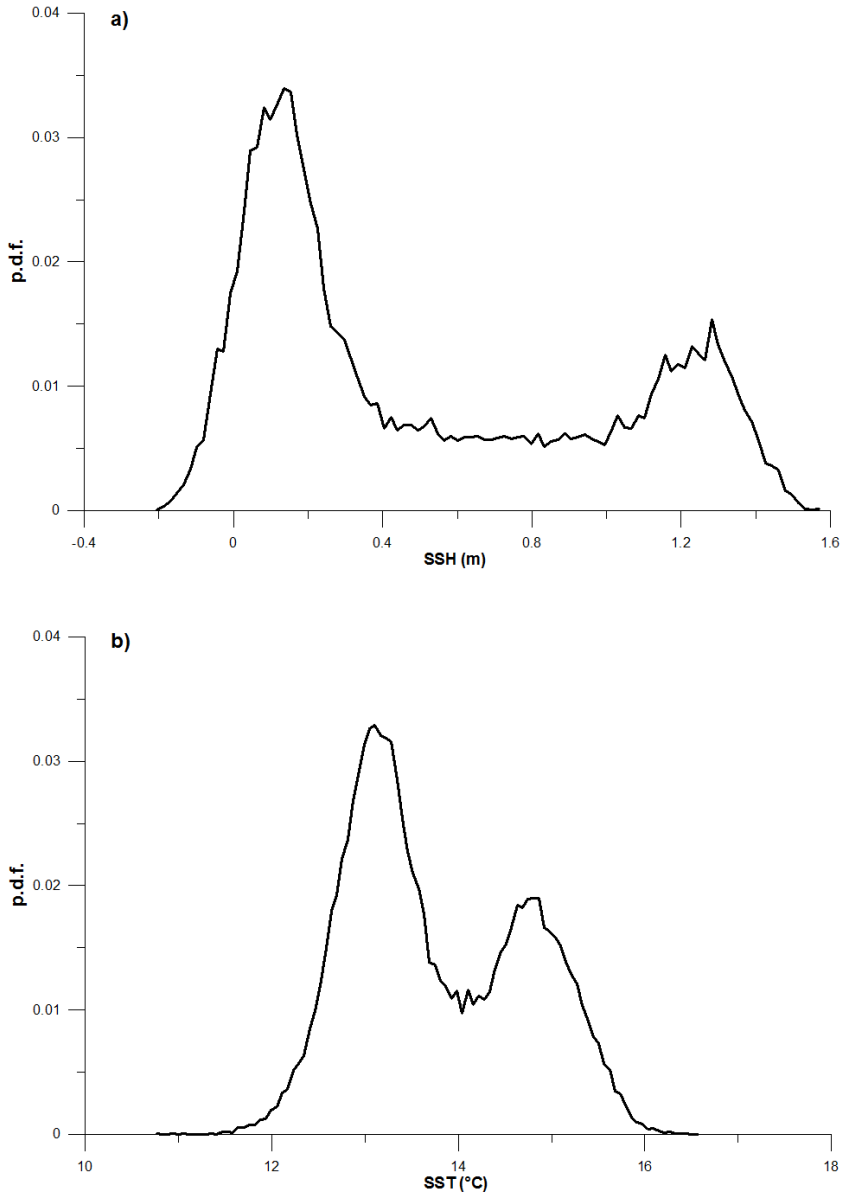

Figure 5.14: *Probability density function of the SSH (a) and of the SST (b) time series for the point P located at 47 °S, 45 °E, for the simulation 5.*

ble periods appear for a limited time. This is qualitative in good agreement with the results of Bigorre and Dewar (2009) (see Figure 5.4). In this model configuration, the bimodal behaviour appears more evident as it can also be deduced from the Figure 5.14 where the PDF of the SSH and SST signals relative to the point P are displayed.

On the basis of these sensitive experiments it is possible to argue that the ZR is a significant feature in determining the intrinsic variability within the AB, probably playing an important role also in establishing the bimodal behaviour of the flow.

5.4.1 The role of the SAF fluctuations in determining the AB regime

In this section we analyze the results of simulation 5, in which several rapid switches occur. Dividing the AB region in 4 sectors as shown in the Figure 5.15, we display the time series of the total KE for each sector and

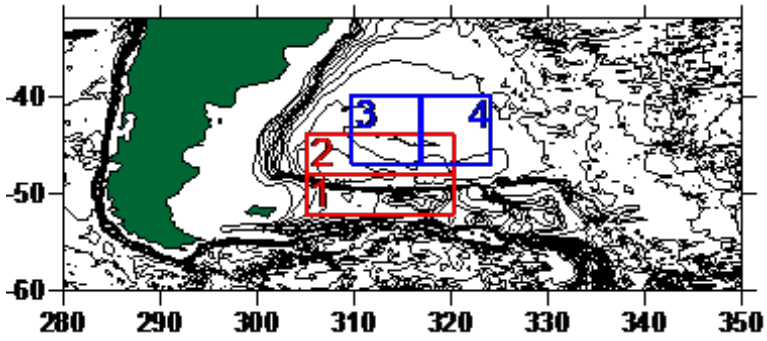

Figure 5.15: *The 4 sectors considered for the phase space analysis.*

the corresponding orbits in four different state planes (Figure 5.16). The system evolution tends to lie in two different sectors in phase space, which are clearly associated with the two different regimes of the AB circulation.

By selecting a limited period in the time integration (in which the system switches from one regime to the other, as shown in Figure 5.16), it is possible to investigate the qualitative leading mechanisms of such a process. The abrupt transition is associated with fluctuactions of the main flow along the southern part of the AB. This can be identified with the SAF, which, due to intrinsic mechanisms, tends to float meridionally, triggering different

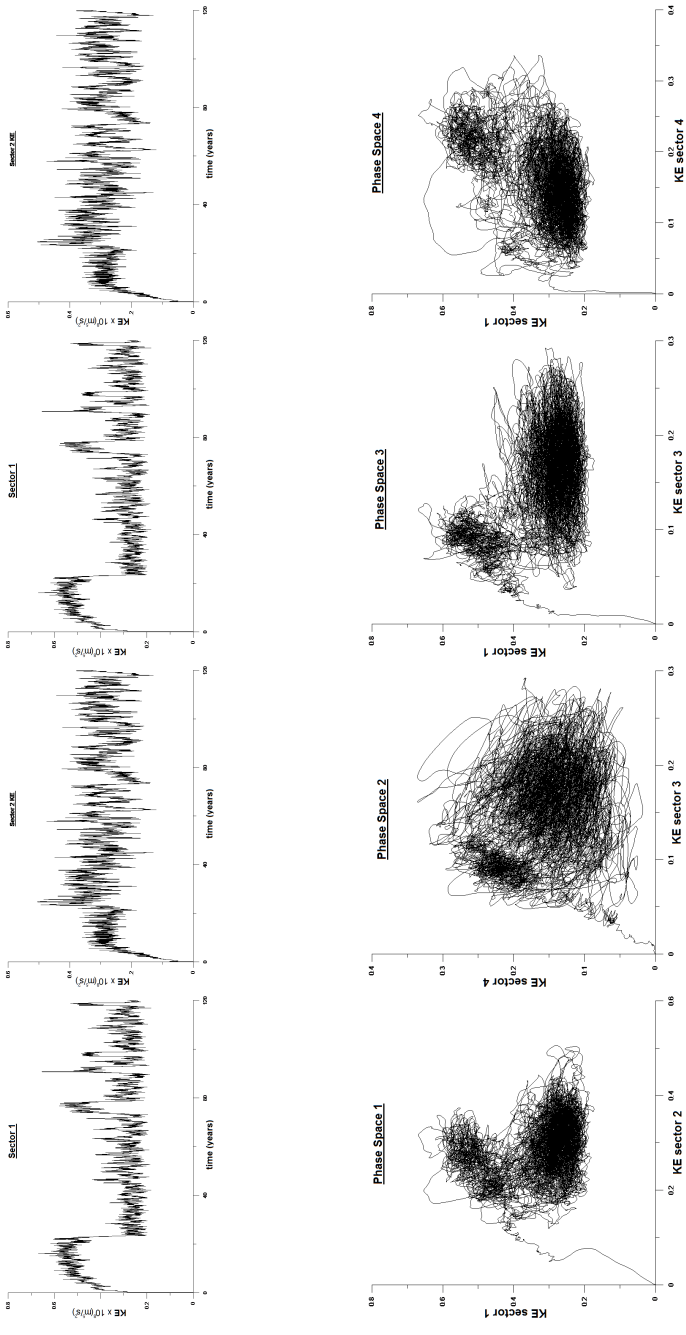

Figure 5.16: *Time series of the KE in each of the considered sectors (upper panels)and associated orbits in four different state planes (lower panels). The switches from one regime to the other is evident.*

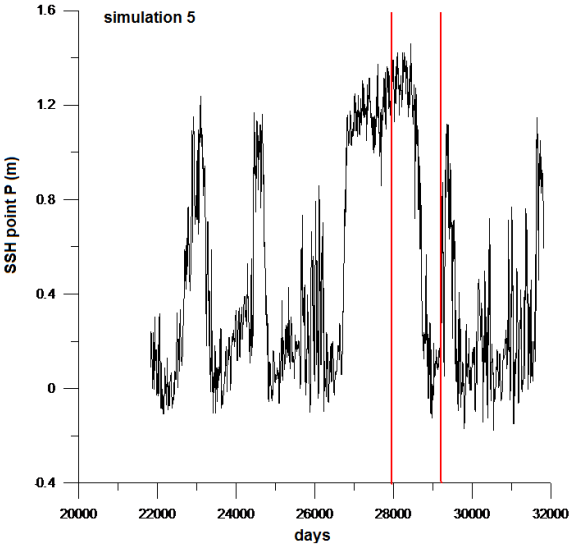

Figure 5.17: *Selected period chosen to analyze the transition between regimes in the AB.*

responses in the AB circulation (Figure 5.18. This is in good agreement with the analysis made by Saraceno *et al.* (2009) who found a good correlation between the acceleration or deceleration of the SAF and the occurence of a strong anticyclonic flow aound the ZR. The position of the SAF oscillates meridionally and, through the interaction with the highly variable bottom topography of the region, the SAF is occasionally able to shift the ZA.

The nature of the variability observed in our channel model shows analogies with the decadal modes associated with Gulf Stream jet and the Kuroshio extension in double-gyre models. Self-sustained oscillations in those models involve the meridional shift of the zonal eastward jet separating from the western boundary as well, as variation in the intensity of this jet. However, for those processes topographic interactions are of second order importance.

All the results and a detailed discussion on the regime switches in the Argentine Basin flow can be soon found on our "in preparation" article (Sgubin *et al.*, 2011).

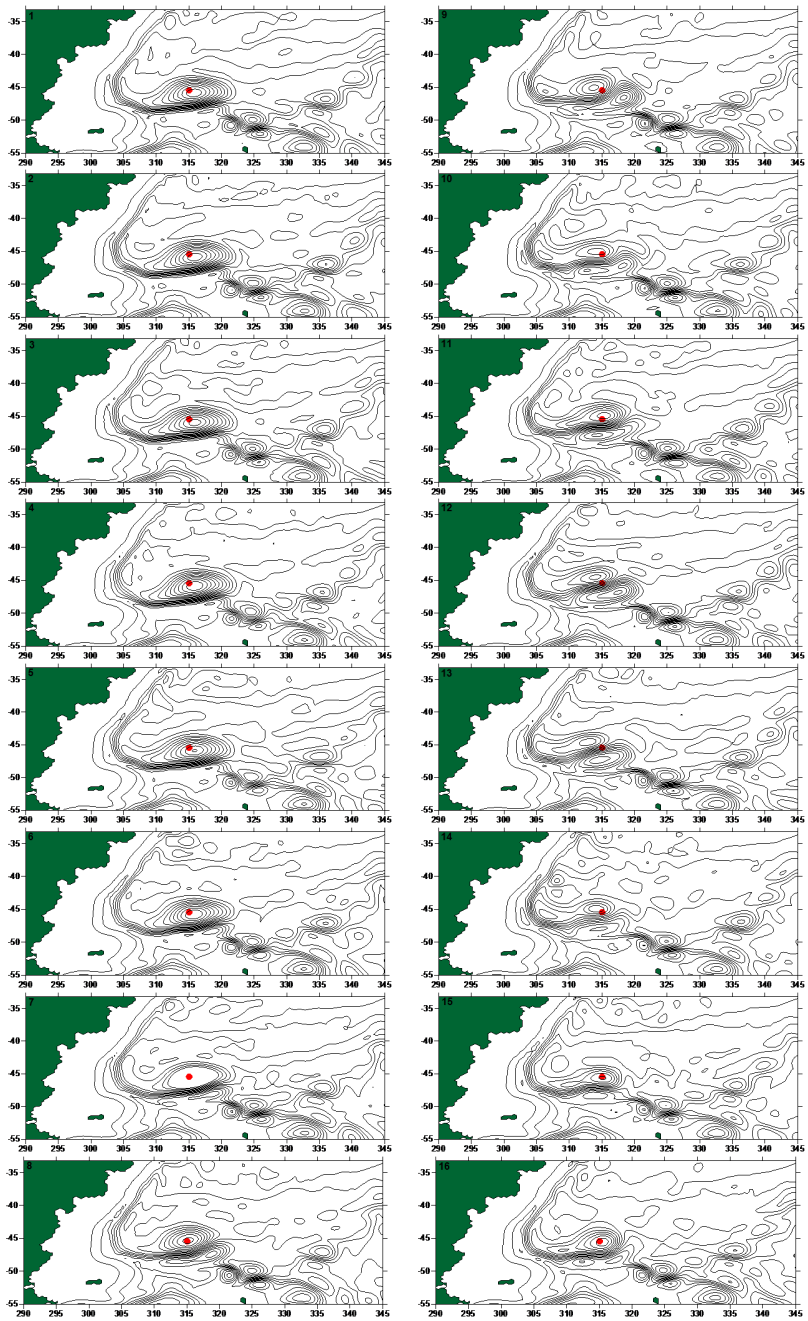

Figure 5.18: *Snapshots (every 90 days) of the averaged streamfunction field during a regime switch in the AB. The red points indicate the position of the top of the Zapiola Rise.*

Summary and conclusions

The object of this thesis is the study of the dynamics of the Southern Ocean and, in particular, of the Antarctic Circumpolar Current (ACC) through a hierarchy of numerical simulations performed with the primitive equation sigma-coordinate Princeton Ocean Model. This PhD project was aimed at obtaining a deeper understanding of the physical processes involved both in the mean flow and in the intrinsic variability of the ACC, which is likely to have a significant influence in the global circulation.

The overall approach adopted in this research is mainly theoretical and is based on the implementation of circulation models in the Southern Ocean within a process-oriented framework. The models have been implemented with steady climatological wind and heat flux forcing. Nevertheless, elements of realism have also been introduced, such as realistic coastline and bathymetry. This, together with the choice of a sigma-coordinate model, have allowed us to reproduce all the main flow-topography interaction processes, and to directly compare our simulations with observational data and other model results.

In the first part of the work (chapter 2), we have focused on the basic dynamical processes involved in the determination of the ACC mean flow. By running a series of numerical simulations, we have stressed the importance of the bottom topography in determining the bottom form drag, an effective stress which closes the momentum balance. Such a dissipative force is also a central mechanism for the meridional heat exchanges between polar regions and sub-tropical regions. However, the presence of the bottom topography in a barotropic model leads to an unrealistic ACC which would, in this case, completely follow the geostrophic contours, losing most of its real

features such as the predominantly zonal flow patterns. The background stratification is indeed another significant factor which needs to be taken into account in modeling the Southern Ocean circulation: through an imposed meridional density gradient it is possible to induce the JEBAR effect, which effectively prevents the total topographic steering. Beyond the purely physical discussion, one of the main goals of this part of the work was to determine a consistent reference model for the Southern Ocean circulation: the representation of the bottom topography and the baroclinicity have, thus, been found to be necessary factors in setting up a realistic model.

The definition of such a valid reference model has allowed us to investigate the dynamical mechanisms occurring within the Southern Ocean. In particular, in the second part of the study, we have focused on the intrinsic variability which may be associated with the ACC. In chapter 3, we have presented results obtained by using an eddy-permitting resolution of our reference model. In such a context, the nonlinear effects have been emphasized and the simulations have displayed a robust mode of both low and high frequency variability. Since the imposed external forcing, i.e. wind stress and heat fluxes, are stationary, the nature of the resulting variability is undoubtedly intrinsic. As such, it is likely to be due to interactions between mean flow and eddies, and it has been found to be sensitive to topography and background stratification. Results have also evidenced limited regions in which such self-sustained changes are clearly more prominent, like, for example, the region around the Zapiola Rise in the Argentine Basin.

The variability associated with the ACC is an important dynamical aspect since it is likely to be relevant to climate variability at global scale. In order to detect the statistical interrelationships between different regions of the Southern Ocean, in chapter 4 a climate network has been constructed on the basis of the simulation data outputs. In this way, teleconnection maps have been constructed. This analysis shows how the Argentine Basin, besides being a location characterized by the most prominent intrinsic variability of our domain, it is also a central region in terms of network system, i.e. it is a region whose dynamics is likely to influence the circulation elsewhere.

Under these circumstances, in the last chapter (5) a deeper analysis of the circulation in the Argentine Basin has been carried out. From our model results, both high and low-frequency variability have been identified in this

region, evidencing different features. The high-frequency variability is characterized by an anticyclone wave around the Zapiola Rise which can be interpreted in terms of topographic Rossby normal modes. Such a propagating anomaly has a period of $O(10)$ days, which is conjectured to be potentially triggered by the lower frequency intrinsic variability. Concerning the low-frequency variability, this is mostly concentrated in the southern part of the basin over the steep continental slope, where the Sub-Antarctic Front is located. The most noticeable result is that such a long term variability yields two distinct regimes with very different variances. The first one is a relatively low variable regime characterized by the permanent presence of the Zapiola Anticyclone over the Zapiola Rise. On the other hand, the second more variable regime is associated with fluctuations of the position of the Sub Antarctic Front, which, in some cases, lead a collapse of the Zapiola Anticyclone. Moreover, the rapidity in which the transition from one regime to another takes place is also striking. These model results are in agreement with recent observations in the Argentine Basin and provide a possible physical interpretation of the effective variability associated with the Zapiola Anticyclone.

Finally, the overall work can represent a valid base for a more detailed investigation of the intrinsic variability in the Southern Ocean and its influence on the global climate. The analysis of teleconnection mechanisms is surely an innovative approach in discussing the ACC dynamics, which deserves to be investigated further. In this sense, this thesis provides a new insight into the relation between internal variability and connectivity, and can be useful for future theoretical studies.

Appendix A

Acronyms list

Abbreviation	Definition
AABW	*Antarctic Bottom Water*
AAIW	*Antarctic Intermediate Water*
AASW	*Antarctic Surface Water*
AB	*Argentine Basin*
ACC	*Antarctic Circumpolar Current*
ACW	*Antarctic Circumpolar Wave*
CDW	*Circumpolar Deep Water*
CFL	*Courant-Friedrichs-Lewy conditions*
CZ	*Confluence Zone*
EKE	*Eddy Kinetic Energy*
ENSO	*El Nino Southern Oscillation*
GEBCO	*General Bathymetric Chart of the Oceans*
HIM	*Hallberg Isopycnal Model*
JEBAR	*Joint Effect of Baroclinicity and Relief*
KE	*Kinetic Energy*
LCDW	*Lower Circumpolar Deep Water*
NADW	*North Atlantic Deep Water*

PDF	*Probability Density Function*
PF	*Polar Front*
PG	*Pressure Gradient*
POM	*Princeton Ocean Model*
POP	*Parallel Ocean Program*
QG	*Quasi-geostrophic*
SAM	*Southern Annular Mode*
SAMW	*Sub-Antarctic Mode Water*
SSH	*Sea Surface Height*
SST	*Sea Surface Temperature*
STF	*Sub-Tropical Front*
UCDW	*Upper Circumpolar Deep Water*
THC	*Thermohaline Circulation*
WOCE	*World Ocean Circulation Experiment*
ZA	*Zapiola Anticyclone*
ZR	*Zapiola Rise*

Bibliography

Anderson, D. I. T. and Gill, A. E. (1975), «Spin-up of a stratified ocean, with application to upwelling», *Deep Sea Reasearch,* **22**, *583-596*.

Baines, P. G. and Cai, W. (2000), «Analysis of an Interactive Instability Mechanism for the Antarctic Circumpolar Wave», *Journal of Climate* **13**, *1831-1844*.

Baker, D. J. (1982), «A note on Sverdrup balance in the Southern Ocean», *Journal of Marine Research,* **40**, *21-26*.

Barnier, B., Marchesiello, P., de Miranda, A. P., Molines, J.-M. and Coulibaly, M. (1998), «A sigma-coordinate primitive equation model for studying the circulation in the South Atlantic. Part I: Model configuration with error estimates», *Deep-Sea Research,* **45**, *543-572*.

Bergamasco, A., Defendi, V., Zambianchi, E. and Spezie, G. (2002), «Evidence of dense water overflow on the Ross Sea shelf-break», *Antarctic Science* **14**, *271-277*.

Best, S. E., Ivchenko, V. O., Richards, K. J., Smith, R. D. and Malone, R. C. (1999), «Eddies in numerical models of the Antarctic Circumpolar Current and their influence on the mean flow», *Journal of Physical Oceanography,* **29**, *328-350*.

Bigorre, S. and Dewar, W. K. (2009), «Oceanic time variability near a large scale topographic circulation», *Ocean Modelling*, **29**, *176-188*.

Broecker, W. (1991), «The great ocean conveyor», *Oceanography* **4**, *79-89*.

Bryan, F. (1986), «High-latitude salinity effects and interhemispheric thermohaline circulation», *Nature* **323**, *301-304*.

Cai, W. and Baines, P. G. (1996), «Interactions between thermohaline- and wind-driven circulations and their relevance to the dynamics of the Antarctic Circumpolar Current in a coarse-resolution global ocean general circulation model», *Journal of Geophysical Research,* **101**, *14073-14093*.

Cane, M. A., Kamenkovich, V. M. and Krupitsky, A. (1995), «On the utility and disutility of JEBAR», *Journal of Physical Oceanography, Notes and Correspondece* **22**, *301-305*.

Danabasoglu, G. and Mc Williams, J. C. (1995), «Sensitivity of the global ocean circulation to parametrization of mesoscale tracer transport», *Journal of Climate,* **8**, *2967-2987*.

de Miranda, A. P., Barnier, B. and Dewar, W. K. (1999), «On the dynamics of the Zapiola Anticyclone», *Journal of Geophysical Research,* **104**, *21139-21149*.

Dewar, W. K. (1998), «Topography and barotropic transport control by bottom friction», *Journal of Marine Research,* **56**, *295-328*.

Diestel, R. (2005), *Graph Theory*, Springer-Verlag, Berlin, Germany.

Dijkstra, E. W. (1959), «A Note on Two Problems in Connexion with Graphs», *Numerische Mathematik,* **1**, *269-271*.

Dijkstra, H. A. (2005), *Nonlinear Physical Oceanography*, Springer, Dordrecht, The Netherlands.

Dijkstra, H. A. (2007), «Characterization of the multiple equilibria regime in a global ocean model», *Tellus A* **59**, *695-705*.

Dijkstra, H. A. (2008), *Dynamical Oceanography*, Springer, Dordrecht, The Netherlands.

Dijkstra, H. A. and Ghil, M. (2005), «Low-frequency variability of the large-scale ocean circulation: A dinamical system approach», *Reviews of Geophysics,* **43**, *RG3002, doi:10.1029/2002RG000122*.

Dijkstra, H. A. and te Raa, L. (2004), «Systematic approach to determine thresholds of the ocean's thermohaline circulation», *Tellus A* **56**, *362-370*.

Donges, J. F., Zou, Y., Marwan, N. and Kurths, J. (2009), «Complex networks in climate dynamics», *The European Physical Journal Special Topics,* **174**, *157-179*.

Fu, L. L. (2007), «Intercaction of mesoscale variability with large-scale waves in the Argentine Basin», *Journal of Physical Oceanography,* **37**, *787-793*.

Fu, L. L., Cheng, B. and Qiu, B. (2001), «25-days period large-scale oscillations in the Argentine Basin revealed by the TOPEX/Poseidon altimeter», *Journal of Physical Oceanography,* **31**, *506-517*.

Gent, P. R., Large, W. G. and Bryan, F. O. (2001), «What sets the mean transport accross the Drake Passage?», *Journal of Geophysical Research,* **106**, *2693-2712*.

Gille, S. T. (1997), «The Southern Ocean momentum balance: evidence for topographic effects from numerical model output and altimeter data», *Journal of Physical Oceanography* **27**, *2219-2232*.

Gille, S. T. (2003), «Float observations of the Southern Ocean: Part 1, Estimating mean fields, bottom velocities, and topographic steering», *Journal of Physical Oceanography,* **33**, *1167-1181*.

Gnanadesikan, A. and Hallberg, R. W. (2000), «On the relationship of the Circumpolar Current to Southern Hemisphere winds in coarse resolution ocean model», *Journal of Physical Oceanography,* **30**, *2013-2034*.

Gordon, A. L. and Owens, W. B. (1987), «Polar oceans», *Reviews of Geophysics* **25(2)**, *227-233*.

Hallberg, R. and Gnanadesikan, A. (2006), «The Role of Eddies in Determining the Structure and Response of the Wind-Driven Southern Hemisphere Overturning: Results from the Modeling Eddies in the Southern Ocean (MESO) Project», *Journal of Physical Oceanography,* **36**, *2232-2252*.

Hidaka, K. and Tsuchiya, M. (1953), «On the Antarctic Circumpolar Current», *Journal of Marine Research,* **12**, *214-222*.

Hogg, A. M. and Blundell, J. R. (2006), «Interdecadal variability of the Southern Ocean», *Journal of Physical Oceanography,* **36**, *1626-1645*.

Hogg, A. M., Killworth, P. D., Blundell, J. R. and Dewar, W. K. (2005), «Mechanisms of decadal variability of the wind-driven ocean circulation», *Journal of Physical Oceanography,* **35**, *512-531*.

Hughes, C. V. (2002), «Sverdrup-like theories of the Antarctic Circumpolar Current», *Journal of Marine Research,* **60**, *1-17*.

Hughes, C. W. and E. Ash, E. R. (2001), «Eddy forcing of the mean flow in the Southern Ocean», *Journal of Geophysical Research* **106**, *2713-2722*.

Hughes, C. W. and Killworth, P. (1995), «Effects of bottom topography in the large-scale circulation of the Southern Ocean», *Journal of Physical Oceanography,* **25**, *2485-2497*.

Hughes, C. W., Stepanov, V. N., Barnier, B. and Hargreaves, G. W. (2007), «Three forms of variability in Argentine Basin ocean bottom pressure», *Journal of Geophysical Research,* **112**, *C01011*.

Hughes, T. M. C. and Weaver, A. J. (1994), «Multilple equilibria of an asymmetric two-basin ocean model», *Journal of Physical Oceanography* **24**, *619-637*.

Ishida, A. (1994), «Effects of partial meridional barriers on the Antarctic Circumpolar Current wind-driven barotropic model», *Dynamics of Atmosphere and Oceans,* **20**, *315-341*.

Ivchenko, V. O., Richards, K. J. and Stevens, D. P. (1991), «The dynamics of the Antarctic Circumpolar Current.», *Journal of Physical Oceanography,* **21**, *236-264*.

Ivchenko, V. O., Krupitsky, A. E., Kamenkovich, V. M. and Wells, N. (1999), «Modeling the Antarctic Circumpolar Current: A comparison of FRAM and equivalent barotropic model results», *Journal of Marine Research,* **57**, *29-45*.

Jiang, S., Jin, F. and Ghil, M. (1995), «Multiple equilibria, periodic and aperiodic solutions in a wind-driven, double-gyre, shallow-water model», *Journal of Physical Oceanography,* **25**, *764-786*.

Keffer, T. and Holloway, G. (1988), «Estimating Southern Ocean eddy flux of heat and salt from satellite altimetry», *Nature* **332**, *91-147*.

Kelley, J. (1975), *General Topology*, Springer-Verlag, New York, U.S.A.

Krupitsky, A. E. and Cane, M. A. (1994), «On topographic pressure drag in a zonal channel», *Journal of Marine Research,* **52**, *1-23*.

Krupitsky, A. E., Kamenkovich, V., Naik, N. and Cane, M. A. (1996), «A linear equivalent barotropic model of the Antarctic Circumpolar Current with realistic coastlines and bottom topography», *Journal of Physical Oceanography,* **26**, *1803-1824*.

Langlais, C., Rintoul, S. and Schiller, A. (2011), «Variability and mesoscale activity of the Southern Ocean fronts: identification of a circumpolar coordinate system», *Ocean Modeling* **39**, *79-96*.

Lorenz, E. N. (1963), «Deterministic Nonperiodic Flow», *Journal of the Atmospheric Sciences,* **20**, *130-141*.

Marchesiello, P., Barnier, B. and de Miranda, A. P. (1998), «A sigma-coordinate primitive equation model for studying the circulation in the South Atlantic. Part II: Meridional transport and seasonal variability», *Deep-Sea Research,* **45**, *573-608*.

Marshall, D. (1995a), «Influence of topography on the large-scale ocean circulation», *Journal of Physical Oceanography,* **25**, *1622-1635*.

Marshall, D. (1995b), «Topographic steering of the Antarctic Circumpolar Current», *Journal of Physical Oceanography,* **25**, *1636-1650*.

Matthews, A. J. and Meredith, M. P. (2004), «Variability of Antarctic circumpolar transport and the Southern Annular Mode associated with the Madden-Julian Oscillation», *Geophysical Research Letters* **31**, *L24312, doi:10.1029/2004GL021666*.

McCalpin, J. D. and Haidvogel, D. B. (1996), «Phenomenology of the low-frequency variability in a reduced-gravity, quasigeostrophic double-gyre model», *Journal of Physical Oceanography,* **26**, *739-752*.

McCartney, M. S. (1977), «Subantarctic Mode Water», in «A Voyage of Discovery: George Deacon 70th Anniversary Volume», Deep-Sea Research, p. 103–119, Pergamon Press, Oxford.

Mellor, G. L. (2004), *A three dimensional, primitive equation, numerical ocean model*.

Mellor, G. L. and Yamada, T. (1982), «Development of a turbulence closure model for geophysical fluid problems», *Reviews of Geophysics and Space Physics,* **20**, *851-875*.

Mertz, G. and G., D. W. D. (1992), «Interpretations of the JEBAR Term», *Journal of Physical Oceanography,* **25**, *519-526*.

Messinger, F. (1982), «On the convergence and error problems of the calculation of the pressure gradient force in sigma coordinate model», *Geophysical and Astrophysical Fluid Dynamics,* **19**, *105-117*.

Munk, W. H. and Palmen, E. (1951), «Note on dynamics of Antarctic Circumpolar current», *Tellus* **3**, *53-56*.

Naveira Garbato, A. C., Jullion, L., Stevens, D. P., Heywood, J., K. and King, B. A. (2009), «Variability of Subantarctic Mode Water and Antarctic Intermediate Water in the Drake Passage during the Late-Twentieth and Early-Twenty-First Centuries», *Journal of Climate,* **22**, *3661-3688*.

Nicolis, G. (1995), *Introduction to nonlinear science*, Cambridge University Press, Cambridge, UK.

Olbers, D., Borowski, D., Volker, C. and Wolff, J. O. (2004), «The dynamical balance, transport and circulation of Antarctic Circumpolar Current», *Antarctic Science* **16**, *439-470*.

Orsi, A. H., Whitworth III, T. W. and Nowlin Jr., W. D. (1995), «On the meridional extent and fronts of Antarctic Circumpolar Current», *Deep-Sea Research* **42**, *641-673*.

Pedlosky, J. (1987), *Geophysical Fluid Dynamics*, Springer-Verlag, New York, U.S.A.

Peterson, R. G., Nowlin, W. D. and T.W., T. W. I. (1982), «Generation and Evolution of a cyclonic ring at Drake Passage in Early 1979», *Journal of Physical Oceanography* **12**, *712-719*.

Peterson, R. G. and White, W. B. (1998), «Slow oceanic teleconnections linking the Antarctic Circumpolar Wave with the tropical ENSO», *Journal of Geophysical Research*, **103**, *24573-24583*.

Pierini, S. (1996), «Topographic Rossby modes in the Strait of Sicily», *Journal of Geophysical Research*, **101**, *6429-6440*.

Pierini, S. (2005), «A model of the Antarctic Circumpolar Current system», Report, 3rd International Conference on the Oceanography of the Ross Sea Antarctica, October 2005, Venice.

Pierini, S. (2006), «A Kuroshio Extension System model study: decadal chaotic self-sustained oscillations», *Journal of Physical Oceanography*, **36**, *1605-1625*.

Pierini, S. (2011), «Low-frequency variability, coherence resonance and phase selection in a low-order model of the wind-driven ocean circulation», *Journal of Physical Oceanography*, **41**, *1585-1604*.

Pierini, S. and Dijkstra, H. A. (2009), «Low-frequency variability of the Kuroshio Extension», *Nonlinear Processes in Geophysics*, **16**, *665-675*.

Pierini, S., Dijkstra, H. A. and Riccio, A. (2009), «A nonlinear theory of the Kuroshio Extension bimodality», *Journal of Physical Oceanography*, **39**, *2212-2229*.

Pillsbury, R. D. and Bottero, J. S. (1984), «Observations of current rings in the Antarctic Zone at Drake Passage», *Journal of Marine Research* **42**, *853-874*.

Rahmstorf, S. (2000), «The thermohaline ocean circulation: a system with dangerous threshold?», *Climatic Change* **46**, *247-256*.

Rahmstorf, S. (2002), «Ocean circulation and climate during the past 120,000 years», *Nature* **419**, *207-214*.

Rintoul, S. R., Hughes, C. and Olbers, D. J. (2001), «The Antarctic Circumpolar Current system», in «Ocean Circulation and Chmate», Academic Press, p. 271–302, G. Siedler, J. Church and J. Gould Eds.

Sallee, J. B., Morrow, R. and Speer, K. (2008), «Response of the Antarctic Circumpolar Current to atmospheric variability», *Journal of Climate* **21**, *3020-3039*.

Saraceno, M., Provost, C. and Zajaczkovski, U. (2009), «Long-term variation in the anticyclonic ocean circulation over the Zapiola Rise as observed by satellite altimetry: Evidence of possible collapses», *Ocean Modelling*,**29**, *176-188*.

Saunders, P. and King, B. (1995), «Bottom currents derived from a shipborne ADCP on WOCE cruise in the South Atlantic», *Journal of Physical Oceanography*, **25**, *329-347*.

Sgubin, G. (2008), *Analisi della Corrente Circumpolare Antartica mediante studi modellistici*, Master thesys in Oceanography, advisor Pierini, S., University "Parthenope", Naples.

Sgubin, G., Pierini, S. and Dijkstra, H. A. (2011), «Possible regime switches in the Argentine Basin flow,», *In Preparation*.

Simonnet, E. and Dijkstra, H. A. (2002), «Spontaneous generation of low-frequency modes of variability in the wind-driven ocean circulation», *Journal of Physical Oceanography*, **32**, *1747-1762*.

Simonnet, E., Ghil, M. and Dijkstra, H. A. (2005), «Quasi-homoclinic behavior of the barotropic quasi-geostrophic double-gyre circulation», *Journal of Marine Research*, **63**, *931-956*.

Sorensen, J. V. T., Ribbe, J. and Shafer, G. (2001), «Antarctic Intermediate Water mass formation in ocean general circulation models.», *Journal of Physical Oceanography* **31**, *3295-3311*.

Spall, M. A. (1996), «Dynamics of the Gulf Stream/Deep Western Boundary current crossover. Part II: Low-frequency internal oscillations», *Journal of Physical Oceanography*, **26**, *2169-2182*.

Stanton, B. R. and Morris, M. Y. (2004), «Direct velocity measurements in the Subantarctic Front and over Campbell Plateau, southeast of New Zealand», *Journal of Geophysical Research* **109**, *1-11*.

Stocker, T. F. and A., S. (1997), «Influence of CO_2 emission rates on the stability of the thermohaline circulation», *Nature* **388**, *862-865*.

Stommel, H. (1957), «A survey of ocean current theory», *Deep-Sea Research* **4**, *149-184*.

Stommel, H. (1961), «Thermohaline convection with two stable regimes of flow», *Tellus* **13**, *224-230*.

Strogatz, S. H. (1994), *Nonlinear dynamics and chaos*, Westview Press, Cambridge, Massachusetts, U.S.A.

Swart, N. C., Ansorge, I. J. and Lutjeharms, J. R. E. (2008), «Detailed characterization of a cold Antarctic eddy», *Journal of Geophysical Research* **113**, *1-15*.

Tai, C.-K. and Fu, L. (2005), «25-day period large-scale oscillations in the Argentine Basin revisited», *Journal of Physical Oceanography*, **35**, *1473-1479*.

Tomczak, M. and Godfrey, J. S. (2003), «Regional Oceanography: an Introduction», Online book http://www.lei.furg.br/ocfis/mattom/regoc/pdfversion.html.

Tomczak, M. and Liefrink, S. (2005), «Interannual variations of water mass volumes in the Southern Ocean», *Journal of Atmospheric and Ocean Science* **10**, *31-42*.

Trani, M., Falco, P. and Zambianchi, E. (2011), «Near-surface eddy dynamics in the Southern Ocean», *Polar Research*, submitted.

Treguier, A. M. and Mc Williams, J. C. (1990), «Topographic influences on wind-driven stratified flow in a β-plane channel: an idealized model for

the Antarctic Circumpolar Current.», *Journal of Physical Oceanography,* **20**, *321-344*.

Volkov, D. L. and Fu, L. L. (2008), «The role of vorticity fluxes in the dynamics of the Zapiola Anticyclone», *Journal of Geophysical Research,* **113**, *C11015*.

Warren, B. A., LaCasce, J. H. and Robbins, P. E. (1996), «On the obscurantist physics of "form drag" in theorizing about the Circumpolar current», *Journal of Physical Oceanography* **26**, *2297-2301*.

Watts, D. J. and Strogatz, S. H. . (1998), «Collective dynamics of "small-world" networks», *Nature,* **393**, *440-442*.

Webb, D. J. (1993), «A simple model of the effect of the kerguelen Plateau on the strength of the Antarctic Circumpolar Current», *Geophysics Astrophysics Fluid Dynamics,* **70**, *57-84*.

Weijer, W., de Ruijter, W. P. M., Dijkstra, H. A. and van Leeuwen, P. J. (1999), «Impact of interbasin exchange on the Atlantic Overturning Circulation», *Journal of Physical Oceanography* **29**, *2266-2284*.

Weijer, W., Vivier, F., Gille, S. T. and Dijkstra, H. A. (2007a), «Multiple oscillatory modes of the Argentine Basin. Part I: statistical analysis», *Journal of Physical Oceanography,* **37**, *2855-2868*.

Weijer, W., Vivier, F., Gille, S. T. and Dijkstra, H. A. (2007b), «Multiple oscillatory modes of the Argentine Basin. Part II: the spectral origin of basin modes», *Journal of Physical Oceanography,* **37**, *2869-2881*.

Weisse, R., Mikolajewicz, U., Sterl, A. and Drijfhout, S. S. (1999), «Stochastically forced variability in the Antarctic Circumpolar Wave», *Journal of Geophysical Research,* **104**, *11049-11064*.

White, W. B. and Peterson, R. G. (1996), «An Antarctic circumpolar wave in surface pressure, temperature and sea-ice extent», *Nature* **380**, *699-702*.

Whitworth III, T. W. (1983), «Monitoring the trasport of the Antarctic Circumpolar current from bottom pressure measurements», *Journal of Physical Oceanography* **13**, *2045-2057*.

Whitworth III, T. W. and Paterson, R. G. (1985), «Volume transport of the Antarctic Circumpolar current from bottom pressure measurements», *Journal of Physical Oceanography* **15**, *810-816*.

Whitworth III, T. W., Orsi, A. H., Kim, S. J., Nowlin Jr, W. D. and Locarnini, R. A. (1998), «Water masses and mixing near the Antarctic slope front», *Ocean, Ice, and Atmosphere: Interactions at the Antarctic Continental Margin Antarctic Research Series* **75**, *1-27*.

Wolff, J. O., Maier-Reimer, E. and Olbers, D. J. (1996), «Wind-driven flow over topography in a zonal β-plan channel: a quasi-geostrophic model of the Antarctic Circumpolar Current.», *Journal of Physical Oceanography*, **26**, *753-774*.